

08

III

NASA CR

144676

All-Digital Precision Processing of ERTS Images

E7.6-10040

CR-144676

"Made available under NASA sponsorship  
in the interest of early and wide dis-  
semination of Earth Resources Survey  
Program information and without liability  
for any use made thereof."

1161A

RECEIVED

APR 10 1975

SIS/902.6

**ALL-DIGITAL PRECISION PROCESSING OF ERTS IMAGES**

**Ralph Bernstein  
International Business Machines Corporation  
18100 Frederick Pike  
Gaithersburg, Maryland 20760**

**April 1975  
Final Report**

**Prepared under NASA contract NAS5-21716 for  
GODDARD SPACE FLIGHT CENTER  
Greenbelt, Maryland 20771**

**Original photography may be purchased from  
EROS Data Center  
10th and Dakota Avenue  
Sioux Falls, SD 57198**

TECHNICAL REPORT STANDARD TITLE PAGE

1. Report No.	2. Government Accession No.	3. Recipient's Catalog No.	
4. Title and Subtitle ALL-DIGITAL PRECISION PROCESSING OF ERTS IMAGES		5. Report Date April 1975	
		6. Performing Organization Code	
7. Author(s) Ralph Bernstein		8. Performing Organization Report No. FSD-75-0009	
9. Performing Organization Name and Address International Business Machines Corporation 18100 Frederick Pike Gaithersburg, Maryland 20760		10. Work Unit No.	
		11. Contract or Grant No. NAS5-21716	
12. Sponsoring Agency Name and Address NASA Goddard Space Flight Center Greenbelt, Maryland 20771 Technical Monitor: Frederick Gordon, Jr.		13. Type of Report and Period Covered Final Report	
		14. Sponsoring Agency Code	
15. Supplementary Notes			
16. Abstract  Digital techniques have been developed and used to apply precision-grade radiometric and geometric corrections to ERTS MSS and RBV scenes. Geometric accuracies sufficient for mapping at 1:250 000 scale have been demonstrated. Radiometric quality has been superior to ERTS NDPF precision products. A configuration analysis has shown that feasible, cost-effective all-digital systems for correcting ERTS data are easily obtainable. This report contains a summary of all results obtained during this study and includes: radiometric and geometric correction techniques, reseau detection, GCP location, re-sampling, alternative configuration evaluations, and error analysis.			
17. Key Words (Selected by Author(s)) Digital image processing, ERTS image processing, precision image correction, resampling, LANDSAT investigation		18. Distribution Statement	
19. Security Classif. (of this report)	20. Security Classif. (of this page)	21. No. of Pages 148	22. Price*

## PREFACE

This is the final report on IBM's study of All-Digital Precision Processing of ERTS Images performed under NASA contract NAS5-21716. It summarizes the effort and results of the entire study, and is submitted in accordance with Item 5 of Article II of the study contract.

The principal objectives of this study were:

1. To develop and evaluate all-digital techniques for the precision-grade radiometric and geometric correction of ERTS RBV and MSS data
2. To evaluate several alternative hardware configurations for applying digital corrections in a production environment.

These objectives have been accomplished. The required digital techniques have been developed and have been used to correct one RBV scene and several MSS scenes. Absolute geometric accuracies obtained in the digital products are sufficient for mapping at a 1:250,000 scale. Radiometric quality obtained is excellent and is superior to that of the NDPF precision (scene corrected) products. The results show that digital methods provide a viable technology for the correction of ERTS data.

A very effective algorithm for locating reseau marks in RBV images has been developed. Study of the performance of the Sequential Similarity Detection Algorithm (SSDA) has shown that it can serve as the basis for an automatic ground control point (GCP) location scheme. Three different methods of resampling the input data space to derive correct output data values have been implemented. Further study is required to determine whether the expense of the more costly resampling techniques is justified by an increase in output quality and utility.

Several different production systems have been defined and evaluated. The results show that digital implementations are economically feasible and that system cost effectiveness can be improved by the judicious use of special-purpose digital hardware. (As used in this report, the term "special-purpose digital hardware" refers to microprogrammed processors and other high-speed digital equipment.)

The following principal recommendations result from this study:

1. Digital technology should be used for future systems for correcting high-resolution earth observation sensor data.
2. The use of special-purpose digital hardware should be considered strongly for high-throughput production image processing systems.

3. The possible benefits of the more expensive resampling techniques should be studied carefully to see whether they justify the increased processing costs.

The principal investigator for this study was R. Bernstein. He was supported by M. Cain, C. Colby, R. Depew, D. Ferneyhough, S. Forrer, H. Markarian, S. Murphrey, W. Niblack, and J. Przybocki.

Appreciation and thanks are extended to Mr. Paul Heffner, the Scientific Monitor of this contract, and to J. Eck of NASA and T. Berger, M. Byerly, and R. McEwen of the U.S. Geological Survey for their assistance during the course of this study.

## CONTENTS

		Page
Section 1	INTRODUCTION AND SUMMARY	1-1
1.1	Purpose	1-1
1.2	Scope of the Study	1-1
1.3	Summary of Effort	1-2
1.4	Conclusions	1-2
1.5	Recommendations	1-4
1.6	New Technology	1-6
Section 2	RADIOMETRIC CORRECTION	2-1
2.1	RBV Radiometric Correction	2-1
2.2	MSS Radiometric Correction	2-4
Section 3	GEOMETRIC CORRECTION	3-1
3.1	Geometric Correction Techniques	3-1
3.2	Results	3-7
Section 4	RESEAU DETECTION AND LOCATION	4-1
Section 5	LOCATION OF GROUND CONTROL POINTS	5-1
Section 6	COMPARISON OF RESAMPLING TECHNIQUES	6-1
6.1	Nearest Neighbor Assignment	6-1
6.2	Bilinear Interpolation	6-4
6.3	Cubic Convolution	6-6
6.4	Resampling Experiment	6-8
6.5	Related IRAD Investigations	6-8
Section 7	CONFIGURATION ANALYSIS	7-1
7.1	Configuration and Processing Descriptions	7-1
7.2	Man-Machine Interaction	7-2
7.3	Hardware Configuration Analysis	7-5
Section 8	REFERENCES	8-1
Appendix A	MSS PRECISION PROCESSING ERROR ANALYSIS	A-1
Appendix B	RBV PRECISION PROCESSING ERROR ANALYSIS	B-1

## ILLUSTRATIONS

Figure		Page
2-1	Monterey - Band 1 - Before Radiometric Correction	E
2-2	Monterey - Band 1 - After Radiometric Correction	E
2-3	MSS Image Showing Striping	E
2-4	MSS Image After Linear Striping Compensation	E
2-5	Scene 1373-17295 Band 6, Detector 1 Histogram	2-4
2-6	Scene 1373-17295 Band 6, Detector 2 Histogram	2-12
2-7	Scene 1045-06560 Band 4, Detector 2 Histogram	2-13
2-8	Scene 1049-17324 Band 4, Detector 2 Histogram	2-14
3-1	Geometric Correction of ERTS Images	3-2
3-2	Input Preparation	3-3
3-3	Mapping Polynomials	3-4
3-4	Monterey - Band 1	E
3-5	Monterey - Band 2	E
3-6	Monterey - Band 3	E
3-7	Monterey - Band 4	E
3-8	Monterey - Band 5	E
3-9	Monterey - Band 6	E
3-10	Monterey - Band 7	E
3-11	Monterey - MSS Color Composite	E
3-12	Phoenix - Band 4	E
3-13	Phoenix - Band 5	E
3-14	Phoenix - Band 6	E

E - These illustrations are contained in the envelope at the back of this report.

ILLUSTRATIONS (Continued)

Figure		Page
3-15	Phoenix - Band 7	E
3-16	Phoenix - MSS Color Composite	E
3-17	Chesapeake Bay - Band 4	E
3-18	Chesapeake Bay - Band 5	E
3-19	Chesapeake Bay - Band 6	E
3-20	Chesapeake Bay - Band 7	E
3-21	Chesapeake Bay - MSS Color Composite	E
3-22	Chesapeake Bay - Band 4 - Linear Counts/Density Relationship	E
3-23	Chesapeake Bay - Band 5 - Linear Counts/Density Relationship	E
3-24	Chesapeake Bay - Band 6 - Linear Counts/Density Relationship	E
3-25	Chesapeake Bay - Band 7 - Linear Counts/Density Relationship	E
3-26	Chesapeake Bay - MSS Color Composite - Linear Counts/Density Relationship	E
4-1	Shape and Size of Reseau Within the Search Area	4-1
4-2	Typical Set of Row or Column Sums	4-3
6-1	Nearest Neighbor Assignment	6-2
6-2	Point Shift Algorithm	6-3
6-3	Bilinear Interpolation	6-5
6-4	Cubic Convolution	6-7
6-5	Monterey - Band 5 - Resampled by Bilinear Interpolation	E

E - These illustrations are contained in the envelope at the back of this report.

## ILLUSTRATIONS (Continued)

Figure		Page
6-6	Monterey - Band 5 - Resampled by Cubic Convolution	E
6-7	Enlargements of Subimage Area	E
6-8	Resampling Error Histograms-Cultural Image	6-11
6-9	Resampling Error Histograms-Natural Image	6-12
6-10	Composite Geometric Correction-Bilinear Interpolation	E
6-11	Composite Geometric Correction-Cubic Convolution	E
6-12	Composite Geometric Correction-Enlargements of Subimage Area	E
7-1	CPU Time vs Processors	7-4
7-2	Configuration A Diagram	7-6
7-3	Configuration A Processing Times	7-7
7-4	Configuration B Diagram	7-9
7-5	Configuration B Processing Times	7-10
7-6	Configuration C Diagram	7-12
7-7	Configuration C Processing Times	7-13
7-8	Configuration D Diagram	7-15
7-9	Configuration D Processing Times	7-17
7-10	Configuration E Diagram	7-19
7-11	Configuration E Processing Times	7-20

E - These illustrations are contained in the envelope at the back of this report.

## TABLES

Number		Page
1-1	SSDA Performance Summary	1-3
2-1	RBV Radiometric Correction Zones	2-3
2-2	Linear Counts/Density Relationship Radiometric Adjustment Table	2-8
3-1	Photographic Products of ERTS Imagery Made By IBM	3-7
3-2	Predicted Output Accuracies (Metres)	3-8
5-1	GCPs From Phoenix-Tucson Area	5-2
5-2	GCPs From Chesapeake Bay Area	5-4
5-3	Effect of Non-Random Sampling Strategies	5-6
5-4	SSDA Results - MSS Data, Phoenix-Tucson Area	5-8
5-5	Registration Success Ratios as a Function of the Temporal Separation Between Search Area and Window Area, Phoenix-Tucson Area	5-10
5-6	SSDA Results - MSS Data, Chesapeake Bay Area	5-13
5-7	Registration Success Ratios as a Function of the Temporal Separation Between Search Area and Window Area, Chesapeake Bay Area	5-14
5-8	Average SSDA Performance for Selected Feature-Band Combinations	5-15
5-9	Effect of Revised Threshold	5-16
6-1	Point Shift Performance	6-4
7-1	Configuration Definitions	7-3
7-2	Configuration A Summary	7-8
7-3	Configuration B Summary	7-11
7-4	Configuration C Summary	7-14

TABLES (Continued)

Number		Page
7-5	Configuration D Summary	7-18
7-6	Configuration E Summary (Without Laser Beam Recorder)	7-21
7-7	Configuration E Summary (With Laser Beam Recorder)	7-22
7-8	Scene Throughput Summary	7-23
7-9	Configuration Cost in Millions of Dollars	7-23
7-10	Per Scene Cost	7-23

## Section 1. INTRODUCTION AND SUMMARY

### 1.1 PURPOSE

This is the final report on IBM's study of All-Digital Precision Processing of ERTS Images. It describes the work performed under contract NAS5-21716 and satisfies Item 5 of Article II of that contract. Some results of additional related studies outside the scope of this contract performed by IBM under its Independent Research and Development (IRAD) program are also described in this report.

The report is organized into seven sections. Section 1 summarizes the study, presents the conclusions which can be drawn from its results, and gives recommendations for future NASA actions. Section 2 discusses the radiometric correction techniques developed. Geometric correction techniques are described in Section 3. Methods for finding reseaux and GCPs in the image data are discussed in Sections 4 and 5, and the results of the investigation of three resampling techniques are presented in Section 6. Section 7 contains the results of the configuration analysis. Two appendices provide the MSS and RBV processing error analyses.

### 1.2 SCOPE OF THE STUDY

The primary purpose of this study was to investigate the feasibility of using all-digital techniques to apply precision-grade radiometric and geometric corrections to ERTS RBV and MSS scenes. To accomplish this, extensive analyses were conducted, the required software routines were designed and developed, and several representative scenes were processed. The results of this processing, in terms of computer performance and output quality, are presented later in this report.

Particular attention was paid to three key areas of the processing. An efficient and very effective method for locating reseaux in RBV images was developed. The Sequential Similarity Detection Algorithm (SSDA) was used to locate GCPs of various types in scenes having temporal separations ranging from 18 to 378 days. Routines to perform geometric correction using bilinear interpolation and cubic convolution instead of nearest neighbor replacement as the resampling technique were developed and applied to one band of one scene.

A secondary purpose of the study was to design and evaluate several candidate configurations for operational systems to process ERTS data. Originally intended to consider only general-purpose digital equipment, this part of the study was expanded to include consideration of I/O media other than computer compatible tape and the use of special-purpose processors. Possible man/machine interaction in the location of GCPs was also added as an area for study.

### 1.3 SUMMARY OF EFFORT

Work on this study began in February of 1972. Many of the required software routines already existed in rudimentary form but required modification to accommodate the unique characteristics of ERTS data. Initial progress was hampered by the delay in the ERTS launch (with its subsequent delay in the dissemination of normal data tapes) and by the idiosyncrasies of the simulated data products which were distributed. U-2 photographs were obtained, scanned, and digitized in an effort to have representative data on which SSDA experimentation could be conducted, but tonal differences between overlapping frames were found to be so great as to preclude meaningful results.

The first post-launch ERTS-1 data tapes were received in August 1972. They revealed numerous deficiencies in the software which had been developed. For example, it was found that the reseau detection routine, which worked well with "nominal" reseaux, gave unacceptable performance with actual RBV images. A new detection program had to be developed.

For IBM, as well as much of the user community, the shutdown of the RBV caused a shift of emphasis to MSS processing. Correction of MSS data proved more difficult than had been anticipated, but the first full precision corrected MSS scenes were produced in February 1973.<sup>1</sup>

The technical work of this study has now been completed, and the following has been accomplished:

- All software required for precision digital correction and annotation of MSS and RBV scenes has been developed.
- Several representative MSS scenes and one RBV scene have been precision corrected and annotated.
- A full program of SSDA experimentation has been completed.
- Several configurations for operational systems have been developed and evaluated.

An IRAD program of related investigations outside the scope of the contract has been defined and completed. Some of the results are included in this report.

### 1.4 CONCLUSIONS

The primary conclusion to be drawn from the results of this study is that digital methods provide a viable technology for the precision-grade geometric and radiometric correction of ERTS RBV and MSS data. The software developed by IBM has been applied successfully to representative ERTS scenes. RMS geometric

errors are on the order of 50 to 60 m in the digital products and 130 to 150 m in the film products. MSS radiometric quality has been described as "excellent" by several observers and is clearly superior to the few precision processed products produced by the NDPF. Radiometric quality of the corrected RBV images is significantly improved relative to the uncorrected images. There are no visible artifacts caused by the zoning technique used, and the correction appears to be as good as can be accomplished with the existing calibration data.

A successful reseau detection algorithm has been developed. It will find the 81 reseaux in an RBV image in less than 10 seconds, using an IBM 370/155. In tests on six RBV images (486 reseaux) it had 100 percent success in locating the reseaux. Its probability of false reseaux detection is on the order of  $1 \times 10^{-5}$ .

It has been shown that the SSDA provides a technique around which an operational GCP detection routine can be built. Successful locations of some types of features have been demonstrated for temporal separations as large as 378 days (the largest separation for which IBM obtained data). Table 1-1 summarizes the types of features that make the best GCPs, the spectral bands in which they should be located, the probability of detection, and average detection times on an IBM 370/155.

Table 1-1

SSDA PERFORMANCE SUMMARY

<u>Best GCP Feature Types</u>	<u>Best Spectral Band</u>	<u>Probability of Detection</u>	<u>Average Detection Time (Sec)*</u>
Large Land-Water Interfaces	7	0.88	2.08
Mountain Peaks, Hills	5	1.00	8.44
Airports	7	0.81	15.44
Interstate-Grade Highways	5	0.93	2.33

\*On an IBM 370/155 computer

Resampling by bilinear interpolation and cubic convolution (as well as by the nearest neighbor assignment technique used for most of the processing under this contract) has been implemented and applied to a sample image. Conclusions as to whether or not the increased processing cost of the more complex resampling techniques is justified by an increase in output quality requires further analysis and must come from the user community.

The configuration analysis has shown that digital systems for correcting ERTS data on an operational, production basis are economically feasible. Great increases in throughput can be achieved by the use of high-speed I/O and high-speed microprogrammable processors.

## 1.5 RECOMMENDATIONS

The results of this study lead to the following recommendations for future NASA actions:

- a. Future ground systems for earth resources satellites should be based on digital (as opposed to electro-optical) technology. In the near future, digital processing will be able to produce better quality products in a more cost-effective manner than electro-optical processing.
- b. In future systems involving high throughput, input and output to the processors should be by a high-speed means such as high density digital tape. Conversion to low density computer tapes, when required, should be performed off-line so as not to slow down the processors with low-speed I/O operations.
- c. Microprogrammable processors should be seriously considered for future systems. Although the exact throughput requirements can influence the configuration, special-purpose systems are generally more cost-effective than general-purpose systems for the highly repetitive inner loop operations characteristic of digital image processing. Microprogrammable processors provide a degree of flexibility that is difficult to attain with hard-wired equipment and are, therefore, better choices for the experimental multi-mission sensor programs of the near future. General-purpose equipment should still be used for the infrequent, complex, high-precision calculations needed to support image processing; for low-throughput image processing applications; and for image processing research and development.
- d. The present ERTS byte-pair interleaved CCT format is not ideal from a processing standpoint. If the CCT data were

spectrally separated (at least on a line-by-line basis), radiometric correction could be accomplished more efficiently. A single correction table would be valid for thousands of consecutive samples, and the overhead of referencing different correction tables would be greatly reduced. On the other hand, byte interleaved data aids the geometric correction process, since the resampling parameters can be computed once and applied to four consecutive samples. Data that is spectrally separated by scene makes film recording easier; but byte interleaved data is preferable for computer-implemented multispectral classification, since it eliminates the need to merge separate data streams.

The choice between byte interleaved and spectrally separated data is a difficult one. It depends largely upon the equipment to be used for processing and the intended use of the processed data. However, the present byte-pair interleaved format possesses the advantages of neither byte interleaved nor spectrally separated data and should be changed, if that can be accomplished without creating a format conversion problem in the user community.

- e. Accurate format center coordinates and normalized spacecraft velocity ( $\Delta V/V$ ) should be added to the header on the present ERTS CCTs. This would permit users to perform systematic corrections without the need for Bulk Image Annotation Tape (BIAT) data dumps. If the attitude and altitude data presently included on the BIAT were added to the CCT headers, still more accurate corrections would be possible.
- f. Future RBV pre-launch calibration should completely span the image area, especially the edges and corners. Such calibration should alleviate some of the problems that were encountered in RBV radiometric correction.
- g. During the study of methods to eliminate striping in the MSS data, it was discovered that histograms of the individual detectors displayed characteristics which indicated possible errors somewhere in the NASA sensor/calibration chain. This should be investigated further.
- h. NASA should fund a study to develop a fully-automatic (though, perhaps, man-monitored) GCP detection program based on the SSDA. The study should include extensive testing using the ERTS data which has been collected since July 1972. Such a study should be performed under Government supervision and funding.

- i. NASA should also fund a study to compare the results of the three sampling techniques presently being used for ERTS data. Several different scenes should be processed, and the impact upon both human interpretation and machine processing in a variety of applications areas should be evaluated.

#### 1.6 NEW TECHNOLOGY

No new technology was discovered during the course of this contract.

## Section 2. RADIOMETRIC CORRECTION

The radiometry of both the ERTS RBV and MSS was changed to correct and enhance the images. The MSS has 24 detectors, each of which has unique response characteristics, while the RBV radiometric response varies over the image.

### 2.1 RBV RADIOMETRIC CORRECTION

The ERTS RBV CCTs contain image data which has been sampled and digitized with 6-bit quantization. There are thus only 64 possible input data values. If a table which specifies the correct output intensity for each of the 64 possible input intensities can be defined, radiometric correction of the RBV images can be accomplished by a simple table lookup operation.

This is essentially the technique used by IBM. It is complicated somewhat by the fact that the RBV radiometric errors vary across the image, requiring the use of multiple correction tables. RBV radiometric correction is thus conducted in two parts: generation of the correction tables (an off-line operation) and application of the correction.

#### 2.1.1 Generation of RBV Radiometric Correction Tables

Pre-flight calibration provides readings at several intensity levels from a uniform light source, a Hovis Sphere, taken at an 18x18 array of points across the RBV image. These readings are in terms of voltage ranging from 0.32 to 1.10, so they are first scaled to the digital range 0 to 63. From these uniform input values, 18x18 arrays of gain(G) and bias(B) values are computed for the correction equation:

$$V_{out} = (V_{in} + B)G \quad (1)$$

The uniform input readings are distributed uniformly throughout the image, but do not include the edges. Various extrapolation techniques of up to third order were used to estimate the edge data, but due to the radical radiometric distortion near the edges, zero order extrapolation proved to produce the best results.

These computations finally produce 20x20 arrays of gain and bias that completely span the image. These values can be fit in a least squared error sense with functions B(X,Y) and G(X,Y). We now have a general expression:

$$V_{out}(X,Y) = [V_{in} + B(X,Y)]G(X,Y) \quad (2)$$

Although (2) could be used to compute a radiometric correction for every (X,Y) point in the image, this would be quite costly. It is computationally more efficient to divide the image into zones in which constant values of B and G can be used with acceptably small error. Such a zoning of the image can be accomplished by variations on the solution to the following problem:

Given a specific input value  $V_o$  at point  $(X_o, Y_o)$  of the image and bias and gain values

$$B_o = B(X_o, Y_o)$$

$$G_o = G(X_o, Y_o)$$

find the distances  $\Delta X$  and  $\Delta Y$  such that

$$\left| \Delta V_{out} \right| \leq K$$

Now

$$\Delta V_{out} = \frac{\partial V_{out}}{\partial X} \Delta X + \frac{\partial V_{out}}{\partial Y} \Delta Y \quad (3)$$

$$\begin{aligned} \frac{\partial V_{out}}{\partial X} &= \frac{\partial V_{out}}{\partial B} \frac{\partial B}{\partial X} + \frac{\partial V_{out}}{\partial G} \frac{\partial G}{\partial X} \\ &= G_o \frac{\partial B}{\partial X} \bigg|_{X_o, Y_o} + (V_o + B_o) \frac{\partial G}{\partial X} \bigg|_{X_o, Y_o} \end{aligned} \quad (4)$$

and

$$\begin{aligned} \frac{\partial V_{out}}{\partial Y} &= \frac{\partial V_{out}}{\partial B} \frac{\partial B}{\partial Y} + \frac{\partial V_{out}}{\partial G} \frac{\partial G}{\partial Y} \\ &= G_o \frac{\partial B}{\partial Y} \bigg|_{X_o, Y_o} + (V_o + B_o) \frac{\partial G}{\partial Y} \bigg|_{X_o, Y_o} \end{aligned} \quad (5)$$

Equation (3) presents a problem of one equation and two unknowns. There are two methods of circumventing this problem:

- a. Assume a relationship between  $\Delta X$  and  $\Delta Y$  (e.g.,  $\Delta X = \Delta Y$ , or  $\Delta X = (4608/4125) \Delta Y$ )
- b. Solve the problem as two one-dimensional problems.

A procedure based on the second method has been developed.<sup>2</sup> Intrinsic to the procedure is the assumption that the effects of the correction function are more severe at the edges of the image than at the center. Since the principal radiometric effect is shading, this assumption appears well justified. The zoning generated by this procedure is conservative in that it processes the entire image with zones computed from "worst case" conditions at the image edges.

For each zone, constant values of G and B are computed. These values are then used with equation (1) to generate a table of correct values for the 64 possible input values.

This procedure was applied to the three RBV bands of scene 1002-18134. It took approximately 165 seconds per band on a 370/155 to perform the fitting, zoning, and table generation process. The results, in terms of the number of zones generated, are given in Table 2-1.

Table 2-1

RBV RADIOMETRIC CORRECTION ZONES  
Scene 1002-18134

	<u>Horizontal</u>	<u>Vertical</u>	<u>Total</u>
Band 1	191	138	26,358
Band 2	184	119	21,896
Band 3	181	106	19,186

### 2.1.2 Correction Application

In a production system, the RBV radiometric correction can be applied during the operation of the Point Shift geometric correction process. During this process, a buffer of input image lines is kept in computer memory. This

buffer is updated a line at a time as the correction process moves down an image.

As each new line of input image data is read into the buffer, the line count can be consulted to determine the vertical correction zone. As each new vertical zone is reached, a new set of horizontal zones can be read into main storage and used to correct that set of lines. The horizontal zones divide the input line into segments, each one of which has its own distinct correction table.

Segments up to 256 pixels in length can be corrected with a single Translate instruction. Segments greater than 256 pixels in length would be corrected in 256 pixel pieces, except for the final piece which is generally less than 256 pixels long. This is required by the eight bit limitation on the field of the Translate instruction which specifies the number of bytes to be processed.

An alternative method would be to store the gain and bias values on supplemental storage and generate the horizontal zone tables as they are needed in the image correction process. In the first method, 4.1M bytes of supplemental storage are necessary to store the tables; in the alternate method, 0.5M bytes are needed. However, the image correction process in the first method takes about 45 seconds on an IBM 370/155, while the second method takes 100 seconds.

### 2.1.3 Results

The radiometric correction procedure described above was applied to the three RBV bands of scene 1002-18134. The fully corrected images are presented in Section 3. A "before and after" pair showing the effects of radiometric correction only is presented in Figures 2-1 and 2-2. Comparison of the figures shows that although the correction significantly improves image shading, it is not perfect. Along the edges, and especially in the corners, radiometric distortion is still apparent. This is due to the fact that the preflight calibration data is taken at points interior to the image area and does not include the edges where distortion is quite severe. It should be possible to obtain better edge results with calibration data that extends over the entire image area.

Careful examination of the figures reveals a regular pattern of vertical lines. Computer shade prints show that these lines are in the original CCT data. Their cause is unknown to IBM.

## 2.2 MSS RADIOMETRIC CORRECTION

The MSS CCTs generated by the ERTS NDPF are radiometrically corrected. Thus, strictly speaking, there was no need for IBM to radiometrically "correct" the MSS data which was obtained during this study. If it were

Figures 2-1 and 2-2 are contained in the envelope at the back of this report.

desired to include a radiometric correction in a digital correction system, the basic procedure used by the NDPF would be used. Correction tables for each detector would be generated and updated as required, based on the calibration data received. Application of the correction could occur at one of several places in the processing stream. As the discussion of Section 7 shows, radiometric correction early in the processing stream, using loadable special-purpose equipment, appears to be an attractive solution.

Although the MSS data did not have to be corrected, it did have to be "adjusted" so that it would produce the desired results when recorded on film by the recorder used by IBM. This adjustment is a transformation that provides a film gamma compensation for a particular film and recorder combination but does not alter the quality of the digital data. In addition, an attempt was made to eliminate the residual striping present in the CCT data.

#### 2.2.1 . MSS Radiometric Adjustment

Two distinct methods of radiometric adjustment can be applied to the MSS scenes, each yielding a separate output product. In the first, independent enhancements are made for each scene to produce final images having radiometric qualities pleasing to the eye. In the second method, a standard correction which attempts to produce a fixed relationship between calibrated sensor counts and film density is applied to all images.

##### 2.2.1.1 Scene Dependent Enhancement for Pleasing Radiometric Quality

For each band of an MSS scene, the following procedure is used to determine the radiometric enhancement to be used:

- a. Select a representative subimage
- b. Apply several (typically four or eight) different radiometric adjustments to this subimage
- c. Expose on film and develop each of these adjusted subimages
- d. By visual comparison and inspection, select the enhancement providing the best radiometry.

It should be noted that this method involves an independent and subjective evaluation for each scene processed.

Most of the sample corrected images presented in Section 3 were processed this way.

### 2.2.1.2 Standard Radiometric Adjustment

MSS scenes can also be processed with a standard scene-independent radiometric adjustment. This adjustment is defined by the two requirements that (1) a linear relationship exist between sensor count and film density and (2) the film density have a range of approximately 2.0. (The actual range used was 0.1 - 2.1.) The table which effected this adjustment is given in Table 2-2. The relationship given in the table is a function of the IBM Drum Scanner/Plotter characteristics, the film used, and the developing techniques used in the photographic laboratory. A version of scene 1080-15192 adjusted in this manner is presented in Section 3.

### 2.2.2 Striping Removal in MSS Scenes

Striping, or horizontal banding, is evident in numerous MSS scenes. Using IBM IRAD funding, an investigation was undertaken to determine a means of removing this striping from the output products. Initially, it was hoped that a set of gain and bias coefficient  $[(g_i, b_i), i=1, \dots, 6]$  could be determined by measuring detector responses in areas of uniform radiance, so that for a given detector in a given band an adjustment of the form  $x'=(x+b_i)g_i$  would remove the striping. Moreover, it was hoped that these coefficients would remain relatively constant so that they would require only occasional adjustment and could then be applied to all MSS scenes for some period of time. Both of these hoped-for results proved unrealistic. Partial success was achieved on individual scenes, but striping was never completely removed, and the correction applied to one scene would not work for any other scene. Typical results are shown in Figures 2-3 and 2-4.

When a linear correction based on detector responses in areas of uniform radiance proved insufficient, it was thought that a non-linear correction which would adjust the histograms of all detectors in a band to some standard form might be possible. To this end, detector histograms over entire images were compiled. Typical histograms are presented in Figures 2-5 through 2-8.

Since the histograms were generated from MSS CCTs produced by the ERTS NDPF, they represent data which has been radiometrically corrected. The original MSS data contains at most 64 unique values. Therefore, unless the calibration tables are altered during a scene, there should be no more than 64 unique values on a CCT for any given detector. Figures 2-5 through 2-8 all show more than 64 unique values, which indicates that the calibration tables applied to the original MSS data were changed at least once during each of the three scenes represented.

Table 2-2

LINEAR COUNTS/DENSITY RELATIONSHIP  
RADIOMETRIC ADJUSTMENT TABLE

IN	OUT	IN	OUT	IN	OUT	IN	OUT
00	48	32	148	64	175	96	199
01	56	33	149	65	175	97	200
02	64	34	150	66	176	98	200
03	72	35	151	67	176	99	201
04	80	36	152	68	177	100	202
05	84	37	153	69	177	101	203
06	88	38	154	70	178	102	204
07	93	39	155	71	178	103	206
08	98	40	156	72	179	104	207
09	101	41	158	73	179	105	207
10	104	42	160	74	180	106	208
11	107	43	161	75	180	107	209
12	110	44	163	76	181	108	210
13	112	45	163	77	181	109	211
14	114	46	164	78	182	110	212
15	118	47	165	79	183	111	214
16	122	48	165	80	184	112	216
17	124	49	166	81	184	113	218
18	126	50	166	82	185	114	220
19	129	51	167	83	186	115	222
20	132	52	167	84	187	116	224
21	133	53	168	85	187	117	226
22	134	54	168	86	188	118	228
23	135	55	169	87	190	119	229
24	136	56	170	88	192	120	230
25	139	57	171	89	194	121	230
26	141	58	172	90	196	122	231
27	142	59	172	91	196	123	232
28	143	60	173	92	197	124	233
29	144	61	173	93	198	125	235
30	145	62	174	94	198	126	238
31	147	63	174	95	199	127	241

Note: All values shown are decimal. The table assumes 7-bit input data. For 6-bit input data, the input values should be doubled prior to entry to the table.

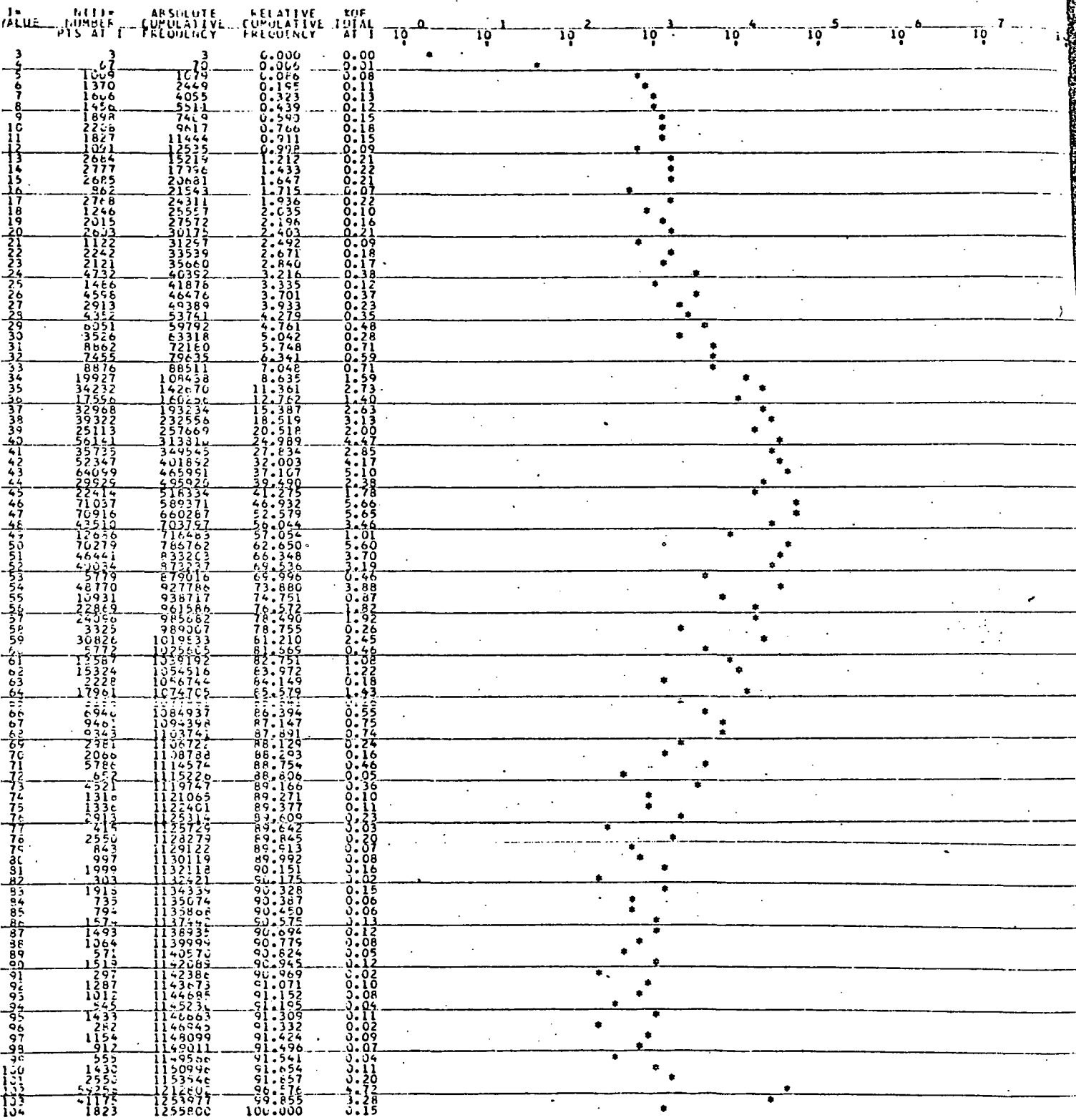
Figures 2-3 and 2-4 are contained in the envelope at the back of this report.

It would be expected that the corrected outputs of adjacent detectors in a given spectral band would have very similar histograms over a scene. For the data shown in Figures 2-5 and 2-6, this is not the case. The data of Figure 2-5 shows what might be expected in the presence of changing calibration tables. On the other hand, the "multi-curve" nature of Figure 2-6 is quite unusual. The two figures plainly show that there will be striping in the band 6 image. Since the radiometric correction process of the NDPF should have eliminated differences in detector responses, a thorough examination of that process appears warranted.

No simple transformation will make the data of Figure 2-6 agree with that of Figure 2-5. Therefore, so long as the CCTs contain data with the characteristics shown in the figures, no simple striping removal procedure will be successful.

The general shapes of the histograms in Figures 2-7 and 2-8 are not strikingly dissimilar. Thus, it was hoped that a striping correction computed for one of the scenes would be applicable to the other. This did not prove to be the case, however. When a correction which significantly decreased striping in scene 1045-06560 was applied to scene 1049-17324, the striping in the latter scene was made slightly worse. From this, it appears that it is not likely that a striping correction which will remain constant for relatively long periods of time can be devised.

HISTOGRAM OF DETECTOR 1 SUBIMAGE



ALL LEADING AND TRAILING VALUES OF I WITH N(I) = 0 ARE OMITTED FROM THE GRAPH

MEAN = 51.4058

RMS = 55.02333

STANDARD DEVIATION = 19.42465

END OF CASE INPUT REACHED

Figure 2-5. Scene 1373 - 17295 Band 6, Detector 1 Histogram

HISTOGRAM OF DETECTOR 2 SURFACE

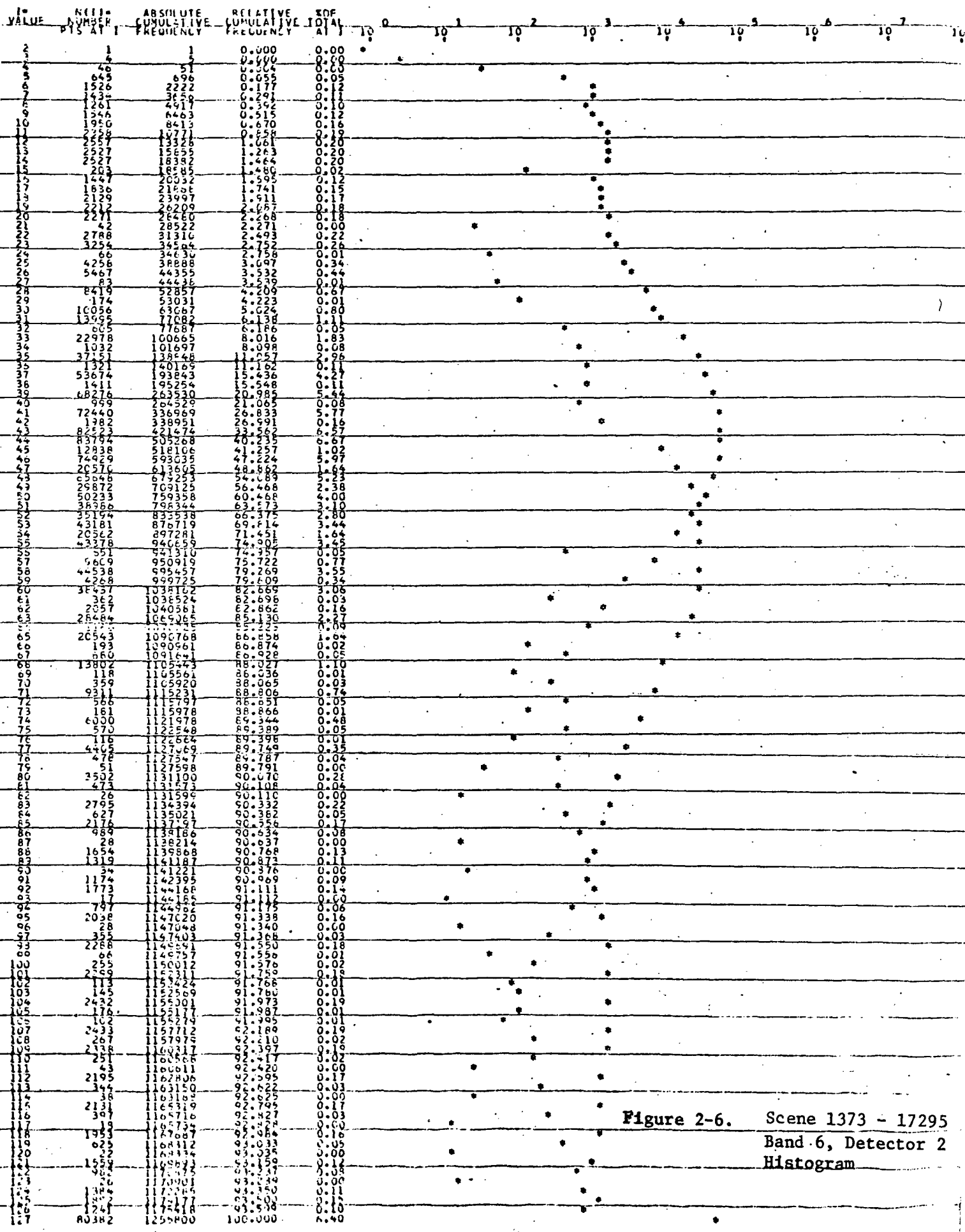


Figure 2-6. Scene 1373 - 17295  
Band 6, Detector 2  
Histogram

ALL LEADING AND TRAILING VALUES OF L WITH N(I) = 0 ARE OMITTED FROM THE GRAPH

HISTOGRAM OF DETECTOR 2 OUTPUT

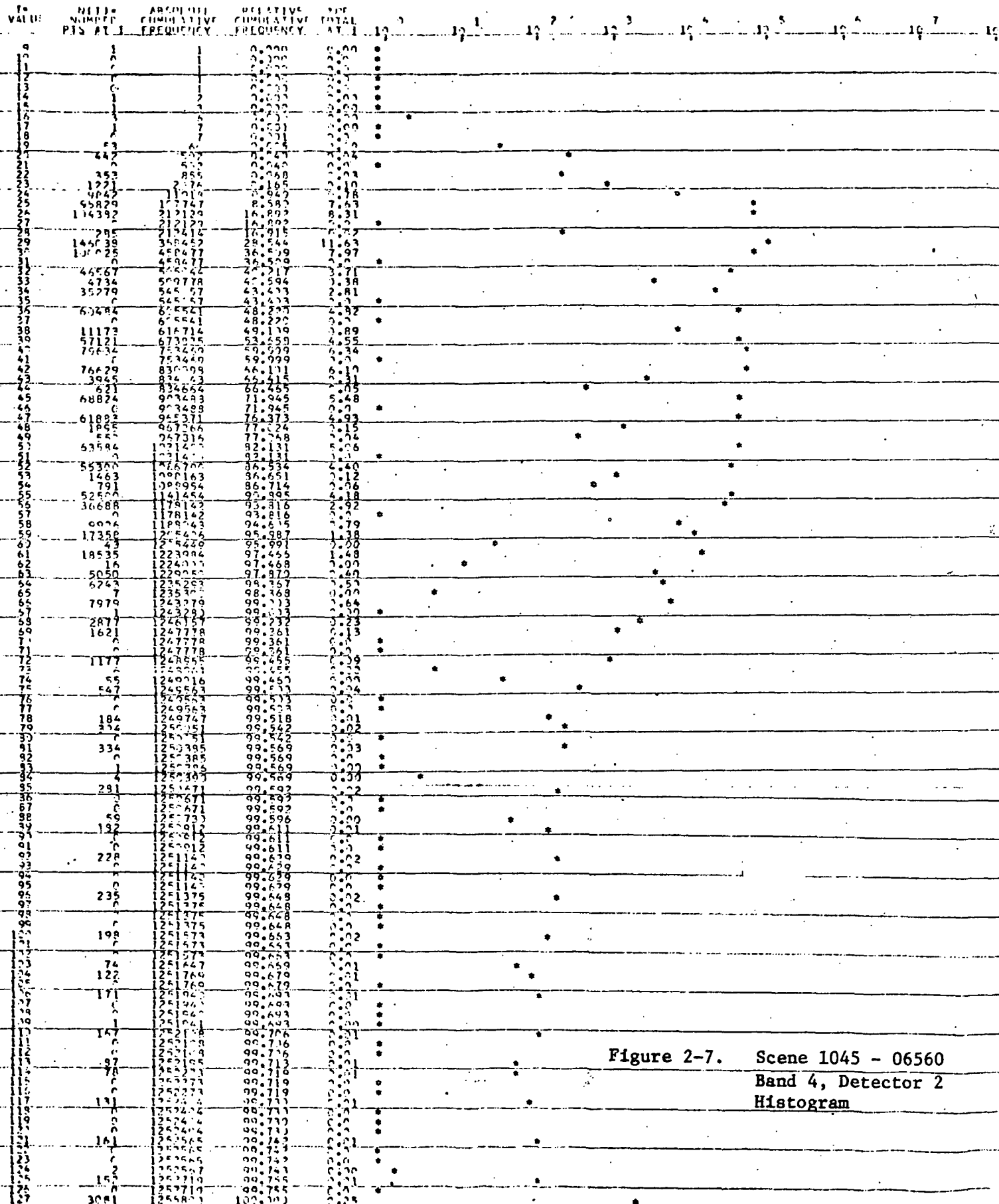


Figure 2-7. Scene 1045 - 06560  
Band 4, Detector 2  
Histogram

ALL LEADING AND TRAILING VALUES OF L WITH REL# 2 ARE OMITTED FROM THE GRAPH

MEAN= 39.2295 RMS= 41.6912 STANDARD DEVIATION= 12.2316  
END OF CARD INPUT REACHED



## Section 3. GEOMETRIC CORRECTION

### 3.1 GEOMETRIC CORRECTION TECHNIQUES

IBM's method of creating geometrically corrected film and CCT imagery from NASA Bulk CCTs is shown in Figure 3-1. In this process there are six steps which are functionally the same for both RBV and MSS images. How each of these functions is accomplished for each type (RBV or MSS) of image is described below in subsections 3.1.1 through 3.1.6.

#### 3.1.1 Reformat Image Data

Most of IBM's image processing programs are designed to accept digital images in the format of one record per line of image data. For most purposes, this is the most suitable format. Consequently, the data on NASA CCTs is reorganized into the above format and stored on IBM computer tapes. A separate tape data set is created for each spectral band. Since the formats of the NASA Bulk RBV and MSS CCTs are different, separate reformatting programs are used.

#### 3.1.2 Prepare Input

In this step, the inputs required for the rest of the process are prepared. There are four different inputs that may be needed, and each is described below. Functional flow charts for this task are shown in Figure 3-2.

##### 3.1.2.1 SIZES/BIAT/GCP Data Set (RBV and MSS)

A disk data set that is used by the modeling programs is created. It contains the sizes of both the output and input images, the maximum gridding size, the minimum gridding error allowed, format center and nadir locations (from BIAT), and (for MSS only) the normalized spacecraft velocity error (from BIAT). It also contains the nominal (UTM coordinates) and observed (input image pixel coordinates) locations of ground control points in the image. The observed GCP locations may be found either manually or automatically.

##### 3.1.2.2 Reseau Detection (RBV Only)

A disk data set containing the observed reseau locations (input image pixel coordinates) is created. IBM has developed an efficient algorithm for automatically locating reseaux. All 81 reseaux are located in less than 10 seconds CPU time on an IBM 370/155 computer. The algorithm developed and used by IBM to locate reseaux in an RBV bulk image is described in Section 4.

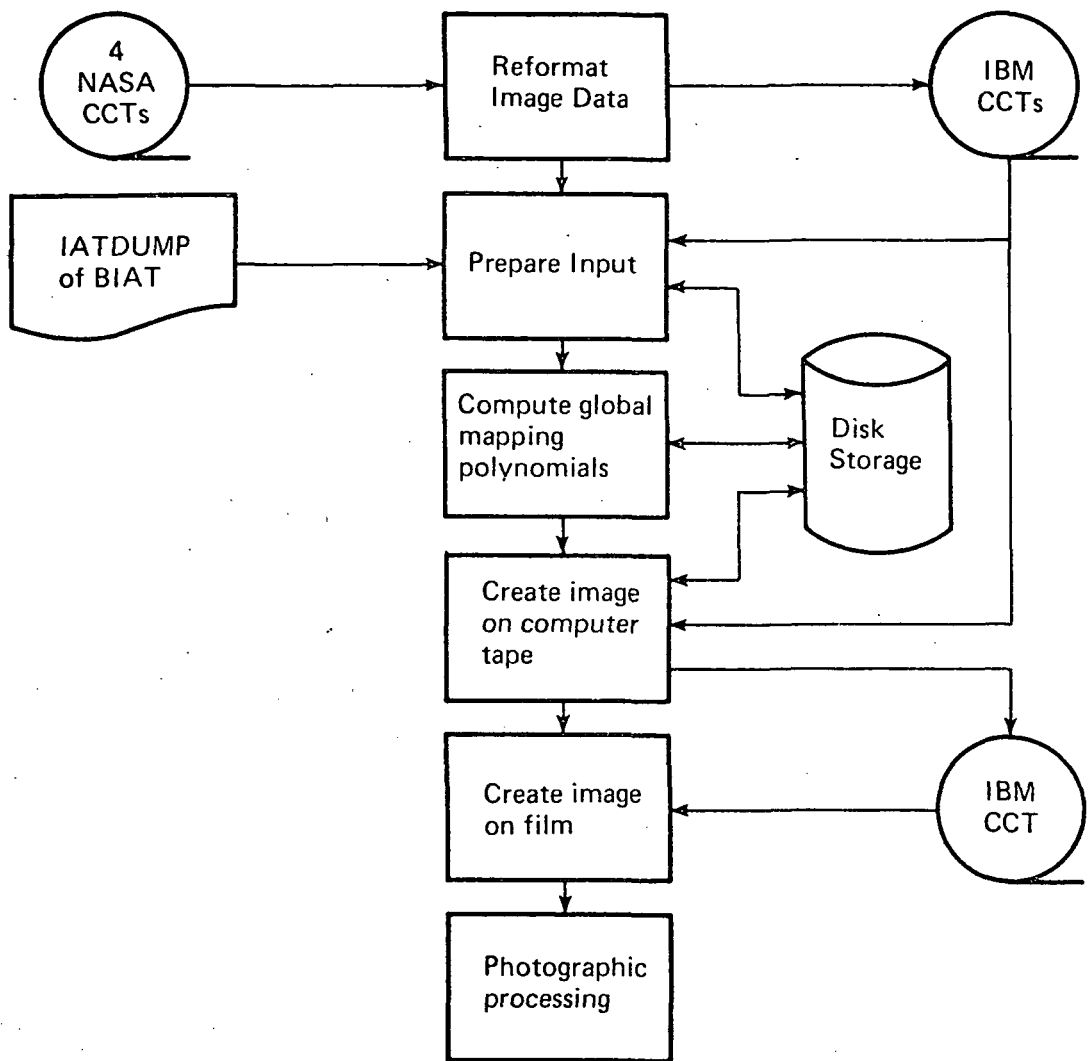
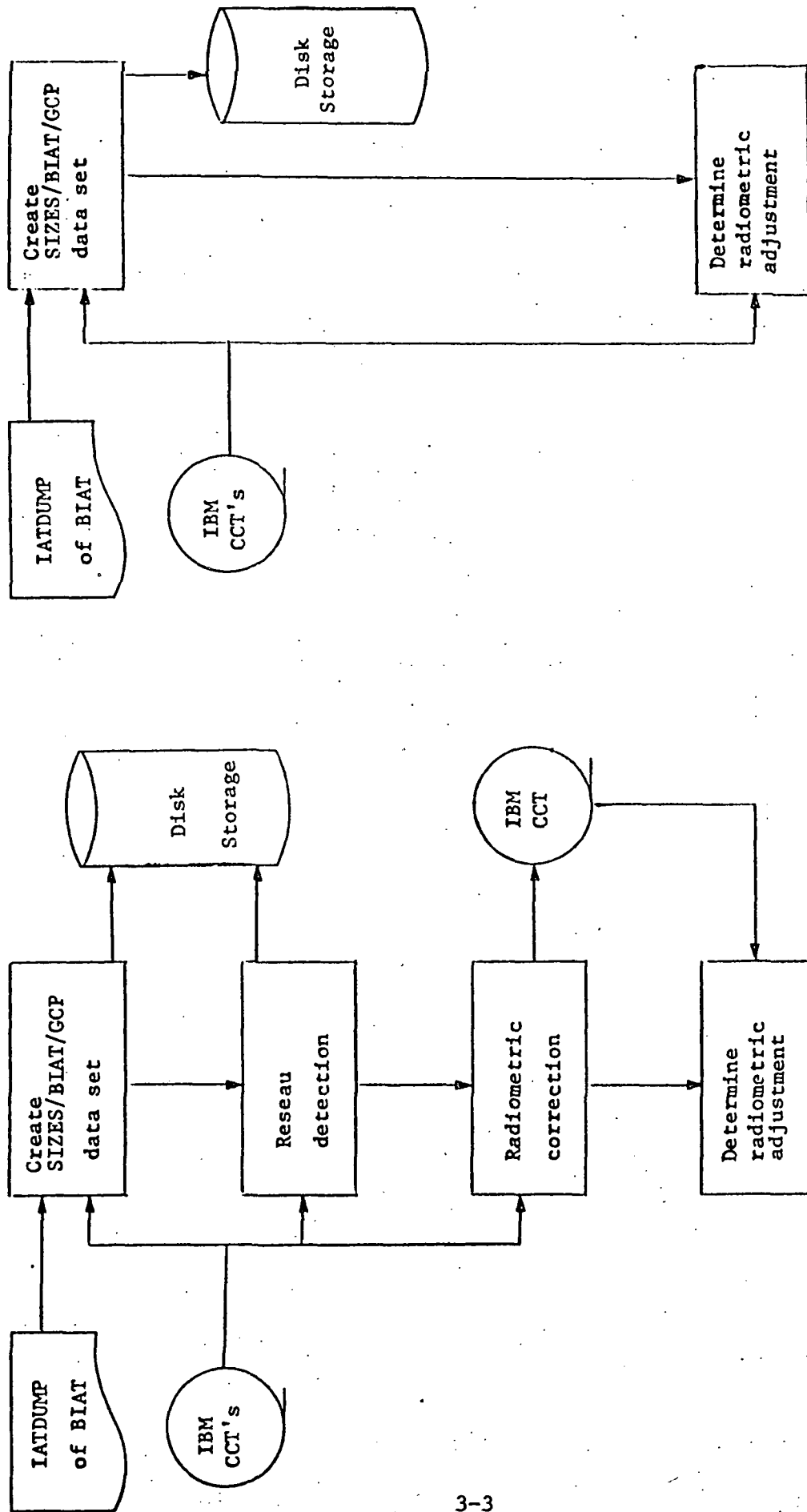


Figure 3-1. Geometric Correction of ERTS Images



MSS

RBV

Figure 3-2. Input Preparation

### 3.1.2.3 Radiometric Correction (RBV Only)

For each band, a radiometrically corrected image is created on a computer tape data set. The zoned, table look-up process described in Section 2.1 is used, but the correction is applied prior to (rather than during) the Point Shift operation. Since MSS data is already radiometrically corrected, no further correction is applied.

### 3.1.2.4 Radiometric Adjustment (RBV and MSS)

If a radiometric adjustment is desired, the tables to be used are determined. Adjustment is often required to make certain information more visible or to make image intensity values fall within the correct range for a particular film recording device.

### 3.1.3 Compute Global Mapping Polynomials

IBM uses a pair of global polynomials in two variables to define the transformation used in the geometric correction of a digital image. The function that these global polynomials define is a mapping from the output (i.e., geometrically correct) image to the input image, as shown in Figure 3-3.

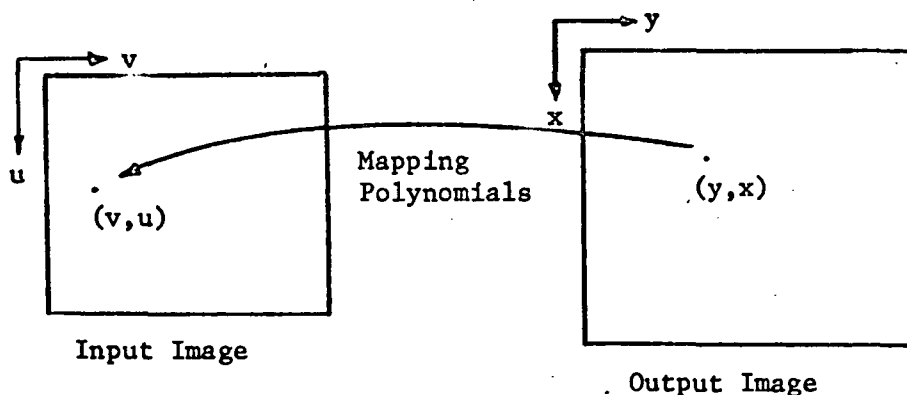


Figure 3-3. Mapping Polynomials

Specifically,

$$v = \bar{v}(y,x)$$

$$u = \bar{u}(y,x)$$

where  $\bar{v}$  and  $\bar{u}$  are polynomials. IBM has found that 5th degree polynomials with all terms included are quite adequate for accurate modeling the errors of ERTS images.

#### 3.1.4 Create Image on Computer Tape

In this part of IBM's precision processing, a fully annotated image is written on computer compatible tape in a format suitable for film recording on the IBM Drum Scanner/Plotter. This format is one data record on tape for each image line. In this section, the "image" represents one band of an ERTS scene, including all of the annotation and ground image data. Annotation and ground image data are organized to form the image in a single computer load module.

##### 3.1.4.1 Image Annotation

IBM includes both identification information and tick marks in the annotation on its precision processed imagery. Some of the identification information is obtained from the first two records on the NASA Bulk CCT. The rest of the identification information and the data needed to include tick marks is supplied by the error modeling routine that calculates the global mapping polynomials. Tick marks are located within a border surrounding the ground image data. On the inner edges of this border are UTM tick marks, and on the outer edge are geodetic latitude and longitude tick marks.

##### 3.1.4.2 Ground Image Data

The ground image data is constructed by resampling the data from the IBM computer tape constructed during the reformatting step. Theoretically, the global mapping polynomials could be used to compute the input space coordinates for every output image pixel. This method would involve the evaluation of two 5th degree, 21-term polynomials for more than 14 million output image points, which would be extremely time consuming on any computer. A more efficient method (from a computer cost point of view) is to map only a few key points with the global mapping polynomials and to locate the remaining points by bilinear interpolation. If these key points are chosen so that the error introduced by this method is very small, then this is an efficient method of performing the output image to input image mapping.

IBM uses a rectangular array of key points (called "interpolation grid points") to perform the mapping. The points are selected so that the interpolation error is less than 0.1 pixels. However, due to the characteristics of the Move Character (MVC) instruction (OS Assembler Language),

the key points are required to be no further than 256 pixels apart. This constraint, rather than the 0.1 pixels maximum interpolation error, has been the dominating factor in all MSS images processed by IBM so far. With this constraint, the interpolation grid mesh is always 17x17 for MSS images. For RBV images, the error bound is sometimes reached. Typically 20 to 24 grid points, horizontally and vertically, are required for RBV images.

Once an output image point has been mapped into the input image space, a radiometric intensity must be assigned to it. Since the output point location generally does not coincide with the location of any input point, the input space must be resampled at the output point location to obtain this intensity.

One resampling method used by IBM is nearest neighbor assignment. The intensity of the nearest input pixel is assigned to the output pixel in question. When this is done, lines in the output image are composed of segments of lines from the input image. The mapping polynomials permit the lengths of the segments to be calculated. Entire segments (3 to 9 pixels long in the work done under this contract) can then be moved from the input space to the output space with a single MVC instruction. This is the basis of IBM's Point Shift Algorithm, which is a very efficient method of applying a geometric correction.<sup>3,4,5</sup>

Other resampling techniques have also been implemented. Section 6 presents the results of applying bilinear interpolation and cubic convolution to a sample image.

### 3.1.5 Create Image on Film

The device used to record the precision processed images on black and white photographic film is the IBM Drum Scanner/Plotter. This machine can plot an image of any size up to about 760mm wide by 610mm high. It plots a square, non-overlapping spot and has three possible spot sizes: 25  $\mu\text{m}$  x 25  $\mu\text{m}$ , 50  $\mu\text{m}$  x 50  $\mu\text{m}$ , and 100  $\mu\text{m}$  x 100  $\mu\text{m}$ . To obtain an image at 1:1 000 000 scale, IBM has used the 50  $\mu\text{m}$  spot. This requires a change of scale from the NASA bulk image, which has a non-square input picture element (pixel). All necessary scale change has been included when calculating the global mapping polynomials. Some of the images have also been recorded on film with the 100  $\mu\text{m}$  spot, resulting in a 1:500 000 scale image. The IBM Drum Scanner/Plotter is capable of creating a first generation negative or a first generation positive transparency. It is usually necessary to perform a different radiometric adjustment of the data, for a positive rather than for a negative.

### 3.1.6 Photographic Processing

Once film has been exposed by the IBM Drum Scanner/Plotter, a variety of second generation photographic images may be made. The types of products made by IBM from ERTS imagery are listed in Table 3-1.

Table 3-1

PHOTOGRAPHIC PRODUCTS OF ERTS IMAGERY MADE BY IBM

---

<u>Photographic Generation</u>	<u>Type of Product</u>	<u>Process Used</u>
1	B/W negatives	IBM Drum Scanner/Plotter
1	B/W positive transparencies	IBM Drum Scanner/Plotter
2	B/W positive transparencies	Contact printing
2	B/W positive prints	Contact printing
2	False color prints	Three band sequential contact printing
2	False color transparencies	Three band sequential contact printing
3	Color negative	Enlargement of false color transparency

---

## 3.2 RESULTS

### 3.2.1 Error Analyses

Error analyses of both MSS and RBV processing were performed. This work is described in detail in Appendices A and B. Briefly, the analyses predicted the output accuracies shown in Table 3-2.

Table 3-2

## PREDICTED OUTPUT ACCURACIES (METRES)

	Relative Error		Absolute Error	
	<u>RMS</u>	<u>Max</u>	<u>RMS</u>	<u>Max</u>
RBV				
Digital Output	41.8	48.7	35.8	44.6
Film Output	56.6	61.9	52.4	58.8
MSS				
Digital Output	66.9	124.1	78.1	127.1
Film Output	82.2	133.0	91.6	135.8

## 3.2.2 Calculated Accuracies

The mapping polynomials generated during the geometric correction process can be used to determine geometric errors for points for which both geodetic and image coordinates are known. This has been done for several of the scenes processed with the following typical results:

- RBV bands 1, 2, and 3, of scene 1002-18134 had RMS errors of 53.1 m, 52.1 m, and 56.4 m respectively.
- MSS scene 1002-18134 had an RMS error of 66 m.
- MSS scene 1062-1590 had an RMS error of 61 m.
- MSS scene 1080-15192 had an RMS error of 69 m.

The locations of 22 features in scenes 1062-15190 and 1080-15192 were compared. When the average translational differences were removed, the RMS residual error was 67.2 m, the maximum error was 148.0 m, and 90 percent of the points had errors less than 85.8 m. This shows that good registration can be obtained between temporally separated scenes of the same area.

### 3.2.3 Measured Accuracies

Computer shade prints were used to determine the output array locations of 30 features in scene 1062-15190. These actual locations were compared with the nominal locations as determined from UTM coordinates. The maximum error observed as 114 m, and the RMS error was 45 m.

Band 5 of scene 1062-15190 was recorded on film and provided to Dr. Robert McEwen of the USGS for evaluation. Using 21 control points in the image, he measured absolute and relative RMS errors of 135 m.<sup>6</sup>

An APL program was used to estimate the mapping errors for 9 features in each of the RBV bands of scene 1002-18134. The RMS and maximum errors were 38 and 62 m, respectively.

### 3.2.4 Sample Photographic Products

Figures 3-4 through 3-26 present second generation black and white positive prints and color composite prints of the following scenes:

- RBV 1002-18134
- MSS 1002-18134
- MSS 1031-17325
- MSS 1080-15192.

For all of the above, a radiometric adjustment was applied to obtain photographs with good information extraction potential. In addition, Figures 3-22 through 3-26 present MSS scene 1080-15192 radiometrically adjusted to achieve a linear sensor count to film density relationship.

Figures 3-4 through 3-26 are contained in the envelope at the back of this report.

Section 4. RESEAU DETECTION AND LOCATION

A reseau pattern composed of a 9x9 array of opaque cruciform marks is inscribed on the RBV faceplate to provide the means of determining the geometric distortion introduced by the sensor. The mathematical characterization of the sensor-caused error in a given image requires the detection and precise location of the nominally black reseau marks in that image. The vector differences between the actual locations and the undistorted locations of the reseau marks are used to compute the coefficients of the bivariate mapping polynomials pertaining to the internal errors of the RBV.

The internal geometric errors of the RBV are very stable. A 50x50 pixels search area centered at the last known location of the reseau is sufficiently large to insure that it contains the reseau.

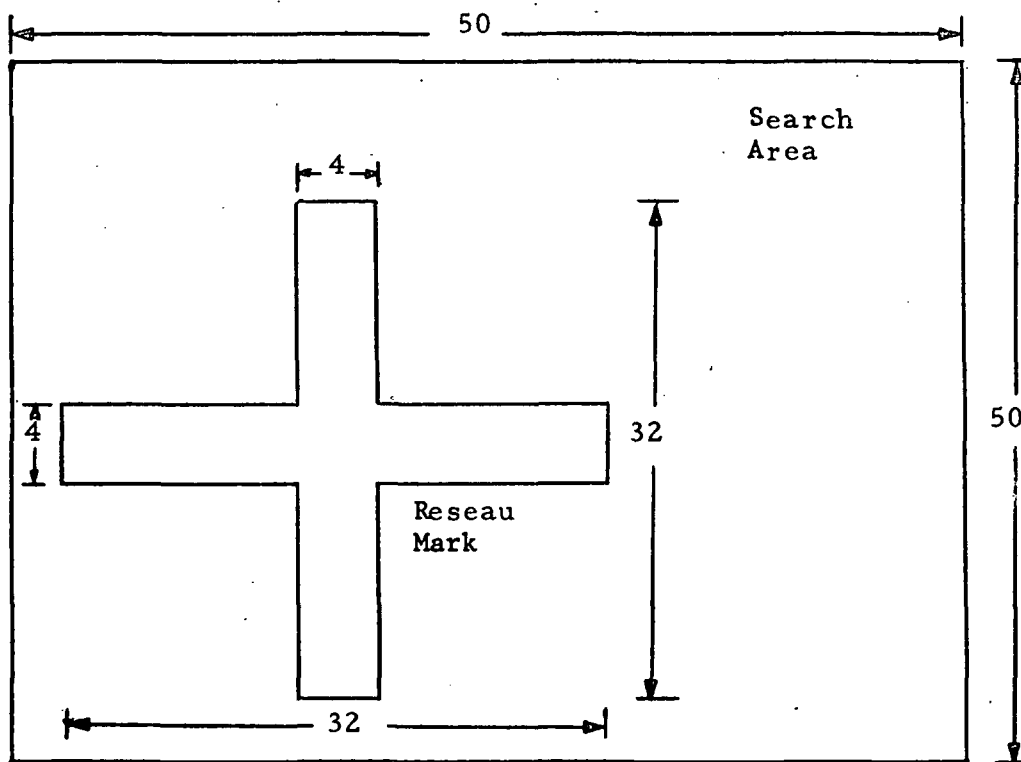


Figure 4-1. Shape and Size of Reseau Within the Search Area

The reseau detection routine developed by IBM is based on the following operational sequence:

- a. The last known locations of reseau marks are inputs to the program.
- b. Within search areas of 50x50 pixels, each centered about a previous reseau mark location, individual row and column sums of pixel gray levels are computed. This operation is called "shadow casting." Thus, along the  $n^{\text{th}}$  column, the sum would be

$$S_n = \sum_{m=1}^{50} g_{mn}$$

where  $g_{mn}$  is the gray level of the pixel located at the  $m^{\text{th}}$  row and the  $n^{\text{th}}$  column of the 50x50 search area.

- c. The reseau mark contained within a search area is detected by the application of the detection algorithm to the row and column sequences  $\left\{ S_m \right\}$  and  $\left\{ S_n \right\}$ .

A detection algorithm was developed, implemented and tested before real RBV data was available.<sup>4,5</sup> It worked well on simulated RBV test images--finding 90 percent of the reseaux correctly. Unfortunately, the reseau marks in real ERTS RBV images are not so well defined as Figure 4-1 would suggest. The RBV beam is distorted slightly by areas of high and low charge density in the image. This causes the reseaux to be fuzzy and to be darker in dark backgrounds than they are in light backgrounds. They vary in width from 3 to 7 pixels, and the arms are often off from horizontal and vertical (giving a greater apparent width in the shadow casting technique).

The original detection algorithm, when applied to real RBV reseaux, proved to be too sensitive to these distortions--only 10 percent of the reseaux were successfully located. However, even though reseaux showed great variance as to size, shape, and intensity, they were invariably the darkest objects in the search area. A new detection algorithm was developed to take advantage of this fact.

This algorithm finds the lowest column sum and tentatively calls this the column center of the reseau. It then computes a threshold value based on the lowest sum and the background intensity. The reseau is considered to be all contiguous sums in the neighborhood of the lowest sum that are lower than the threshold. A similar procedure is used for row sums.

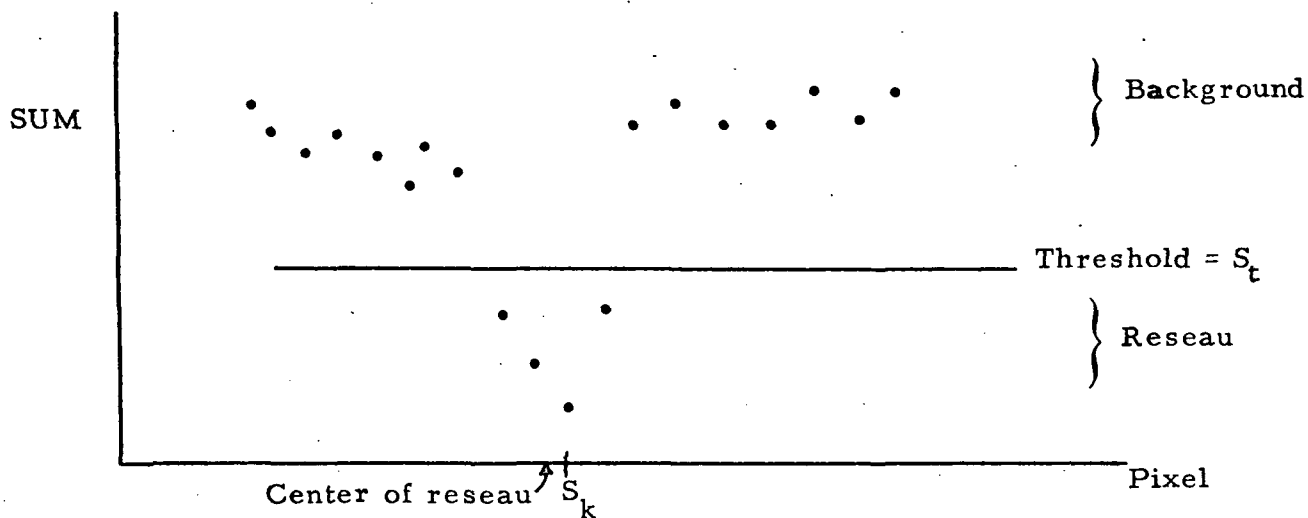


Figure 4-2. Typical Set of Row or Column Sums

The steps of the algorithm, described with reference to the typical set of row or column sums in Figure 4-2, are as follows:

- a. Tentatively call the lowest sum,  $S_k$ , the reseau center.
- b. Next, compute a local average background intensity the following way:
  - Move to the right of  $S_k$  3 sums and the next 4 sums are background.
  - Move to the left of  $S_k$  3 sums and the next 4 sums are background. Average the 8 background sums to get the local average background intensity (call it  $S_a$ ).
- c. Compute the average of  $S_k$  and  $S_a$ . Call this a threshold,  $S_t$ .
 
$$S_t = (S_a + S_k)/2.0$$
- d. All sums below the threshold near  $S_k$  are reseau pixels.

- e. If there is an odd number of pixels in the reseau, the correct center is the middle pixel of the reseau. If there is an even number of pixels in the reseau, the center is the pixel just left of the middle, i.e.



As described, this lowest sum algorithm finds 81 of 81 reseaux. However, it finds a reseau location even if there was no reseau in the search area. Obviously, a check is necessary to detect false reseaux. The false reseau check is based primarily on the following:

- a. Real reseaux are 3 to 7 pixels wide--if we detect a "reseau" narrower than 3 or wider than 7 pixels, reject it.
- b. Real reseaux are much darker than the background, so the algorithm insists that a reseau pixel must be, on the average, at least 8 intensity levels (out of 64) darker than the background. That is,  $S_a - S_k$  must be greater than  $8 \times (32-4) = 244$ .

Both of these checks use data routinely collected during the search for the reseau, and so take very little extra computing time. Used together they are extremely effective.

The reseau detection program was checked on 486 reseau marks (that is, 972 searches, one search through column sums and one search through row sums for each reseau). Every true reseau was found. Visual examination of the reseaux showed the algorithm was finding the correct reseau center. A further confirmation of the algorithm's accuracy is the fact that the algorithm computed the average reseau width to be between 4 and 5 pixels. This agrees well with visual evidence.

The reseau detection program was tested on 486 false reseaux. That is, the program was asked to search for reseaux in 486 search areas that contained no reseaux. Of the 972 searches for the 486 false reseaux, the program accepted only 3 of the 972 as being reseaux. The probability of accepting a false row or column when no reseau is present in the search area is thus approximately 0.003, and the probability of accepting a false reseau is  $(3/972)(3/972) =$  approximately 0.00001. On the average, if the program looked only in search areas that contained no reseaux through more than 1000 images, it would reject all but one of the false reseaux.

## Section 5. LOCATION OF GROUND CONTROL POINTS

The errors and uncertainties present in the available attitude and ephemeris data make it necessary to establish ground truth before precision geometric correction is possible. By determining the image coordinates of well defined geographic features (GCPs) in the scene, the correspondence between image coordinates and geographic coordinates can be used to supplement the attitude and ephemeris data during generation of the output-to-input mapping polynomial.

In a digital image processing system, it is desirable to have ground truth established automatically as part of the processing. The Sequential Similarity Detection Algorithm (SSDA)<sup>4,7,8</sup> has been investigated as a means of accomplishing this. Tests have been run using this program on data from a series of ERTS scenes of the Chesapeake Bay and Phoenix-Tucson areas.

In order to use an SSDA, prototype subimages of the selected geographic features (sometimes called window areas) are required. For the tests conducted by IBM, 20x20 pixel prototype subimages of the features were selected from the earlier of the available MSS scenes. Prototypes of this size (approximately 1.8 km<sup>2</sup> ground area) adequately characterized all features of interest. Search areas containing the geographic features, consisting of 72 lines of 92 samples (approximately 30 km<sup>2</sup> ground area), were taken from subsequent MSS scenes. Each feature was assigned to one of seven classes. Table 5-1 presents the features, class assignments, and ERTS scenes used for the Phoenix-Tucson area, while Table 5-2 provides similar information for the Chesapeake Bay Area.

Preliminary tests were conducted to determine appropriate control parameter values for the SSDA to adapt its operation to ERTS data. From the results of these tests, a suitable error threshold function was obtained. It was also determined that the intensity variation between scenes would require the use of the mean-adjusted error measure to provide a zero order intensity normalization.

The SSDA employs a random sampling sequence for comparing prototype pixels with corresponding search area pixels. Tests were conducted to determine whether more efficient performance could be obtained by selecting a feature-dependent sampling sequence. This was found to be possible, but since no systematic procedure for developing such a sequence could be devised, subsequent investigations employed the random sampling sequence. Typical results of the non-random sampling experiments were presented in Table 5-3.

Initial investigations of the Phoenix-Tucson area employed scenes E-1049-17324 and E-1085-17330. For subsequent work with this area, prototype subimages were selected from these two scenes, and from E-1031-17325, in

Table 5-1

GCPS FROM PHOENIX-TUCSON AREA

Class Code Interpretation

- 1 - Large Land-Water Interfaces
- 2 - Interstate-Grade Highways
- 3 - Airports
- 4 - Small Land-Water Interfaces
- 5 - Non-Interstate-Grade Highways
- 6 - Agricultural Fields
- 7 - Mountain Peaks, Hills

ID	GCP Description	Class Code
1	Bartlett Dam	1
2	T.R. Roosevelt Dam	1
3	Stewart Mtn Dam	1
4	Mormon Flat Dam	1
5	Tailings Pond	1
6	Apache Junction	2
7	Mountain Peak	7
8	Agricultural Field	6
9	Casa Grande Rd Jctn	2
10	Picacho Reservoir	1
11	Redrock Highway	2
14	Hill	7
15	Luke #6 Airfield	3
16	Rittenhouse Airfield	3
17	Florence Jctn	5
18	Stream Confluence	4
19	River Bend	4
20	Small Dam	4
21	Oracle Jctn Store	5
22	Jctn Rts 87 & 93	5
23	Phoenix Hwy Jctn	5
24	Winkleman Jctn	5
25	Owl's Nest Mtn	7
26	Casa Grande Airport	3
27	Gila Bend Airfield	3
28	Luke #2 Airfield	3
29	Luke #1 Airfield	3
30	Ajo Airport	3
31	Mtn at Redrock	7
32	Tailings Pond - Miami	1
33	Hill S. of Black Mtn	7
34	Bend in Gila River	4

Table 5-1 (Continued)

ID	GCP Description	Class Code
35	Bend in Gila River	4
36	Mtn at Pisinmo	7
37	Mtn near Double Peak	7
38	Mtn at Schuck	7
39	Mtn in Papago Reservation	7
40	Mtn in Kovaya Hills	7
41	Guachi Mtn - Ventana	7
42	Lake Pleasant Dam	1
43	Thornydale & Overton Rds	5
44	Guachi Mtn - USGS 2801	7
45	LaCholla & Magee Rds	5

ERTS Scenes Employed: E-1031-17325  
 E-1049-17324  
 E-1085-17330  
 E-1121-17330  
 E-1121-17333  
 E-1211-17334  
 E-1283-17334  
 E-1337-17332

Table 5-2

GCPS FROM CHESAPEAKE BAY AREA

Class Code Interpretation

- 1 - Large Land-Water Interfaces
- 2 - Interstate-Grade Highways
- 3 - Airports (Macadam)
- 4 - Small Land-Water Interface
- 5 - Airports (Concrete)

ID	GCP Description	Class Code
1	Center - Liberty Dam	1
2	Elk Neck	1
3	Mouth of Monocacy	1
4	Lake Needwood	1
5	Cabin John Bridge	4
6	Kent Point	1
7	Mouth - Tuckahoe Crk	1
8	Hains Point	1
9	Hallowing Point	1
10	Prison Point	1
11	Fishing Point	1
12	Lake Louisa	1
13	North Tip, Goat Island	1
14	South End, Downing Br	1
15	Glebe Point	1
16	Sandy Point	1
17	Point Lookout	1
18	Rapidan & Rappahannock	1
19	Rappahannock Bend	1
20	Dulles Airport	5
21	I695 and I95(N)	2
22	I695 and I83(N)	2
23	I695 and I83(S)	2
24	I695 and I70N	2
25	I95 and I495(N)	2
26	I495 and B-W Pkwy	2
27	I495 and Rt 50	2
28	I495 and Rt 4	2
29	Rt 301 and Rt 4	2
30	East End, Wilson Br	1
31	West End, 14th St Br	1
32	East End, 14th St Br	1

Table 5-2 (Continued)

ID	GCP Description	Class Code
33	East End Memorial Br	1
34	East End Roosevelt Br	1
35	I70N and Rt 29	2
36	I70N and Rt 40	2
37	I66 and Rt 50	2
38	I66 and Rt 29(N)	2
39	I66 and Rt 29(S)	2
40	I495 and I66	2
41	I695 and B-W Pkwy	2
42	Nat'l Airport	3
43	Loch Raven Dam	1

ERTS Scenes Employed: E-1062-15190  
 E-1080-15192  
 E-1170-15193  
 E-1350-15192  
 E-1440-15175

Table 5-3

EFFECT OF NON-RANDOM SAMPLING STRATEGIES

GCP Type/Band	Sampling					
	Type 1 Time	Type 1 Success	Type 2 Time	Type 2 Success	Type 3 Time	Type 3 Success
Large Land-Water Interfaces/ Band 4	7.2 sec	yes	6.4 sec	yes	4.8 sec	no
Large Land-Water Interfaces/ Band 7	6.7	yes	7.2	yes	4.7	yes
Hills/Band 6	7.8	yes	4.9	yes	3.7	yes
Small Land-Water Interfaces/ Band 5	8.9	yes	10.5	yes	4.9	yes
Interstate-Grade Highways/ Band 6	3.6	yes	4.4	no	5.6	yes
Hills/Band 5	24.3	yes	5.9	yes	3.7	yes

Type 1 sampling - random  
 Type 2 sampling - selected samples outline feature  
 Type 3 sampling - selected samples cover feature and exclude context

order to obtain prototypes free of striping. For the Chesapeake Bay area, all prototype subimages were taken from scene E-1062-15190. The results of the SSDA tests are summarized in Tables 5-4 through 5-7. Table 5-4 presents the results obtained for ground features in the Phoenix-Tucson area, and Table 5-5 presents these results in terms of the success ratio (number of features of a given type found divided by the number sought) for the various feature types and search area-prototype temporal separations. Inspection of Table 5-5 reveals high success in bands 5 and 7 for land-water interfaces, mountain peaks, and hills, and in band 7 for airfields. Attempts to locate precisely the boundaries of agricultural fields were frustrated by the change which occurred in these features over time.

Tables 5-6 and 5-7 present the corresponding results for the Chesapeake Bay area. The predominant features employed in this area were land-water interfaces and interstate-grade highways. SSDA performance on land-water interfaces was more successful in bands 6 and 7, and on interstate-grade highways was more successful in band 5.

By employing an appropriate combination of feature type and spectral band, one can obtain successful registrations in a minimal time. For example, for the data presented here, a selection based on the spectral band feature type combinations which exhibit the highest success ratios is presented in Table 5-8.

Under IRAD funding, an experiment was conducted to see whether revision of the SSDA threshold function could improve performance. The results, summarized in Table 5-9, showed that altering the threshold function could significantly decrease location times. However, no single function good for all features in a given spectral band was determined. Investigation of this area is continuing.

## SSDA RESULTS - MSS DATA, PHOENIX-TUCSON AREA

Target Type	Band 4			Band 5			Band 6			Band 7		
	No. Found/ Tried	Average Time (Sec.)										
	No. Found/ Tried		No. Found/ Tried		No. Found/ Tried		No. Found/ Tried		No. Found/ Tried		No. Found/ Tried	
Large Land-Water Interfaces	4/6	4.2	6/6	3.1	5/6	2.5	5/6	6.9	5/6	6.9	5/6	6.9
Non-Interstate-Grade Highways	2/8	4.8	6/8	12.2	6/8	37.3	6/8	20.2	6/8	20.2	6/8	20.2
Airports	0/2	---	0/2	---	1/2	48.0	1/2	6.8	1/2	6.8	1/2	6.8
Small Land-Water Interfaces	2/3	11.8	3/3	11.6	3/3	49.1	3/3	6.3	3/3	6.3	3/3	6.3
Hills	1/2	5.5	2/2	6.2	1/2	4.6	2/2	51.6	2/2	51.6	2/2	51.6
Fields	1/1	4.2	1/1	2.7	0/1	---	0/1	---	0/1	---	0/1	---
Large Land-Water Interfaces	1/2	4.8	2/2	3.6	2/2	2.9	2/2	5.7	2/2	5.7	2/2	5.7
Large Land-Water Interfaces	2/4	2.9	1/4	2.4	2/4	2.1	2/4	7.3	4/4	7.3	4/4	7.3
Non-Interstate-Grade Highways	4/8	38.9	4/8	6.8	2/8	3.0	4/8	59.9	4/8	59.9	4/8	59.9
Airports	2/2	48.6	2/2	7.5	1/2	6.1	2/2	71.2	2/2	71.2	2/2	71.2
Small Land-Water Interfaces	2/2	63.9	2/2	8.0	1/2	3.4	2/2	61.5	2/2	61.5	2/2	61.5
Hills	2/2	51.7	2/2	15.8	0/2	---	2/2	62.6	2/2	62.6	2/2	62.6
Fields	0/1	---	0/1	---	0/1	---	0/1	---	0/1	---	0/1	---
Large Land-Water Interfaces	3/4	5.189	4/4	2.719	2/4	2.084	4/4	5.425	4/4	5.425	4/4	5.425
Non-Interstate-Grade Highways	3/5	10.791	3/5	4.465	0/5	---	2/5	53.726	2/5	53.726	2/5	53.726
Airports	0/2	---	0/2	---	0/2	---	2/2	61.298	2/2	61.298	2/2	61.298
Small Land-Water Interfaces	1/2	62.796	1/2	8.867	0/2	---	1/2	58.854	1/2	58.854	1/2	58.854
Hills	2/2	49.950	2/2	14.948	1/2	7.840	2/2	59.367	2/2	59.367	2/2	59.367
Fields	0/1	---	0/1	---	0/1	---	0/1	---	0/1	---	0/1	---
Large Land-Water Interfaces	0/0	---	0/0	---	4/7	1.91	0/0	---	0/0	---	0/0	---
Interstate-Grade Highways	0/0	---	0/0	---	2/3	3.65	0/0	---	0/0	---	0/0	---
Airports	0/0	---	0/0	---	2/5	8.25	0/0	---	0/0	---	0/0	---
Small Land-Water Interfaces	0/0	---	0/0	---	0/0	---	0/0	---	0/0	---	0/0	---
Non-Interstate-Grade Highways	0/0	---	0/0	---	1/2	3.85	0/0	---	0/0	---	0/0	---
Mountain Peaks, Hills	0/0	---	0/0	---	3/3	12.66	0/0	---	0/0	---	0/0	---
Large Land-Water Interfaces	0/0	---	2/3	2.24	0/0	---	2/3	1.80	2/3	1.80	2/3	1.80

Table 5-4 (Continued)

Target Type	Band 4			Band 5			Band 6			Band 7		
	No. Found/ Tried	Average Time (Sec.)										
	No. Found/ Tried	Average Time (Sec.)										
Large Land-Water Interfaces	5/5	2.65	5/5	2.66	0/1	---	4/5	2.19	252 days			
Interstate-Grade Highways	2/3	2.66	2/3	2.33	1/3	1.71	0/3	---				
Airports	1/5	1.09	2/5	1.90	3/3	11.99	5/5	11.61				
Small Land-Water Interfaces	1/1	5.41	1/1	5.30	2/2	22.99	1/1	6.12				
Non-Interstate-Grade Highways	1/2	2.31	1/2	2.61	1/2	3.57	1/2	2.01				
Mountain Peaks, Hills	3/3	6.18	3/3	6.16	4/5	12.84	3/3	14.59				
Large Land-Water Interfaces	0/1	---	0/1	---	0/0	---	3/3	0.87	306 days			
Interstate-Grade Highways	2/3	3.80	1/3	0.99	0/0	---	1/9	1.59				
Airports	3/4	36.28	4/4	4.66	0/0	---	9/12	5.62				
Small Land-Water Interfaces	2/2	53.42	2/2	5.37	0/0	---	4/6	8.73				
Non-Interstate-Grade Highways	1/2	4.73	1/2	2.29	0/0	---	2/6	0.78				
Mountain Peaks, Hills	6/7	36.61	7/7	6.10	0/0	---	17/22	9.25				

Table 5-5

REGISTRATION SUCCESS RATIOS AS A FUNCTION OF THE TEMPORAL SEPARATION  
BETWEEN SEARCH AREA AND WINDOW AREA

Phoenix-Tucson Area

Temporal Separation (Days)	Band 4	Band 5	Band 6	Band 7
<b>Large Land-Water Interfaces</b>				
18	--	1.00	--	1.00
36	0.67	1.00	0.83	0.86
54	--	1.00	--	1.00
72	0.50	1.00	1.00	1.00
90	0.50	0.25	0.50	1.00
180	0.75	1.00	0.50	1.00
198	--	--	0.43	--
234	--	0.67	--	0.67
252	1.00	1.00	0.00	0.80
306	0.00	0.00	--	1.00
<b>Interstate-Grade Highways</b>				
18	--	--	--	--
36	--	--	--	--
54	--	--	--	--
72	--	--	--	--
90	--	--	--	--
180	--	--	--	--
198	--	--	0.67	--
234	--	--	--	--
252	0.67	0.67	0.33	0.00
306	0.67	0.33	--	0.33

Note: -- indicates no data

Table 5-5 (Continued)

Temporal Separation (Days)	Band 4	Band 5	Band 6	Band 7
<b>Airports</b>				
18	--	0.50	--	1.00
36	0.00	0.00	0.50	0.50
54	--	1.00	--	1.00
72	--	--	--	--
90	1.00	1.00	0.50	1.00
180	0.00	0.00	0.00	1.00
198	--	--	1.00	--
234	--	--	--	--
252	0.20	0.40	1.00	1.00
306	0.75	1.00	--	1.00
<b>Small Land-Water Interfaces</b>				
18	--	0.00	--	0.00
36	0.67	1.00	1.00	1.00
54	--	0.00	--	1.00
72	--	--	--	--
90	1.00	1.00	0.50	1.00
180	0.50	0.50	0.00	0.50
198	--	--	--	--
234	--	--	--	--
252	1.00	1.00	1.00	1.00
306	1.00	1.00	--	1.00
<b>Non-Interstate-Grade Highways</b>				
18	--	--	--	--
36	0.25	0.75	0.75	0.75
54	--	--	--	--
72	--	--	--	--
90	0.50	0.50	0.25	0.50
180	0.60	0.60	0.00	0.40
198	--	--	0.50	--
234	--	--	--	--
252	0.50	0.50	0.50	0.50
306	0.50	0.50	--	0.50

Note: -- indicates no data

Table 5-5 (Continued)

Agricultural Fields

Temporal Separation (Days)	Band 4	Band 5	Band 6	Band 7
18	--	--	--	--
36	1.00	1.00	0.00	0.00
54	--	--	--	--
72	--	--	--	--
90	0.00	0.00	0.00	0.00
180	0.00	0.00	0.00	0.00
198	--	--	--	--
234	--	--	--	--
252	--	--	0.00	--
306	0.00	0.00	--	0.00

Mountain Peaks, Hills

18	--	1.00	--	1.00
36	0.50	1.00	0.50	1.00
54	--	1.00	--	1.00
72	--	--	--	--
90	1.00	1.00	0.00	1.00
180	1.00	1.00	0.50	1.00
198	--	--	1.00	--
234	--	--	--	--
252	1.00	1.00	0.80	1.00
306	0.86	1.00	--	0.86

Note: -- indicates no data

Table 5-6

## SSDA RESULTS - MSS DATA, CHESAPEAKE BAY AREA

Target Type	Band 4			Band 5			Band 6			Band 7			
	No. Found/ No. Tried	Average Time (Sec.)											
												Temporal Separation	
Large Land-Water Interfaces	6/15	6.62	5/15	10.98	14/15	0.93	15/15	0.67	15/15	0.67	15/15	0.67	18 days
Interstate-Grade Highways	16/16	1.78	16/16	2.52	15/16	6.90	15/16	2.92	15/16	6.90	15/16	2.92	
Airports (Macadam)	0/1	---	0/1	---	1/1	0.81	1/1	0.64	1/1	0.81	1/1	0.64	
Small Land-Water Interfaces	5/7	3.51	4/7	5.56	7/7	1.57	7/7	0.82	7/7	1.57	7/7	0.82	
Airports (Concrete)	1/1	1.29	1/1	2.71	1/1	4.82	1/1	1.62	1/1	4.82	1/1	1.62	
Large Land-Water Interfaces	5/14	7.08	5/14	8.65	8/14	0.76	8/14	0.71	8/14	0.76	8/14	0.71	108 days*
Interstate-Grade Highways	16/16	2.38	16/16	2.77	10/16	4.60	6/16	7.15	10/16	4.60	6/16	7.15	
Airports (Macadam)	1/1	2.40	1/1	5.66	1/1	0.82	1/1	0.81	1/1	0.82	1/1	0.81	
Small Land-Water Interfaces	6/7	2.08	5/7	3.35	5/7	0.99	3/7	0.93	5/7	0.99	3/7	0.93	
Airports (Concrete)	0/1	---	1/1	3.17	1/1	5.87	0/1	---	1/1	5.87	0/1	---	
Large Land-Water Interfaces	11/14	5.50	9/14	5.54	14/14	0.79	13/14	0.66	14/14	0.79	13/14	0.66	288 days
Interstate-Grade Highways	14/16	1.84	16/16	1.70	10/16	4.00	7/16	2.60	10/16	4.00	7/16	2.60	
Airports (Macadam)	1/1	2.38	1/1	2.88	1/1	0.75	1/1	0.68	1/1	0.75	1/1	0.68	
Small Land-Water Interfaces	4/6	3.91	4/6	4.32	2/6	1.37	2/6	0.76	2/6	1.37	2/6	0.76	
Airports (Concrete)	0/1	---	1/1	2.59	0/1	---	0/1	---	0/1	---	0/1	---	
Large Land-Water Interfaces	9/14	3.62	10/14	6.67	14/14	0.89	14/14	0.67	14/14	0.89	14/14	0.67	378 days
Interstate-Grade Highways	14/16	1.79	14/16	2.44	12/16	4.08	14/16	1.95	12/16	4.08	14/16	1.95	
Airports (Macadam)	1/1	2.24	1/1	3.83	1/1	0.80	1/1	0.69	1/1	0.80	1/1	0.69	
Small Land-Water Interfaces	6/7	5.11	5/7	5.35	6/7	1.44	5/7	0.80	6/7	1.44	5/7	0.80	
Airports (Concrete)	1/1	1.46	1/1	3.13	1/1	3.36	1/1	1.12	1/1	3.36	1/1	1.12	

\*For the 108 day data, portions of the image were under snow cover

Table 5-7

REGISTRATION SUCCESS RATIOS AS A FUNCTION OF THE TEMPORAL SEPARATION  
BETWEEN SEARCH AREA AND WINDOW AREA

## Chesapeake Bay Area

Temporal Separation (Days)	Band 4	Band 5	Band 6	Band 7
<b>Large Land-Water Interfaces</b>				
18	0.40	0.33	0.93	1.00
108	0.36	0.36	0.57	0.57
288	0.79	0.64	1.00	0.93
378	0.64	0.71	1.00	1.00
<b>Interstate-Grade Highways</b>				
18	1.00	1.00	0.94	0.94
108	1.00	1.00	0.63	0.38
288	0.88	1.00	0.63	0.44
378	0.88	0.88	0.75	0.88
<b>Airports (Macadam)</b>				
18	0.00	0.00	1.00	1.00
108	1.00	1.00	1.00	1.00
288	1.00	1.00	1.00	1.00
378	1.00	1.00	1.00	1.00
<b>Small Land-Water Interfaces</b>				
18	0.71	0.57	1.00	1.00
108	0.86	0.71	0.71	0.43
288	0.67	0.67	0.33	0.33
378	0.86	0.71	0.86	0.71
<b>Airports (Concrete)</b>				
18	1.00	1.00	1.00	1.00
108	0.00	1.00	1.00	0.00
288	0.00	1.00	0.00	0.00
378	1.00	1.00	1.00	1.00

Table 5-8

## AVERAGE SSSA PERFORMANCE FOR SELECTED FEATURE-BAND COMBINATIONS

Type/Band	Average Registration Time	Average Success Ratio
Large Land-Water Interfaces/Band 7	2.08 sec	0.88
Mountain Peaks, Hills/Band 5	8.44	1.00
Airports/Band 7	15.44	0.81
Interstate-Grade Highways/Band 5	2.33	0.93

Table 5-9. Effect of Revised Threshold

MSS BAND 7

GCP ID	Description	Scene 1337-17332 (Original Threshold)		Scene 1283-17334 (Revised Threshold)	
		Time (secs)	Success	Time (secs)	Success
42	Lake Pleasant Dam	5.43	No	2.42	Yes
28	Luke # 2 airfield	69.74	Yes	6.28	Yes
29	Luke # 1 airfield	69.88	Yes	7.48	Yes
32	Tailings Pond	5.72	Yes	2.81	Yes
34	Bend in Gila River	68.16	Yes	5.54	Yes
27	Gila Bend airfield	65.13	Yes	5.01	Yes
37	Mountain near Double Peak	57.36	Yes	4.93	Yes
31	Mountain at Redrock	60.50	Yes	29.86	Yes
41	Guachi Mountain	29.73	Yes	3.84	Yes

MSS BAND 4

GCP ID	Description	Scene 1337-17332 (Original Threshold)		Scene 1283-17334 (Revised Threshold)	
		Time (secs)	Success	Time (secs)	Time
6	Apache Junction	28.44	No	4.64	No
23	Phoenix highway junction	9.46	Yes	4.63	Yes
17	Florence Junction	58.27	No	13.33	No
15	Luke # 6 airfield	39.43	No	4.53	No
16	Rittenhouse airfield	49.95	Yes	5.08	No
19	River bend	55.42	Yes	5.41	Yes
10	Picacho Reservoir	2.20	No	1.67	No
9	Casa Grande road junction	5.34	Yes	3.74	Yes
7	Mountain peak	29.80	Yes	6.11	Yes
27	Gila Bend airfield	48.38	Yes	5.44	Yes
11	Redrock highway	6.07	Yes	4.24	Yes
14	Hill	62.23	Yes	7.55	Yes

## Section 6. COMPARISON OF RESAMPLING TECHNIQUES

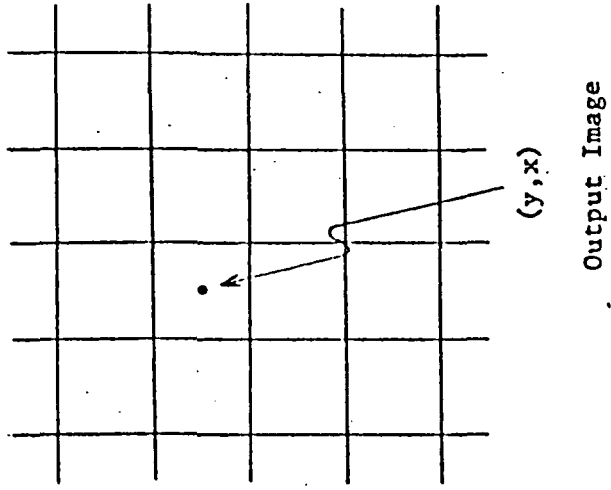
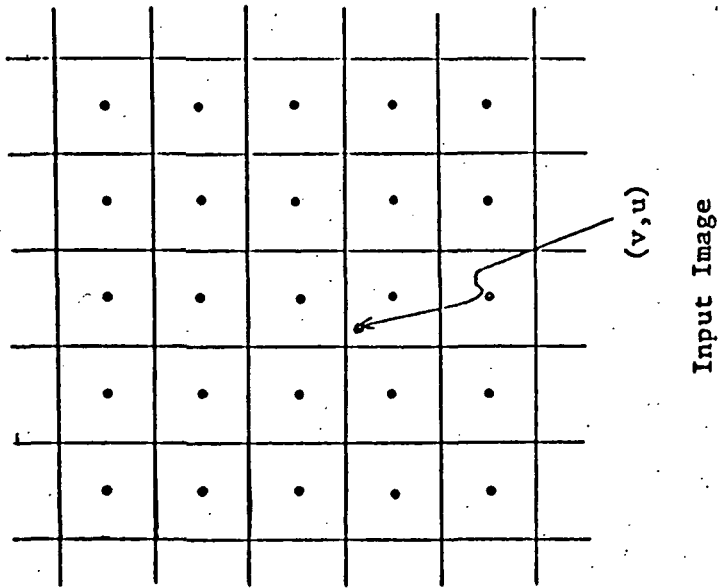
At present three different resampling techniques are being proposed for application to ERTS data: nearest neighbor assignment, bilinear interpolation, and cubic convolution. This section describes the three techniques and presents the results of a resampling experiment conducted under this contract as well as some related investigations outside the scope of the contract, conducted under IRAD funding.

### 6.1 NEAREST NEIGHBOR ASSIGNMENT

Of the three resampling techniques considered, nearest neighbor assignment is the simplest and fastest to perform on a general-purpose digital computer. Consider Figure 6-1. The pixels in the input and output images are rectangles whose centers have integer-valued coordinates. The point  $(y,x)$  in the output image ( $y$  and  $x$  are integers) is mapped to the point  $(v,u)$  in the input image ( $v$  and  $u$  are rational numbers). The output image pixel at coordinates  $(y,x)$  is assigned the intensity value of the input image pixel whose center is nearest to the coordinates  $(v,u)$ . That is, the intensity value of the rectangular input image pixel containing the point  $(v,u)$  is used as the intensity value of the output image pixel  $(y,x)$ .

If the horizontal scales of the input image and output image are not too different, there will be one-to-one correspondence between line segments of pixels in the input and output images. This is illustrated in Figure 6-2. Points 1, 2, and 3 in the output image are mapped to consecutive points A, B, and C in the input image. These values need not be inserted into the output image individually. Since they are consecutive in the input image and in the output image, all three may be inserted at once using the MVC instruction. Similarly, values of points C, D, and E may be moved at once to points 4, 5, and 6. Then point F must be moved by itself to point 7. Next, points F, G, H, and I are moved at once to points 8, 9, 10, and 11. This process continues until the entire output image array has been constructed. This is the basis of IBM's "Point Shift" algorithm.

Moving several values at once is much more efficient than moving them individually. In fact, efficiency increases as the move length increases (see Table 6-1). Hence, another way to reduce computer processing time is to maintain the original horizontal scales of the input and output images.



Assign the intensity of the input pixel nearest to the point  $(v,u)$  to the output pixel  $(y,x)$ .

Figure 6-1. Nearest Neighbor Assignment



Table 6-1

## POINT SHIFT PERFORMANCE

<u>ERTS Image</u>	<u>Horizontal Scale Change</u>	<u>Usual Move Length</u>	<u>CPU Time*</u>
RBV	4608 to 3648	3-4	300 sec
MSS	3240 to 3648	8-9	160 sec

\*On an IBM 370/155 computer

IBM has chosen its output image scale in order to obtain 1:1 000 000 scale with a pixel size of 50  $\mu\text{m}$  x 50  $\mu\text{m}$ . This is a reasonably efficient scale for MSS images, but is less so for RBV due to the much larger number of input samples.

The major drawback to nearest neighbor assignment is the discontinuities which are introduced by its zero-order interpolation. These produce a "staircase" effect on slanting linear features with a particular orientation, which is visible upon close examination of the corrected images. For users to whom this effect is objectionable, nearest neighbor assignment is an unacceptable resampling technique.

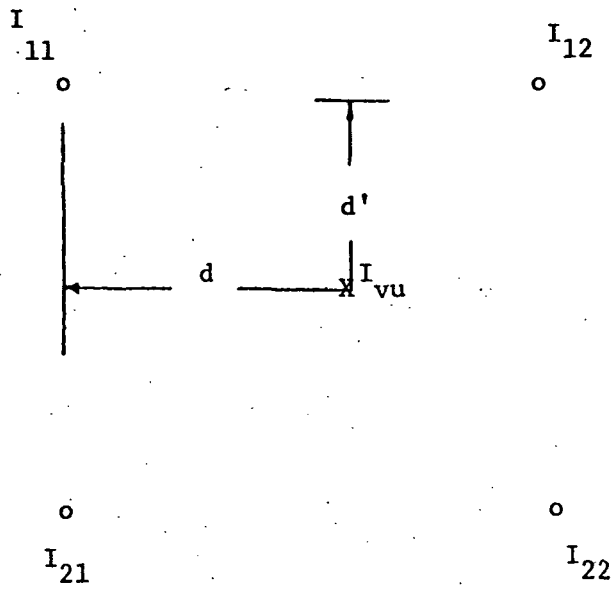
## 6.2 BILINEAR INTERPOLATION

The bilinear interpolation algorithm is given in Figure 6-3. Four input image pixel intensity values are used to compute the intensity value of each output image pixel:

$$I_{vu} = I_{11} + d (I_{12} - I_{11}) + d' \left[ I_{21} + d (I_{22} - I_{21}) - I_{11} - d (I_{12} - I_{11}) \right] \quad (1)$$

Various computer algorithms to implement bilinear interpolation are possible. For experimental purposes, IBM has written a bilinear interpolation program which uses single precision floating point arithmetic to evaluate formula (1). Although inefficient from a computer standpoint, this method was chosen to minimize the programming complexity and maintain high accuracy.

Since bilinear interpolation requires at least six adds and three multiplies per output point, it is computationally more expensive to apply in a general-purpose computer than nearest neighbor assignment. Bilinear



o - Input Image Samples

X - Output Image Sample Mapped Into Input Image Space

$$I_{vu} = I_{11} + d (I_{12} - I_{11}) + d' [I_{21} + d (I_{22} - I_{21}) - I_{11} - d (I_{12} - I_{11})]$$

Figure 6-3. Bilinear Interpolation

interpolation smooths out the high spatial frequencies in the data and eliminates the discontinuities present in data resampled with nearest neighbor assignment. There is evidence that bilinear interpolation may filter the data to such an extent that multispectral classification may be degraded.

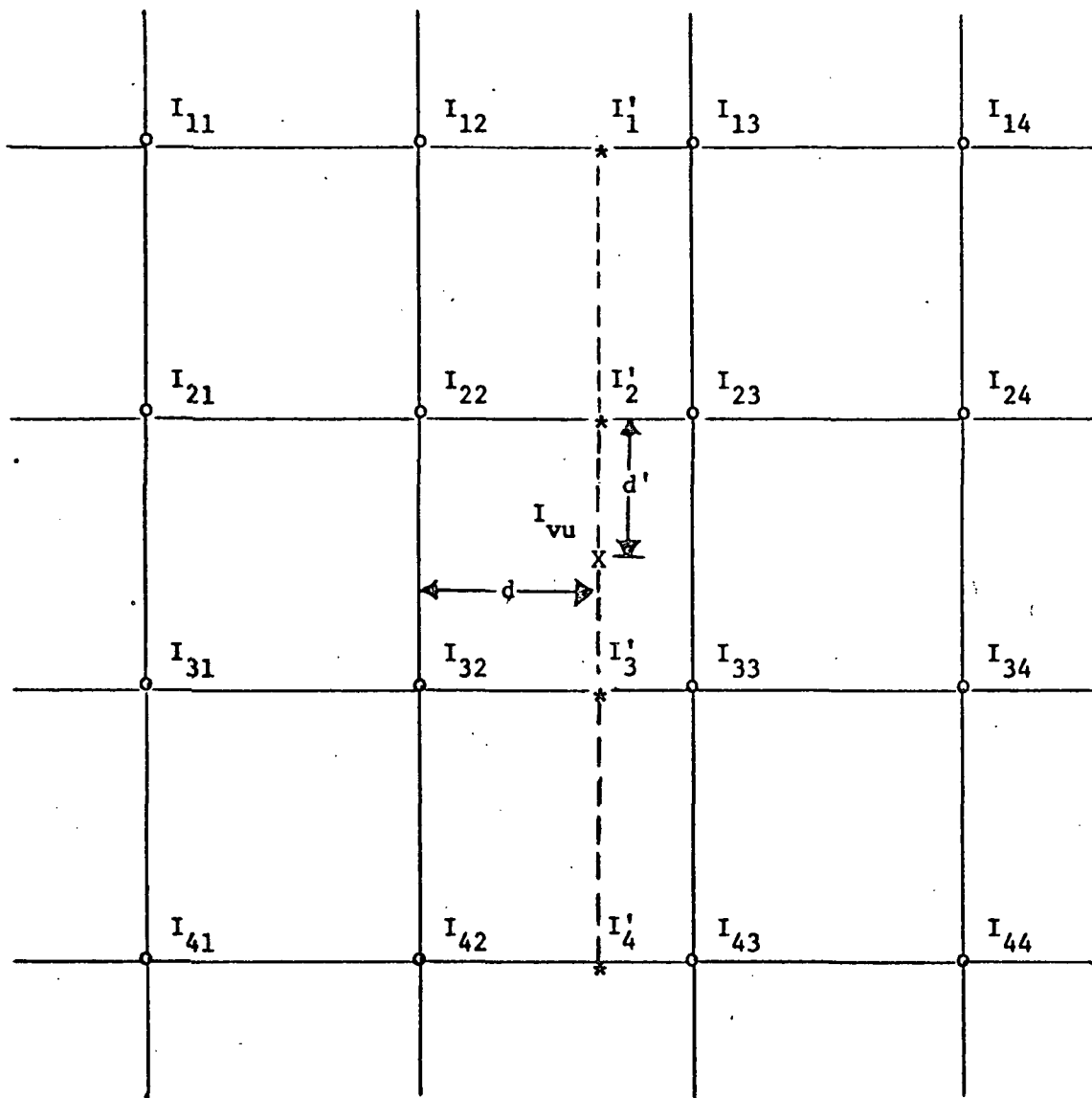
### 6.3 CUBIC CONVOLUTION

The cubic convolution algorithm is illustrated in Figure 6-4. Sixteen input image pixel intensity values are used to compute the intensity value of each output pixel. The algorithm uses four input points in the following way:

$$\begin{aligned}
 I'_k &= I_{k1} \left[ 4 - 8(1+d) + 5(1+d)^2 - (1+d)^3 \right] \\
 &\quad + I_{k2} (1 - 2d^2 + d^3) \\
 &\quad + I_{k3} \left[ 1 - 2(1-d)^2 + (1-d)^3 \right] \\
 &\quad + I_{k4} \left[ 4 - 8(2-d) + 5(2-d)^2 - (2-d)^3 \right] \tag{2}
 \end{aligned}$$

$$\begin{aligned}
 &= d \left\{ d \left[ d(I_{k4} - I_{k3} + I_{k2} - I_{k1}) \right. \right. \\
 &\quad \left. \left. + (-I_{k4} + I_{k3} - 2I_{k2} + 2I_{k1}) \right] \right. \\
 &\quad \left. + (I_{k3} - I_{k1}) \right\} \tag{3} \\
 &\quad + I_{k2}
 \end{aligned}$$

Formula (3) is evaluated for each row of four points. The four input image intensity values  $I_{k1}$ ,  $I_{k2}$ ,  $I_{k3}$ ,  $I_{k4}$  and horizontal distance  $d$  are used to obtain an intermediate interpolated intensity value  $I'_k$ . Then these four intermediate interpolated values  $I'_1$ ,  $I'_2$ ,  $I'_3$ ,  $I'_4$  and the vertical distance  $d'$  are used in formula (3) to obtain the final intensity value  $I_{vu}$ . Various computer algorithms to implement cubic convolution interpolation are possible. IBM has written an experimental cubic convolution program which uses single precision floating point arithmetic to evaluate formula (3). Although very inefficient from a computer standpoint, this method was chosen to minimize the programming complexity and maintain high accuracy.



o - Input Image Samples

\* - Horizontal Interpolation Points

X - Output Image Sample Mapped Into Input Image Space

$$I'_k = d \left\{ d[d(I_{k4} - I_{k3} + I_{k2} - I_{k1}) + (I_{k3} - I_{k4} - 2I_{k2} + 2I_{k1})] + (I_{k3} - I_{k1}) \right\} + I_{k2}$$

$$I'_{vu} = d' \left\{ d'[d'(I'_4 - I'_3 + I'_2 - I'_1) + (I'_3 - I'_4 - 2I'_2 + 2I'_1)] + (I'_3 - I'_1) \right\} + I'_2$$

Figure 6-4. Cubic Convolution

Cubic convolution (developed by TRW)<sup>9</sup> is a good approximation to six x/x interpolation, which is theoretically perfect for band-limited signals. Thus, cubic convolution provides a high-quality resampling technique. Its major disadvantage is its application cost. Since cubic convolution requires at least 15 multiplies and 55 adds per output point, it is relatively expensive to implement on a general-purpose computer. On a special-purpose processor, however, cubic convolution is feasible, even for high-throughput systems.

#### 6.4 RESAMPLING EXPERIMENT

In order to produce a means by which the outputs of the three resampling techniques could be compared, band 5 of scene 1002-18134 was processed with all three techniques. The nearest neighbor assignment output was already presented as Figure 3-9. The bilinear interpolation and cubic convolution results are presented in Figures 6-5 and 6-6 respectively.

Figure 6-7 shows an enlarged area from each of the three processed images. The image resampled by nearest neighbor assignment shows the expected staircase discontinuities. The bilinear interpolation image does not have these discontinuities but appears less sharp. The cubic convolution image shows neither the discontinuities of nearest neighbor assignment nor the blurriness of bilinear interpolation.

In all three parts of Figure 6-7, the six-line discontinuities due to sampling delay errors are visible. This is due to the fact that the programs contained no compensation for that effect. Sampling delay compensation has been conducted under IRAD activity (see Section 6.5.2).

The production times on an IBM 370/155 for the three images were 160 seconds for nearest neighbor assignment, 2160 seconds for bilinear interpolation, and 4980 seconds for cubic convolution. These times are not really meaningful, however, since (as mentioned previously) the bilinear interpolation and cubic convolution programs were not efficiently coded. It is estimated that efficient coding could reduce those production times by 30 percent.

#### 6.5 RELATED IRAD INVESTIGATIONS

IBM has conducted two investigations related to resampling under its IRAD program. The results of these investigations are described below.

Figures 6-5 through 6-7 are contained in the envelope at the back of this report.

### 6.5.1 Resampling Error Measurement

The three methods of image interpolation were compared by generating histograms of the pixel differences between an image obtained by interpolating pixel values and an image obtained by sampling at the appropriate position.

To accomplish this, a set of eight digital images (four of urban areas, four of natural features) whose samples represented 3 meter square spots were processed to simulate the images which would be obtained using an 80 meter square spot, with 1.4 samples/IFOV along the scan direction, and 1.0 samples/IFOV transverse to the scan direction. The three interpolation methods were then applied to the simulated images, generating images composed of samples interpolated to halfway between the lines and samples of the simulated images.

The original images were then processed again, this time to produce simulated images whose sample locations corresponded to those of the interpolated samples. Histograms of the differences of corresponding images were then made. Typical examples of these histograms are presented in Figures 6-8 and 6-9.

The histograms provide an indication of the relative intensity error to be expected when these three interpolation techniques are employed to resample digital imagery. They also provide a caution against the convenient assumption that interpolated samples accurately reproduce the samples which would be obtained on another sampling lattice. While the sampling theorem specifies the conditions (i.e., a band limited signal spectrum) which would permit an exact resampling, in practice one is dealing with signals which either do not satisfy that condition, or which have been distorted (i.e., filtered) to satisfy it. In the former case, resampling can in principle be only approximate. In the latter case, one can exactly reproduce an approximation of the original analog signal.

The histograms show that, as a resampling technique (i.e., a method of estimating samples on a lattice other than the one on which available data samples exist), cubic convolution is more accurate than bilinear interpolation, which in turn is more accurate than nearest neighbor assignment. However, even with cubic convolution, resampling errors may be on the order of 10 counts, and a one count error is more likely than no error at all.

### 6.5.2 Additional Distortion Correction

At present, the ERTS NDPF applies no correction for sampling delay errors. This practice has drawn criticism from portions of the user community.

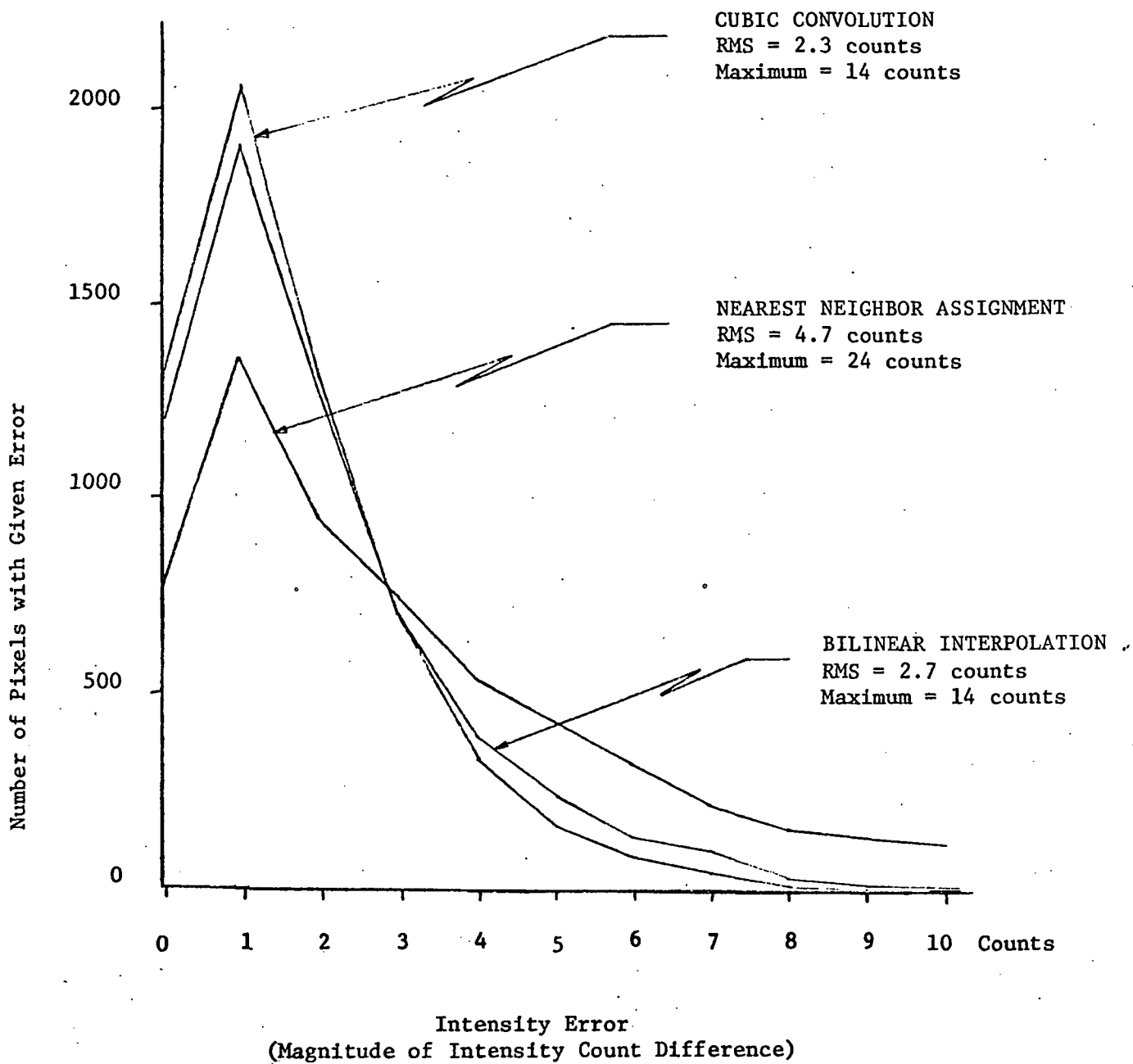


Figure 6-8. Resampling Error Histograms-Cultural Image

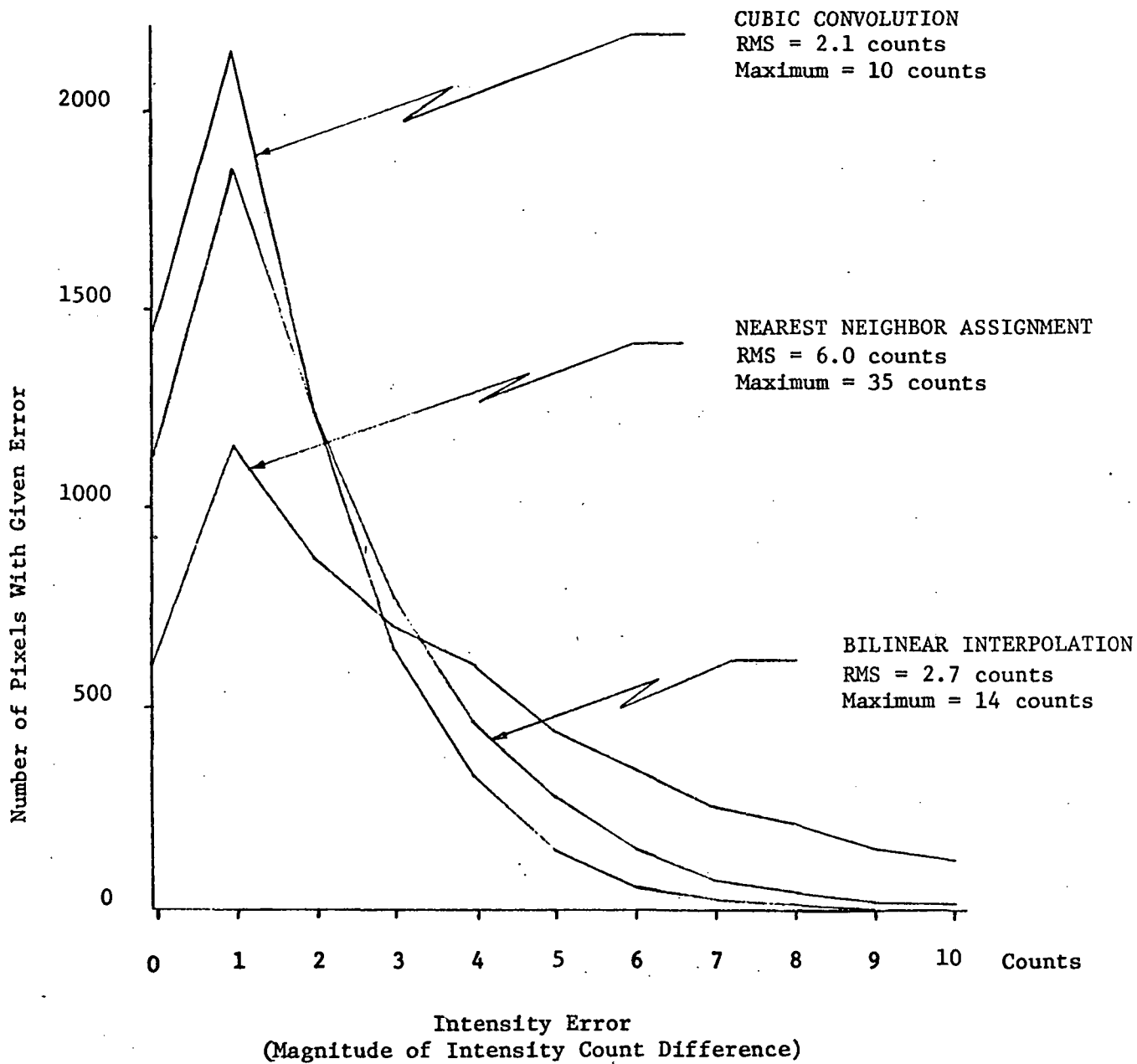


Figure 6-9. Resampling Error Histograms-Natural Image

IBM has developed experimental versions of programs which combine the compensations for all geometric distortions (including sampling delay errors) into a single, composite geometric correction. In these programs, all the geometric distortions for which compensation is provided are corrected in a single resampling. Programs have been written around the bilinear interpolation and cubic convolution resampling techniques discussed above. (A nearest neighbor assignment program incorporating sampling delay error compensation was not implemented, since the sampling delay offsets would only be shifted by nearest neighbor assignment.)

Band 5 of scene 1002-18134 was corrected with each of the correction programs, with the results shown in Figures 6-10 and 6-11. Enlargements of a subimage area are given in Figure 6-12. The sampling delay discontinuities have been removed. Otherwise, the comments made with regard to Figure 6-7 apply to Figure 6-12 also.

Production times on a 370/155 were 2880 seconds for bilinear interpolation and 6900 seconds for cubic convolution, reflecting the fact that neither of these programs was coded efficiently. Efficient coding might reduce these times by 30 percent.

Figures 6-10 through 6-12 are contained in the envelope at the back of this report.

## Section 7. CONFIGURATION ANALYSIS

This section describes five hardware configurations for operational ERTS data correction systems. The configurations are analyzed in terms of their components, operations, throughput, system cost, and cost per scene. It should be noted that the figures presented herein are estimates to be used for planning purposes only and do not represent any offer or commitment on the part of IBM.

### 7.1 CONFIGURATION AND PROCESSING DESCRIPTIONS

The processing steps assumed and the configurations developed to perform them are defined below.

#### 7.1.1 Processing Definition

For each configuration considered, a processing day of 16 hours at 75 percent efficiency (12 hours of actual processing) was assumed. Each configuration was assumed to perform the following processing steps:

##### Step 1:

- Input imagery is read from magnetic tape and transformed to a pixel interleaved (by band) format.
- Supporting data (e.g., ephemeris) is read.
- The image data is radiometrically corrected by table look-up.
- GCP and reseau search areas (as required) are extracted from the input stream and stored for subsequent detection operations.

##### Step 2:

- GCPs are located in the image data.
- Reseau (for RBV images only) are located in the image data.
- Required geometric correction functions are generated.

These processes are not overlapped with I/O operations.

Step 3:

- Geometric correction is applied, using nearest neighbor assignment as the resampling technique.
- The corrected, annotated data is written to magnetic tape in pixel interleaved format.

Step 4:

- User requested scenes are selected from the master output tape and copied onto 800/1600 BPI tape.

Figure 7-1 is a set of graphs of the CPU time required to perform the first three processing steps on various machines. The fourth step is constant for all configurations since it is almost totally dependent on the I/O time required to write the 800 or 1600 BPI tapes.

#### 7.1.2 Configuration Definitions

The five configurations considered are defined in Table 7-1. For the highest-throughput configuration (configuration E) a variation including direct output to a laser beam recorder (LBR) was also evaluated.

#### 7.2 MAN-MACHINE INTERACTION

All configurations analyzed include an operator station with gray scale displays and keyboards. Cloud cover and quality assessment will be a manual operation, wherein an operator will view a scene and key into the information management system his assessments.

A more significant manual operation concerns ground control points (GCPs). It is possible for a man to identify ground control points using a gray scale display by employing an interactive "zooming" procedure wherein he identifies a candidate position on the screen and is presented with an expanded view of the area. After several expansions he will be viewing a sufficiently detailed area to identify a particular scene. Given a reference notebook containing properly scaled ground control point areas he will be able to compare the screen with the reference material to identify the GCP. This method is feasible in a low throughput system processing MSS scenes only. Assuming 12 GCPs are required per MSS scene and that 2 or 3 expansions will be used for a GCP, a completely manual GCP detection operation would require approximately 15 minutes per MSS scene which would extend even the lowest throughput system analyzed by more than 10 minutes per scene. RBV scenes pose a still greater problem since GCPs would be required for each RBV band.

Table 7-1

## CONFIGURATION DEFINITIONS

Configuration	Input Tape Type	Reformatting and Radiometric Correction Processor	Geometric Correction Processor	Geometric Correction Function	Output Tape Type
A	800 BPI CCT	One General-Purpose Processor (GPP)		Individual Scene	6250 BPI CCT
B	HDDT	One GPP		Individual Scene	6250 BPI CCT
C	HDDT	One Microprogrammed Special-Purpose Processor (SPP)	One GPP	Individual Scene	6250 BPI CCT
D	HDDT	One SPP	One GPP	Entire pass for MSS, individual scene for RBV	HDDT
E*	HDDT	One SPP	One SPP supported by one GPP	Entire pass for MSS, individual scene for RBV	HDDT

\* A version of this configuration including direct output to a laser beam recorder was also considered.



A more acceptable arrangement would be to use the Sequential Similarity Detection Algorithm (SSDA), an automatic digital GCP detection technique, augmented with a manual backup. The same "zooming" technique as described above could be used as back-up upon notification by the system that sufficient GCPs could not be found automatically. The cost in time for this operation will vary widely due to the many factors which affect the efficiency of automatic GCP detection.

A third arrangement is to rely still more heavily on the automatic technique by providing for the searching for an excess number of GCPs and presenting results to the screen for verification by the operator. In this approach, as results are computed, a split screen is presented with 1) the original area displayed intact and 2) the original area with the library GCP area inserted at the computed position. The advantages of this approach are:

- Timely response, since only a rejection needs to be communicated to the system (acceptance is the default)
- Accuracy, since experimentation has shown that registration failures are typically gross rather than narrowly off the mark, so that manual detection of erroneous registration is likely
- Simplified implementation, since much less new software is implied in this approach than a more manually oriented one.

For these reasons, this third approach is the one assumed in the following analysis.

The effects of another choice for GCP detection on the following analysis can be extrapolated, so that no need exists for extensive investigations into the effect on each configuration considered below. In general, a more manually oriented GCP approach will have a more significant impact on higher throughput systems, since the manual operations are constant among configurations.

### 7.3 HARDWARE CONFIGURATION ANALYSIS

The five configurations studied are discussed in the following sections.

#### 7.3.1 Configuration A

The components of this configuration are pictured in Figure 7-2. During Step 1, image data is read from 800 BPI CCT one scene at a time into a general purpose processor. Radiometric correction and reformatting are

accomplished, and the image data is temporarily stored on disk. GCP and reseau search areas are held in main memory only as long as they are needed for Step 2 processing. When Step 2 processing is complete, the data is read from the disk; geometric correction is applied; and the fully corrected data is output on 6250 BPI CCT.

The performance and cost of this configuration, using five different General-Purpose Processors (GPPs) are shown in Figure 7-3 and Table 7-2.

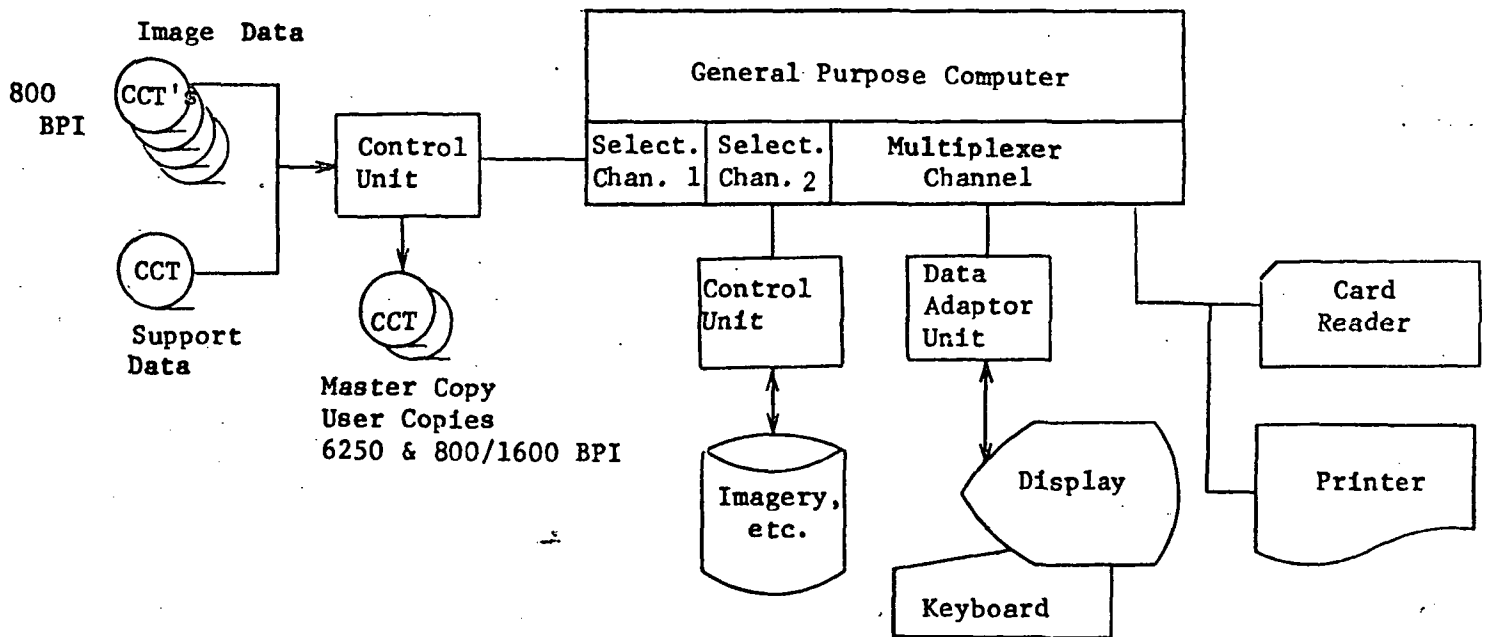
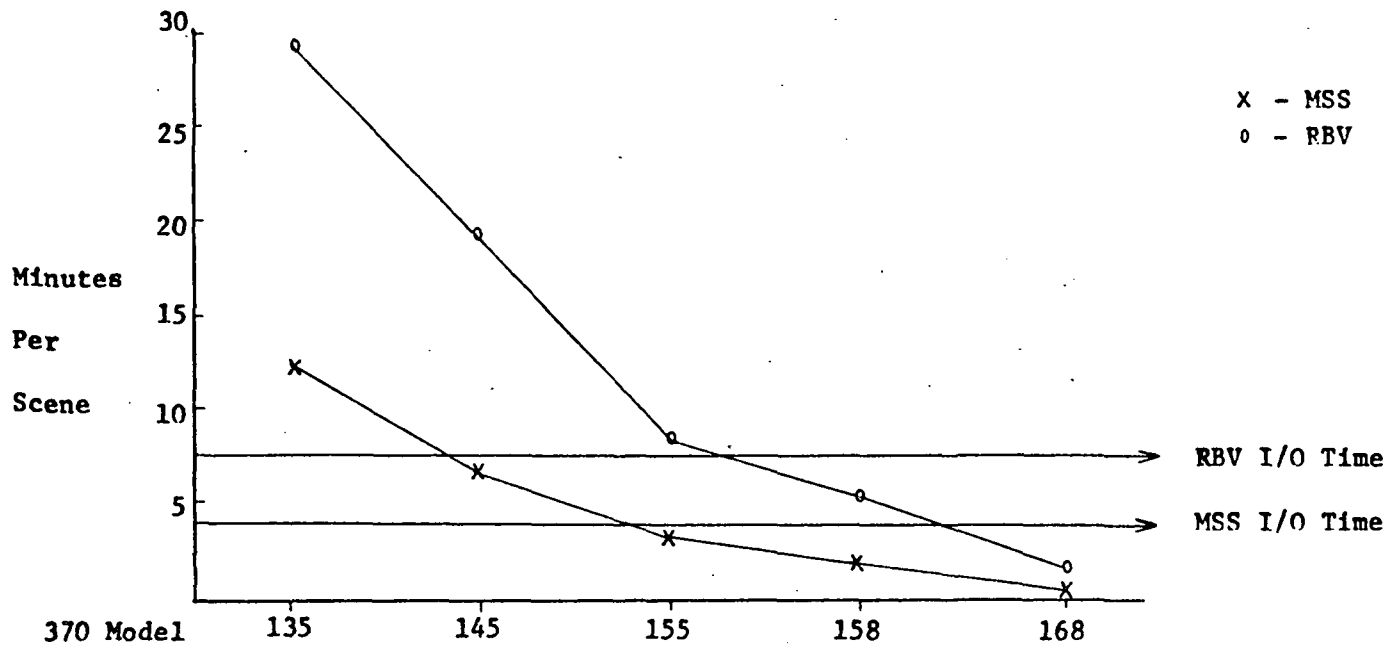
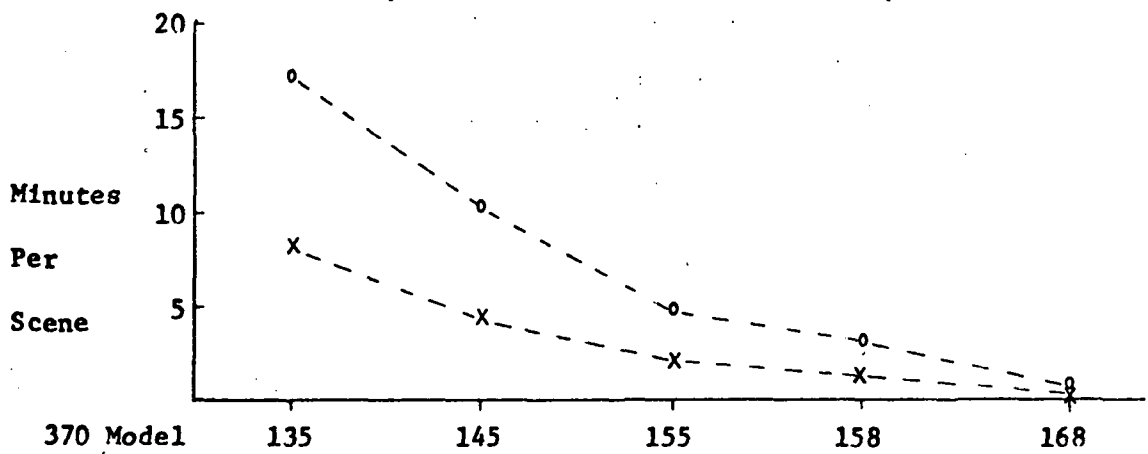


Figure 7-2. Configuration A Diagram

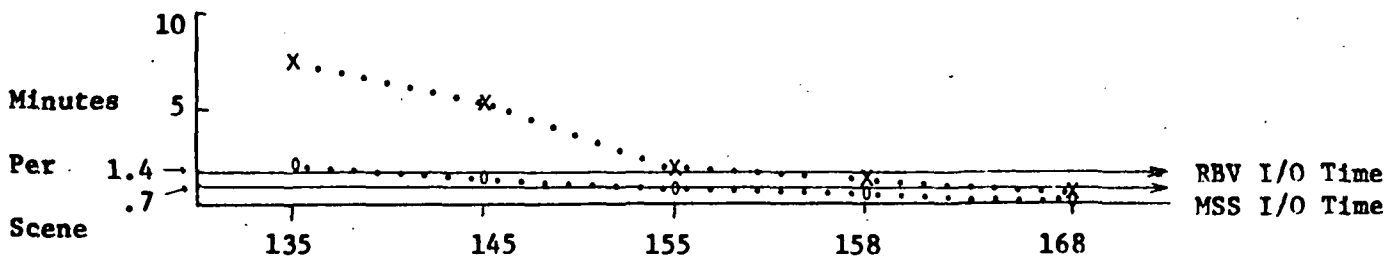
Figure 7-3 shows that Step 1 processing is a bottleneck. With the lower models, CPU processing severely restricts throughput. Even with the most powerful processor, very large throughput is precluded by the I/O time required to read 800 BPI tapes.



(a) Step 1 Processing



(b) Step 2 Processing



(c) Step 3 Processing

Figure 7-3. Configuration A Processing Times

Table 7-2

CONFIGURATION A SUMMARY

370 MODEL		135		145		155		158		168	
		MSS	RBV	MSS	RBV	MSS	RBV	MSS	RBV	MSS	RBV
TIME PER SCENE IN MINUTES	SENSOR										
	STEP 1	12.5	29.4	6.7	19.2	4.0 <sup>I</sup>	8.4	4.0 <sup>I</sup>	7.5 <sup>I</sup>	4.0 <sup>I</sup>	7.5 <sup>I</sup>
	STEP 2	8.1	17.2	4.5	10.4	2.3	4.9	1.5	3.3	.4	.8
	STEP 3	7.5	2.0	5.3	1.4 <sup>I</sup>	2.0	1.4 <sup>I</sup>	1.2	1.4 <sup>I</sup>	.7	1.4 <sup>I</sup>
TOTAL	28.1	48.6	16.5	31.0	8.3	14.7	6.7	12.2	5.1	9.7	
COMBINED TOTAL		76.7		47.5		23.0		18.9		14.8	
THROUGHPUT	INDIVIDUALLY	25	14	43	23	86	48	107	59	141	74
SCENES/DAY	COMBINED	9		15		31		38		48	
APPROXIMATE	MILLIONS OF \$	.80		1.40		1.70		2.10		4.10	
COST	PER SCENE <sup>A</sup>	17.75	31.75	18.00	33.75	11.00	19.75	11.00	19.75	16.25	30.75

A - COST PER SCENE IS AMORTIZED OVER A 5 YEAR PERIOD

I - I/O BOUND OPERATION

### 7.3.2 Configuration B

Configuration B, shown in Figure 7-4, overcomes the input bottleneck of configuration A by using HDDT as the input medium. Otherwise, operation and equipment are the same as in configuration A.

From Table 7-3 and the graphs of Figure 7-5, it can be seen that although throughput is greatly improved in the high range of processors (158 and 168) with a corresponding reduction in scene cost, the lower range of computer is not improved since these were compute bound in Step 1 processing.

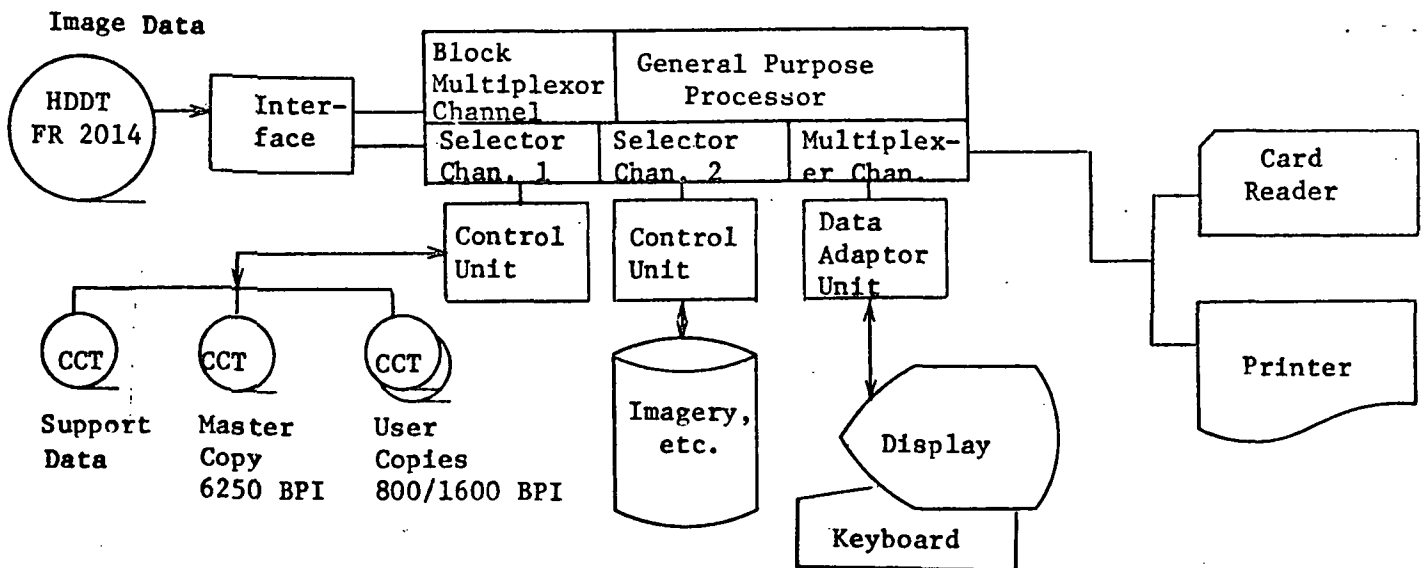
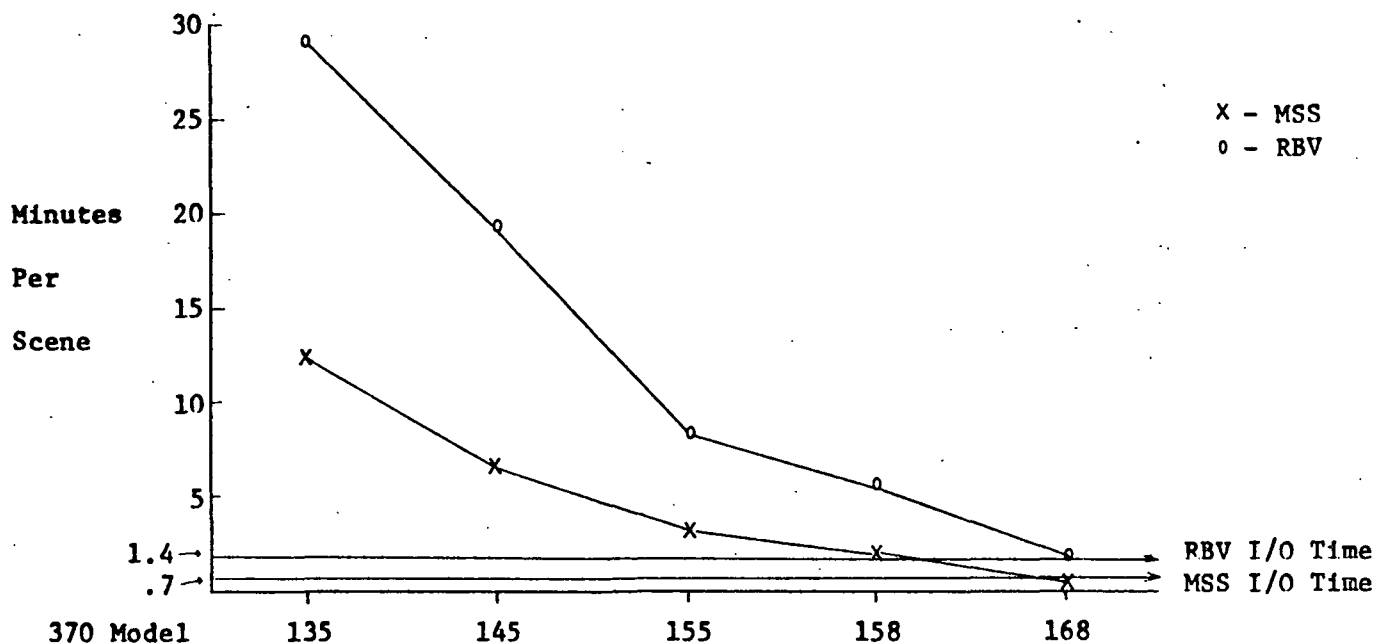


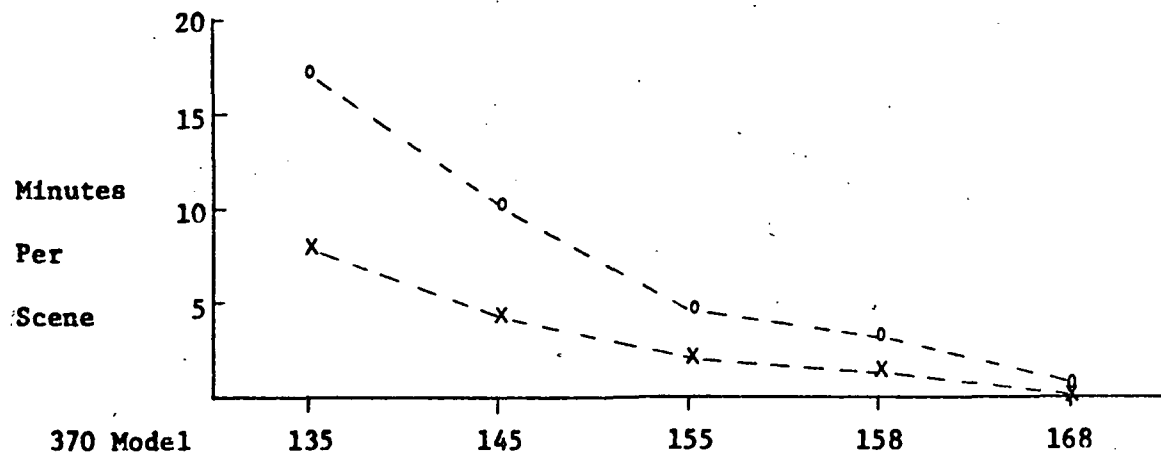
Figure 7-4. Configuration B Diagram

### 7.3.3 Configuration C

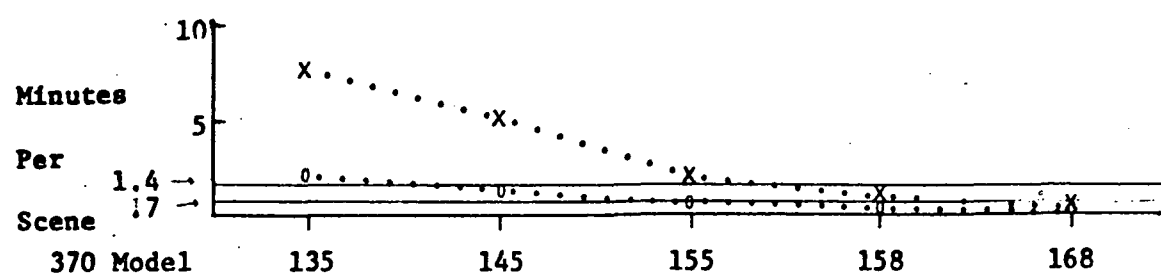
Improved Step 1 performance is achieved in configuration C, shown in Figure 7-6. Image data is read from HDDT one scene at a time and is reformatted and radiometrically corrected in a microprogrammed Special-Purpose Processor (SPP). From this point on, processing is the same as in the previous configurations.



(a) Step 1 Processing



(b) Step 2 Processing



(c) Step 3 Processing

Figure 7-5. Configuration B Processing Times

## CONFIGURATION B SUMMARY

370 MODEL		135		145		155		158		168	
		MSS	RBV	MSS	RBV	MSS	RBV	MSS	RBV	MSS	RBV
SENSOR											
TIME PER	STEP 1	12.5	29.4	6.7	19.2	3.3	8.4	2.0	5.6	.7 <sup>I</sup>	1.8
SCENE IN	STEP 2	8.1	17.2	4.5	10.4	2.3	4.9	1.5	3.3	.4	.8
MINUTES	STEP 3	7.5	2.0	5.3	1.4 <sup>I</sup>	2.0	1.4 <sup>I</sup>	1.2	1.4	.7 <sup>I</sup>	1.4 <sup>I</sup>
	TOTAL	28.1	48.6	16.5	31.0	7.6	14.7	4.7	10.3	1.8	4.0
	COMBINED TOTAL	76.7		47.5		22.3		15.0		5.8	
THROUGHPUT	INDIVIDUALLY	25	14	43	23	94	48	153	69	400	180
SCENES/DAY	COMBINED	9		15		32		48		124	
APPROXIMATE	MILLIONS OF \$	.88		1.48		1.78		2.18		4.18	
COST	PER SCENE <sup>A</sup>	19.50	35.00	19.00	35.75	10.50	20.50	8.00	17.50	5.75	13.00

A - COST PER SCENE IS AMORTIZED OVER A 5 YEAR PERIOD

I - I/O BOUND OPERATION

The performance and cost estimates for this configuration are presented in Figure 7-7 and Table 7-4. Step 1 processing is now constrained by the I/O rate (estimated to be  $7 \times 10^5$  bytes/sec.) that can be maintained to disk, where the image data is stored prior to Step 3 processing. Step 2 processing is also a major constraining factor for this configuration.

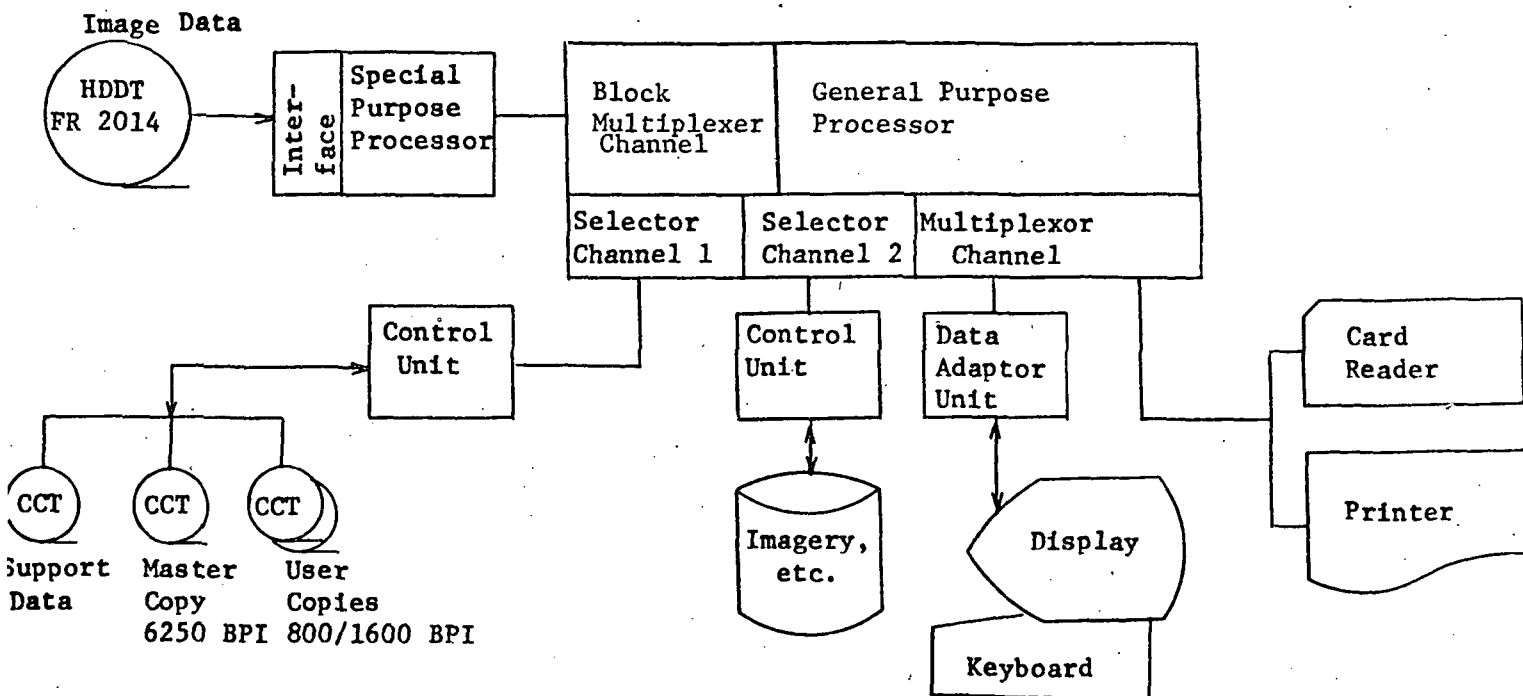
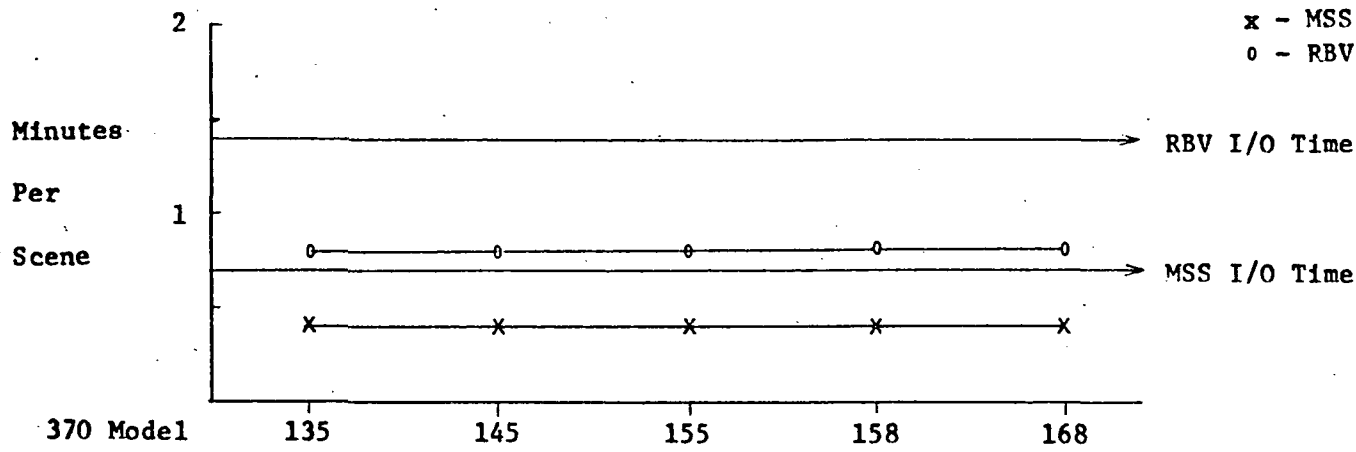


Figure 7-6. Configuration C Diagram

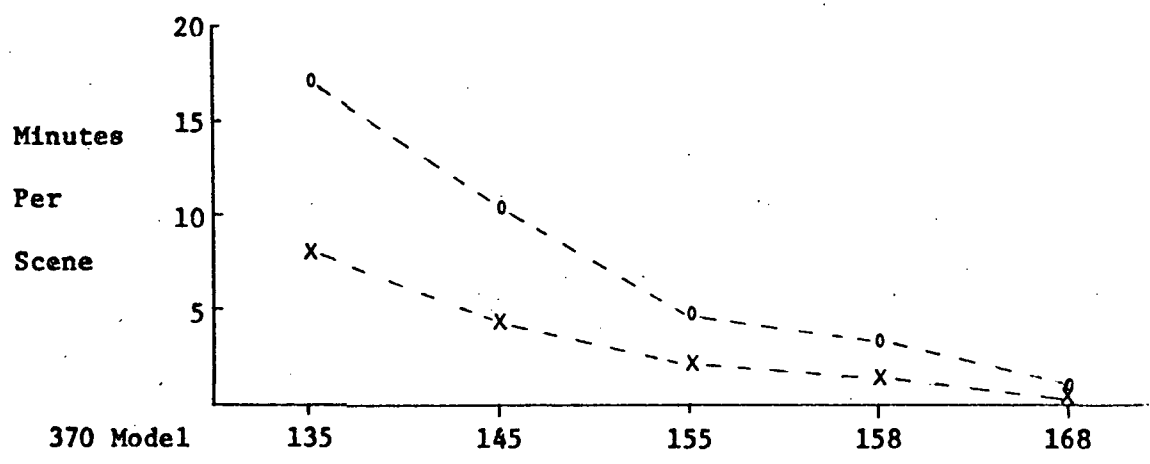
#### 7.3.4 Configuration D

Configuration D, shown in Figure 7-8, overcomes the disk I/O rate constraint by writing the radiometrically corrected data on HDDT. An entire orbital pass of data is processed through Step 1 and recorded on HDDT. GCP and reseau search areas are extracted and stored on disk while the image data is passing through the GPP.

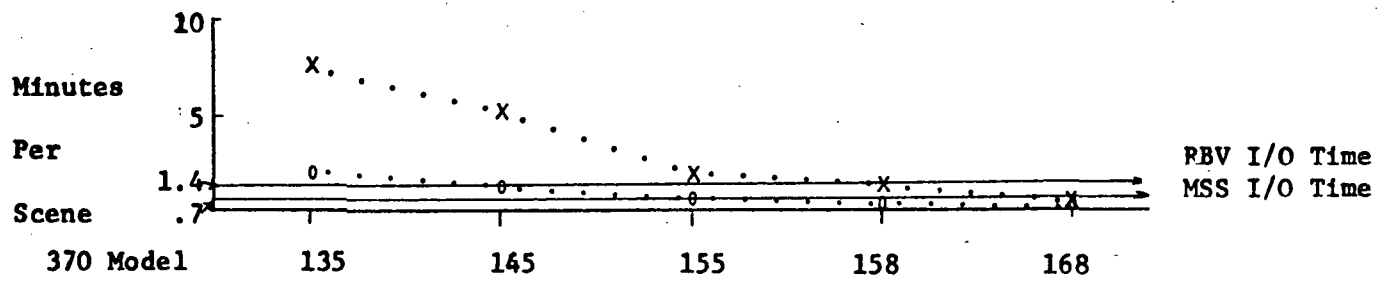
A geometric correction function is computed for the entire MSS pass (rather for each individual scene), thereby reducing the Step 2 processing load. This is possible, since the MSS scans a continuous swath of data. Since RBV scenes are discrete entities, they must be corrected individually.



(a) Step 1 Processing



(b) Step 2 Processing



(c) Step 3 Processing

Figure 7-7. Configuration C Processing Times

TABLE 7-4  
CONFIGURATION C SUMMARY

370 MODEL		135		145		155		158		168	
TIME PER SCENE IN MINUTES	SENSOR	MSS	RBV	MSS	RBV	MSS	RBV	MSS	RBV	MSS	RBV
		STEP 1	.7 I	1.4 I	.7 I						
STEP 2		8.1	17.2	4.5	10.4	2.3	4.9	1.5	3.3	.4	.8
STEP 3		7.5	2.0	5.3	1.4 I	2.0	1.4 I	1.2	1.4 I	.7 I	1.4 I
TOTAL		16.3	20.6	10.5	13.2	5.0	7.7	3.4	6.1	1.8	3.6
COMBINED TOTAL		36.9		23.7		12.7		9.5		5.4	
THROUGHPUT		44	34	68	54	144	93	211	118	400	200
SCENES/DAY		19		30		56		75		133	
APPROXIMATE		1.20		1.80		2.10		2.50		4.50	
COST	A	15.00	19.50	14.75	15.50	8.00	12.50	6.50	11.75	6.25	12.50

A - COST PER SCENE IS AMORTIZED OVER A 5 YEAR PERIOD  
I - I/O BOUND OPERATION

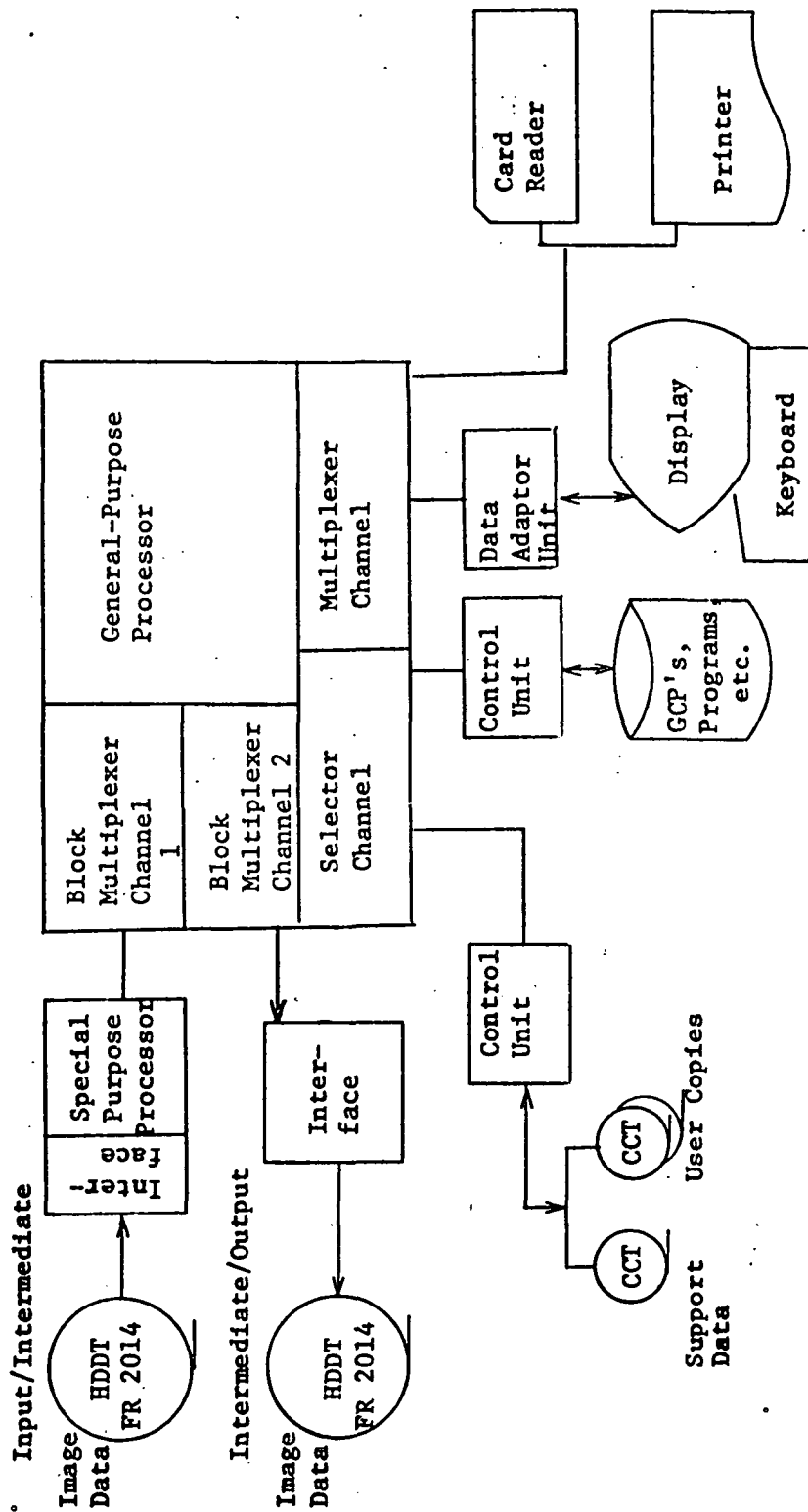


Figure 7-8. Configuration D Diagram

For Step 3, the entire pass of data is read from HDDT, geometrically corrected in the GPP, and written onto HDDT.

As Figure 7-9 and Table 7-5 show, system performance is greatly improved in this configuration. Step 1 is now limited by the channel rate rather than the disk rate. Step 2 processing for MSS scenes is reduced; and Step 3 I/O time is reduced, since it, too, is limited by the channel rate rather than the disk rate.

### 7.3.5 Configuration E

The final configuration considered (shown in Figure 7-10) uses a second SPP to perform the extensive byte manipulation required for geometric correction.

The GPP is used only for GCP and reseau detection and for correction function computation. With this arrangement, Steps 1 and 2 are being processed for one pass of data while Step 3 processing is done for a previously preprocessed pass.

The performance and cost estimates for this configuration are shown in Figure 7-11 and Tables 7-6 and 7-7.

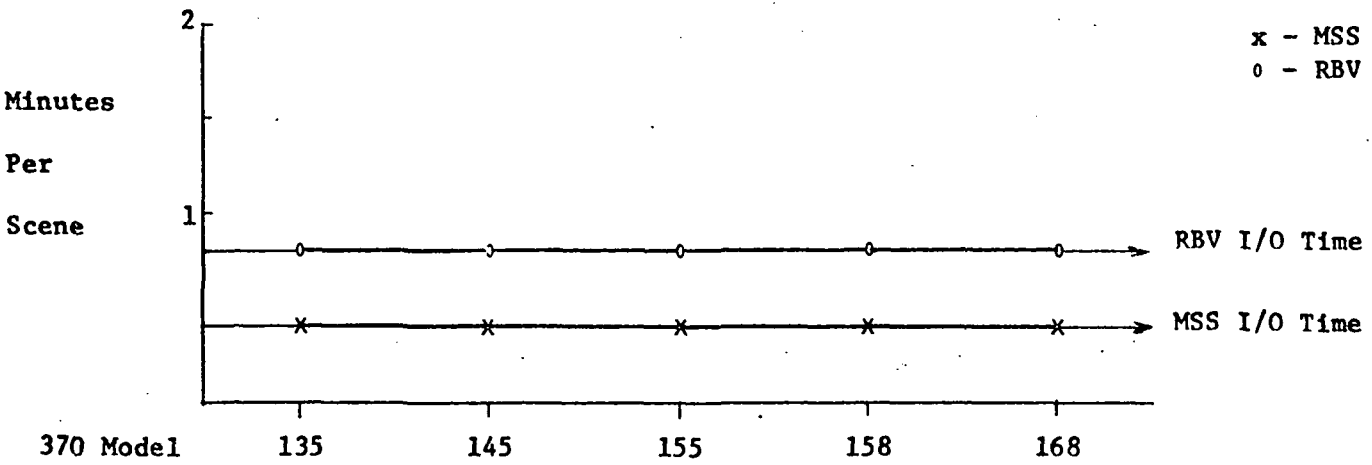
Table 7-6 shows cost data without considering the LBR, to permit easier comparison with earlier configurations. Table 7-7 shows system and scene costs, including the LBR.

The per scene cost for RBV scenes is slightly increased with this configuration. However, the greatly decreased per scene cost for MSS more than balances the difference. The combined cost for one MSS and one RBV scene is less in this configuration than in earlier ones.

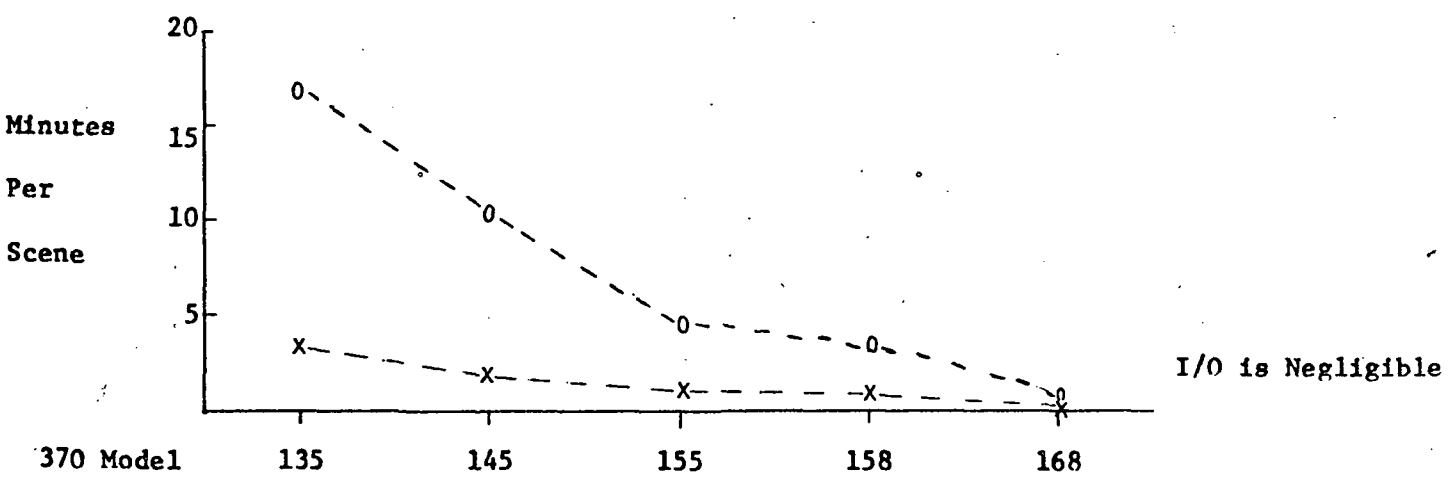
### 7.3.6 Configuration Summary

This section presents a summary of the results for all configurations. Tables 7-8, 7-9, and 7-10 present in order scene throughputs, configuration costs, and scene cost. Two sets of figures are given for configuration E, as stated earlier.

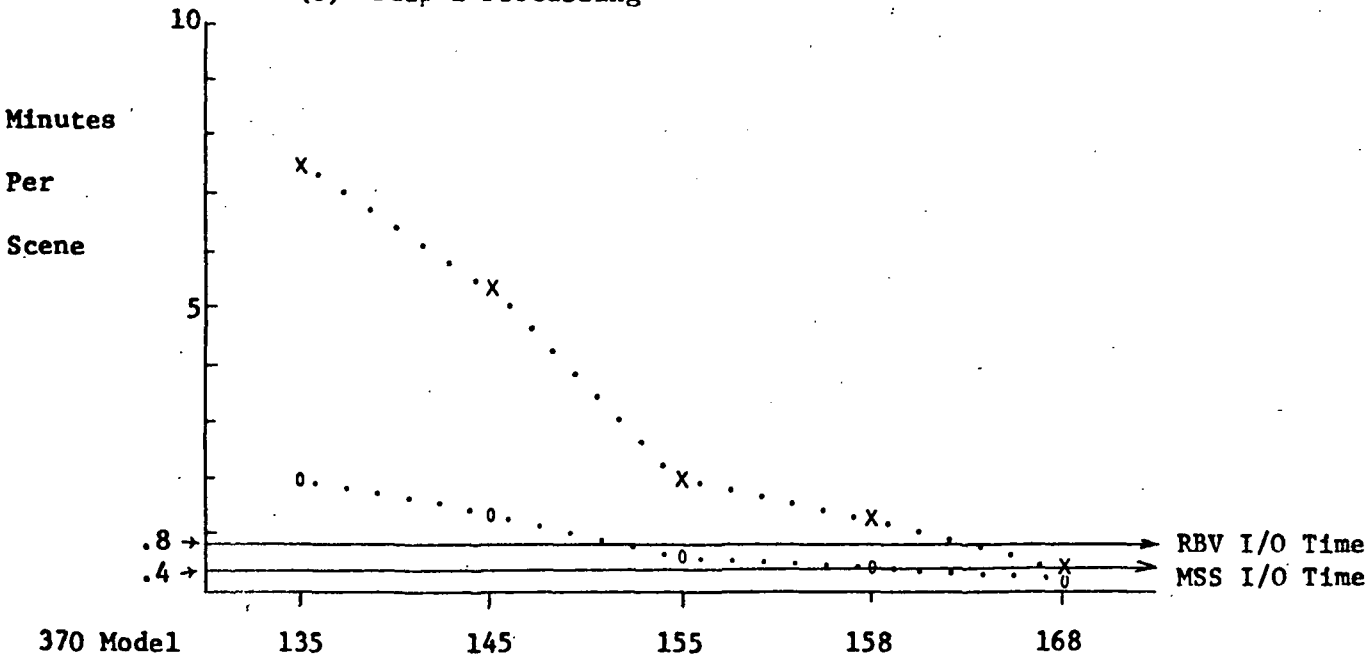
Throughput figures are given in scenes per day, assuming 12 hours per day for the precision processing analyzed here. Many throughput figures are far beyond any daily requirements anticipated but are listed as a measure of excess power available for other tasks, for example, production of user tapes. As mentioned earlier, production of user tapes will be constrained by the I/O to those 800 or 1600 BPI tapes and therefore will differ only negligibly from configuration to configuration.



(a) Step 1 Processing  
Note: I/O and Processing Lines are Coincident



(b) Step 2 Processing



(c) Step 3 Processing

Figure 7-9. Configuration D Processing Times

CONFIGURATION D SUMMARY

370 MODEL		135		145		155		158		168	
		MSS	RBV								
TIME PER SCENE IN MINUTES	SENSOR										
	STEP 1	I .4	I .8								
	STEP 2	3.3	17.2	1.9	10.4	1.0	4.9	.7	3.3	.2	.8
	STEP 3	7.5	2.0	5.3	1.3	2.0	.8	1.2	.8	.4	.8
	TOTAL	11.2	20.0	7.6	12.5	3.4	6.5	2.3	4.9	1.0	2.4
	COMBINED TOTAL	31.2		20.1		9.9		7.2		3.4	
THROUGHPUT	INDIVIDUALLY	64	36	94	57	211	110	313	146	720	300
SCENES/DAY	COMBINED	23		35		72		100		211	
APPROXIMATE	MILLIONS OF \$	1.27		1.87		2.17		2.57		4.57	
COST	PER SCENE A	11.00	19.50	11.00	18.25	5.75	11.00	4.50	9.75	3.50	8.50

A - COST PER SCENE IS AMORTIZED OVER A 5 YEAR PERIOD

I - I/O BOUND OPERATION

**Input Images**

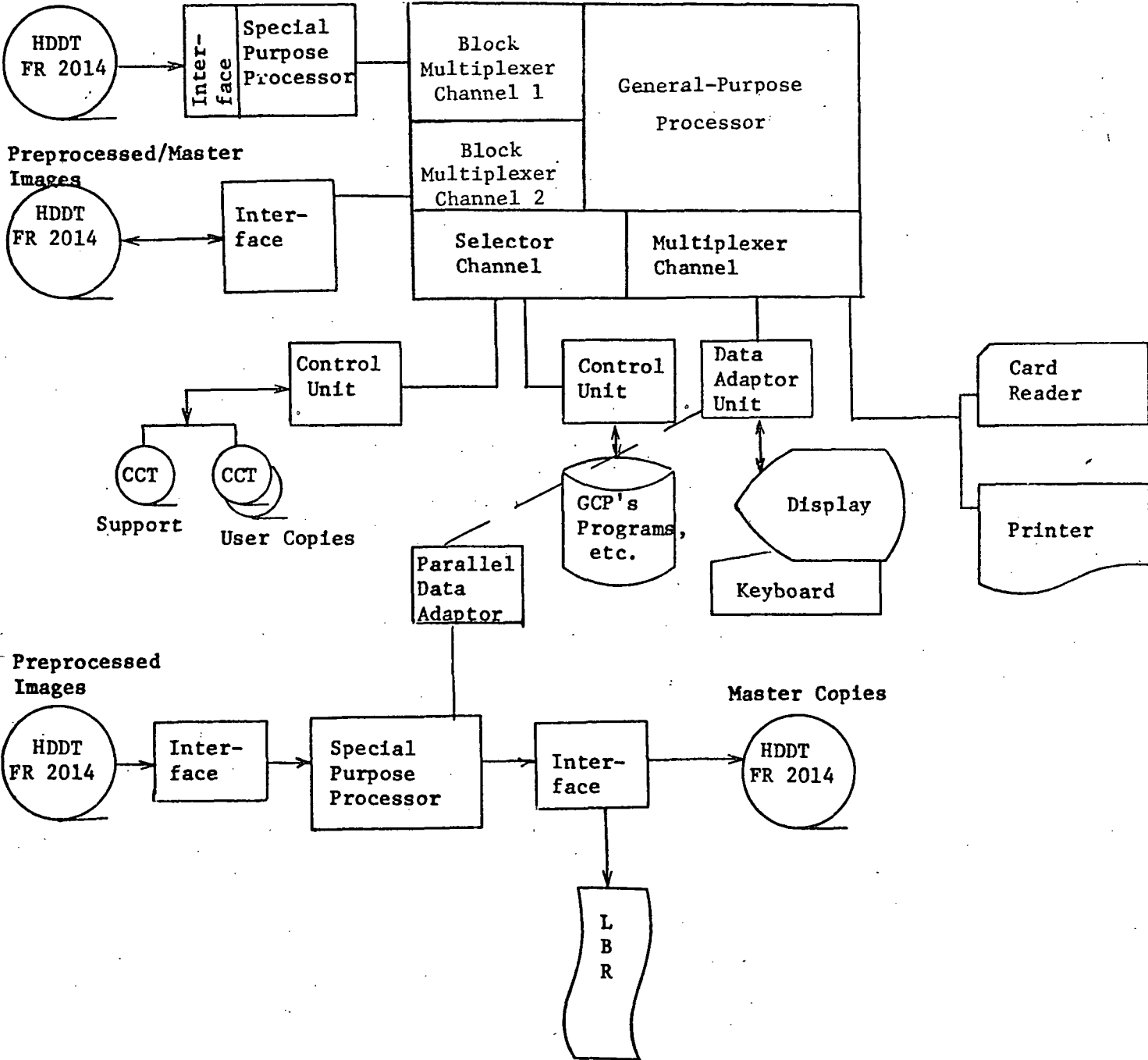
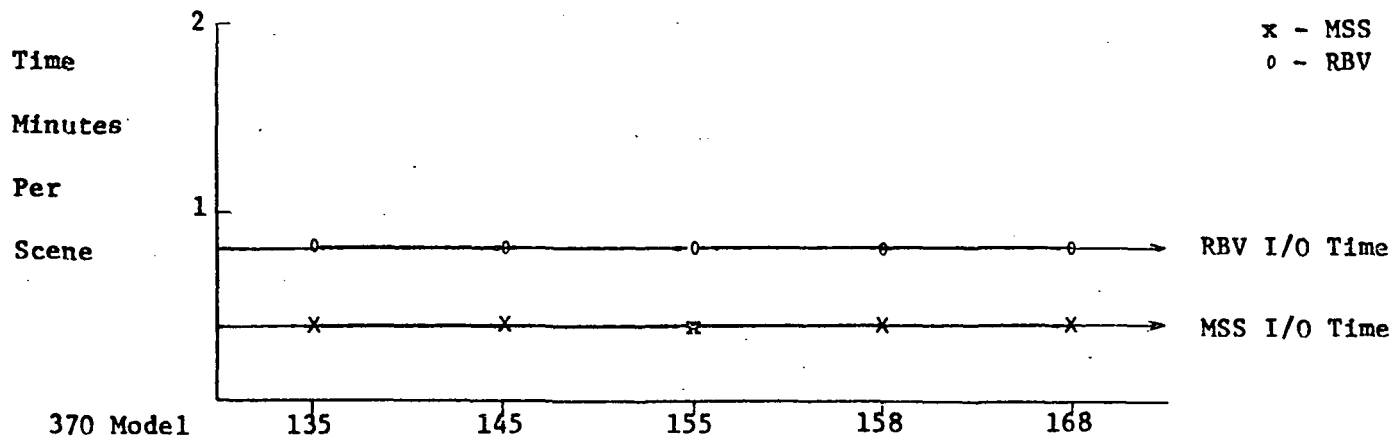
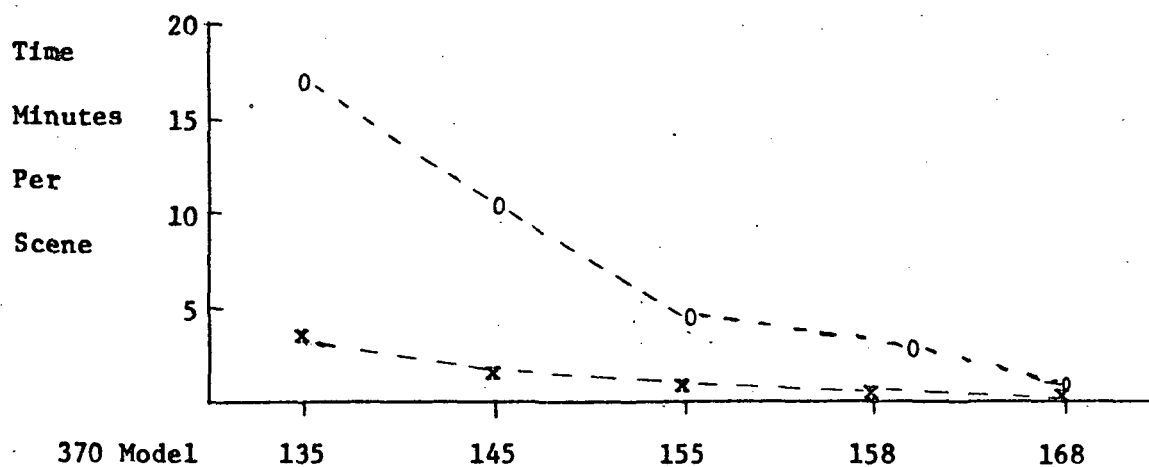


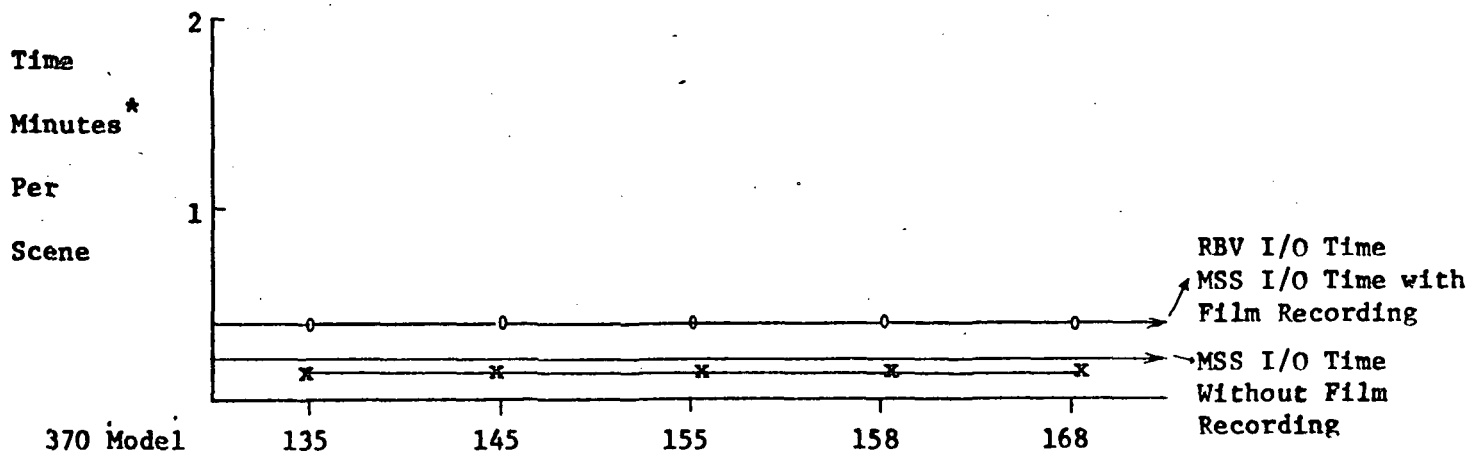
**Figure 7-10. Configuration E Diagram**



(a) Step 1 Processing



(b) Step 2 Processing



(c) Step 3 Processing

\* Step 3 Processing Time is Completely Overlapped on a Parallel Processor.

Note: RBV I/O and Processing Lines are Coincident

Figure 7-11. Configuration E Processing Times

CONFIGURATION E SUMMARY  
(WITHOUT LASER BEAM RECORDER)

370 MODEL		135		145		155		158		168	
SENSOR		MSS	RBV	MSS	RBV	MSS	RBV	MSS	RBV	MSS	RBV
STEP 1		.4 I	.8 I	.4 I	.8 I	.4 I	.8 I	.4 I	.8 I	.4 I	.8 I
STEP 2		3.3	17.2	1.9	10.4	1.0	4.9	.7	3.3	.2	.8
STEP 3		0	0	0	0	0	0	0	0	0	0
TOTAL		3.7	18.0	2.3	11.2	1.4	5.7	1.1	4.1	.6	1.6
COMBINED TOTAL		21.7		13.5		7.1		5.2		2.2	
THROUGHPUT		194	40	313	64	514	126	654	175	1200	450
SCENES/DAY		33		53		101		138		327	
APPROXIMATE		1.74		2.34		2.64		3.04		5.04	
COST		5.00	24.25	4.25	20.25	2.75	11.75	2.50	9.75	2.25	6.25
		A		A		A		A		A	

A - COST PER SCENE IS AMORTIZED OVER A 5 YEAR PERIOD

I - I/O BOUND OPERATION

O - OPERATION COMPLETELY OVERLAPPED ON PARALLEL PROCESSOR

TABLE 7-7

 CONFIGURATION E SUMMARY  
 (WITH LASER BEAM RECORDER)

370 MODEL		135		145		155		158		168	
SENSOR		MSS	RBV	MSS	RBV	MSS	RBV	MSS	RBV	MSS	RBV
STEP 1		.4 I	.8 I	.4 I	.8 I						
STEP 2		3.3	17.2	1.9	10.4	1.0	4.9	.7	3.3	.2	.8
STEP 3		0	0	0	0	0	0	0	0	0	0
TOTAL		3.7	18.0	2.3	11.2	1.4	5.7	1.1	4.1	.6	1.6
COMBINED TOTAL		21.7		13.5		7.1		5.2		2.2	
THROUGHPUT		194		313		514		654		1200	
SCENES/DAY		33		53		101		138		327	
APPROXIMATE		1.99		2.59		2.89		3.29		5.29	
COST	A	5.75	27.75	4.50	22.50	3.25	12.75	2.75	10.50	2.50	6.50

A - COST PER SCENE IS AMORTIZED OVER A 5 YEAR PERIOD

I - I/O BOUND OPERATION

O - OPERATION COMPLETELY OVERLAPPED ON PARALLEL PROCESSOR

SCENE THROUGHPUT SUMMARY

Con-figuration Model Sensor	135			145			155			158			168		
	MSS	RBV	Both	MSS	RBV	Both									
A	25	14	9	43	23	15	86	48	31	107	59	38	141	74	48
B	25	14	9	43	23	15	94	48	32	153	69	48	400	180	124
C	44	34	19	68	54	30	144	93	56	211	118	75	400	200	133
D	64	36	23	94	57	35	211	110	72	313	146	100	720	300	211
E	194	40	33	313	64	33	514	126	101	654	175	138	1200	450	327
E (with LBR)	194	40	33	313	64	53	514	126	101	654	175	138	1200	450	327

TABLE 7-9  
CONFIGURATION COST IN MILLIONS OF DOLLARS

Model Configuration	135	145	155	158	168
	A	.80	1.40	1.70	2.10
BB	.88	1.48	1.78	2.18	4.18
C	1.20	1.80	2.10	2.50	4.50
D	1.27	1.87	2.17	2.57	4.57
E	1.74	2.34	2.64	3.04	5.04
E (with LBR)	1.99	2.59	2.89	3.29	5.29

TABLE 7-10  
PER SCENE COST

Con-figuration Model Sensor	135			145			155			158			168		
	MSS	RBV	Both												
A	17.75	31.75	18.00	33.75	11.00	19.75	11.00	19.75	11.00	19.75	16.25	30.75	16.25	30.75	13.00
B	19.50	35.00	19.00	35.75	10.50	20.50	10.50	20.50	8.00	17.50	6.25	12.50	6.25	12.50	8.50
C	15.00	19.50	14.75	15.50	8.00	12.50	8.00	12.50	6.50	11.75	3.50	8.50	3.50	8.50	6.25
D	11.00	19.50	11.00	18.25	5.75	11.00	5.75	11.00	4.50	9.75	2.25	6.25	2.25	6.25	6.50
E	5.00	24.25	4.25	20.25	2.75	11.75	2.75	11.75	2.50	9.75	2.50	10.50	2.50	10.50	6.50
E (with LBR)	5.75	27.75	4.50	22.60	3.25	12.75	3.25	12.75	2.75	10.50	2.50	10.50	2.50	10.50	6.50

Section 8. REFERENCES

1. R. Bernstein. "Results of Precision Processing (Scene Correction) of ERTS-1 Images Using Digital Image Processing Techniques," Symposium on Significant Results Obtained From the Earth Resources Technology Satellite-1, March 1973.
2. R. Bernstein. "All-Digital Precision Processing of ERTS Images," Interim Report for Period March - July 1972, August 1972.
3. R. Bernstein, et al. "Experimental ERTS Image Processing," IBM report CESC-70-0465, 18 May 1970.
4. R. Bernstein and H. F. Silverman. "Digital Techniques for Earth Resources Image Data Processing," IBM REPORT FSC 71-6017, 30 September 1971.
5. H. Markarian, et al. "Digital Correction for High-Resolution Images," Photogrammetric Engineering, December 1973.
6. R. B. McEwen. "Geometric Accuracy of IBM Precision Image Processing," United States Department of the Interior, Geological Survey, Memo for the Record (ERTS EC-21), November 29, 1973.
7. D. I. Barnea and H. F. Silverman. "A Class of Algorithms for Fast Digital Image Registration," IEEE Transactions on Computers, February 1972.
8. D. I. Barnea and H. F. Silverman. "The Class of Sequential Similarity Detection Algorithms (SSDAs) for Fast Digital Image Registration," IBM Research report RC-3356, 10 May 1971.
9. S. S. Rifman and D. M. McKinnon. "Evaluation of Digital Correction Techniques for ERTS Images - Final Report," TRW report 20634-6003-TU-00, March 1974.

## APPENDIX A

### MSS PRECISION PROCESSING ERROR ANALYSIS

The effects of error sources of three types are considered in this analysis: input errors, internal errors, and propagated errors. Input errors are constants or distributions which are based on information external to the MSS precision processing system. Internal errors result from approximations in mathematical models, so that a process having accurate input produces erroneous output. Propagated errors are transmitted (in general nonlinearly) by a process, so that erroneous input must be compared with erroneous output. The results reported in Section 5 include effects of significant errors in the three categories.

#### 1. Analysis Plan

Figure A-1 shows the geometric corrections and transformations of the MSS precision process, and the input errors for the process. Details of the process were reported in References 1 and 2.

Figure A-2 shows the grouping of consecutive corrections and/or transformations for purposes of the error analysis. The GCPCOR subroutine, which is iterated in Figure A-1, is shown only once in Figure A-2, since what is sought for each "box" is the sensitivity matrix which relates the  $\Delta x$ ,  $\Delta y$  errors in the Ground Control Points (GCP's) on the image to the  $\Delta x$ ,  $\Delta y$  errors in the same points after the corrections indicated in the figure have been made. The elements of the sensitivity matrix are partial derivatives of the values of output variables of a process with respect to the input variables. Therefore the sensitivity matrix is a function of the operating state vector, whose components in this case are attitude and altitude parameters. Since the attitude angles are small (1 degree or less), one pass through GCPCOR with an initial estimate of each angle equal to zero should define the operating state vector with sufficient accuracy for the purpose of sensitivity matrix computation. Spacecraft velocity measurement error, which is shown as an input to GCPCOR in Figure A-1, was specified by GSFC as a one-sigma error of 0.003 m/sec. Since this value is considered negligible, the error source is not shown in Figure A-2.

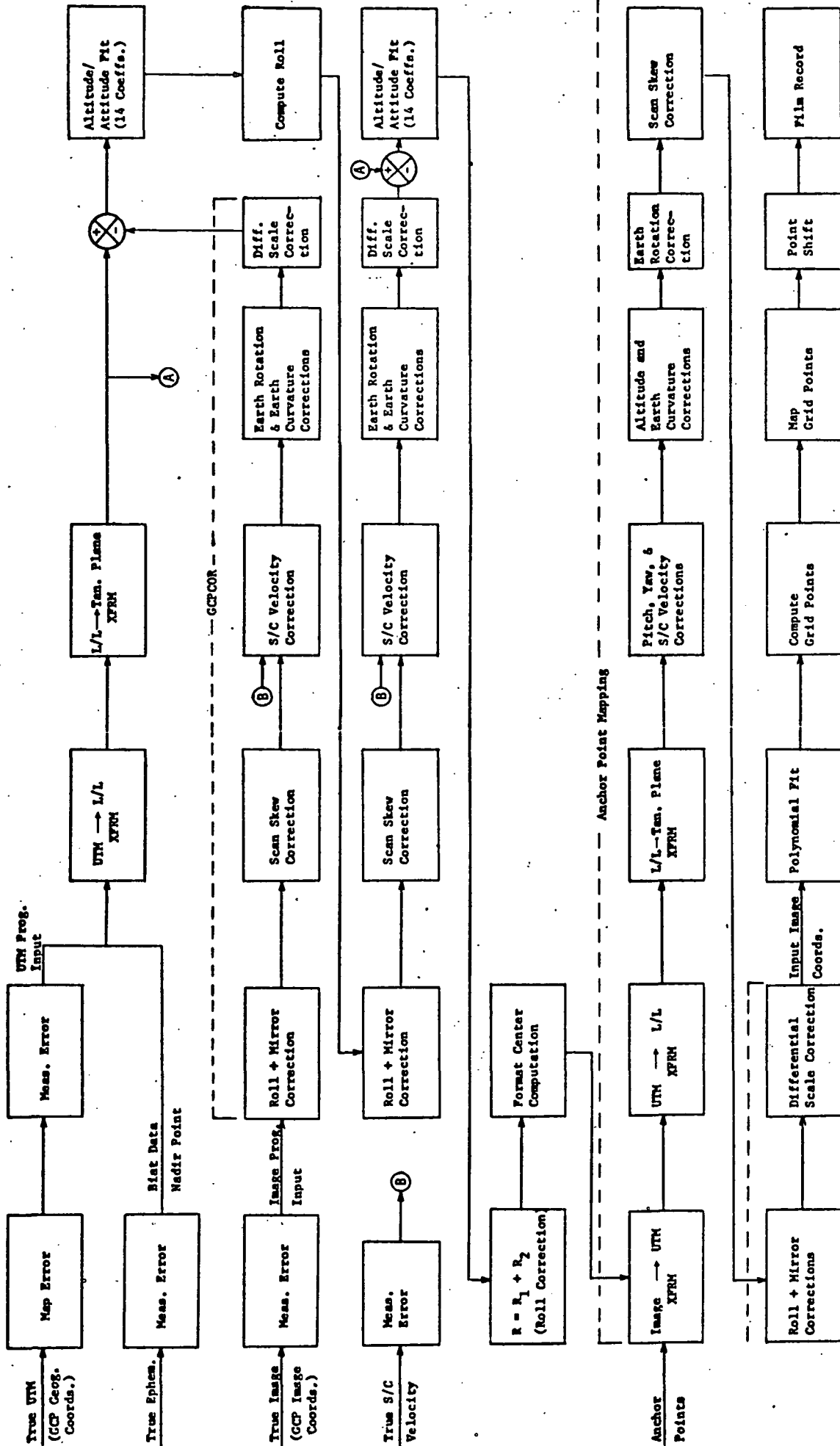
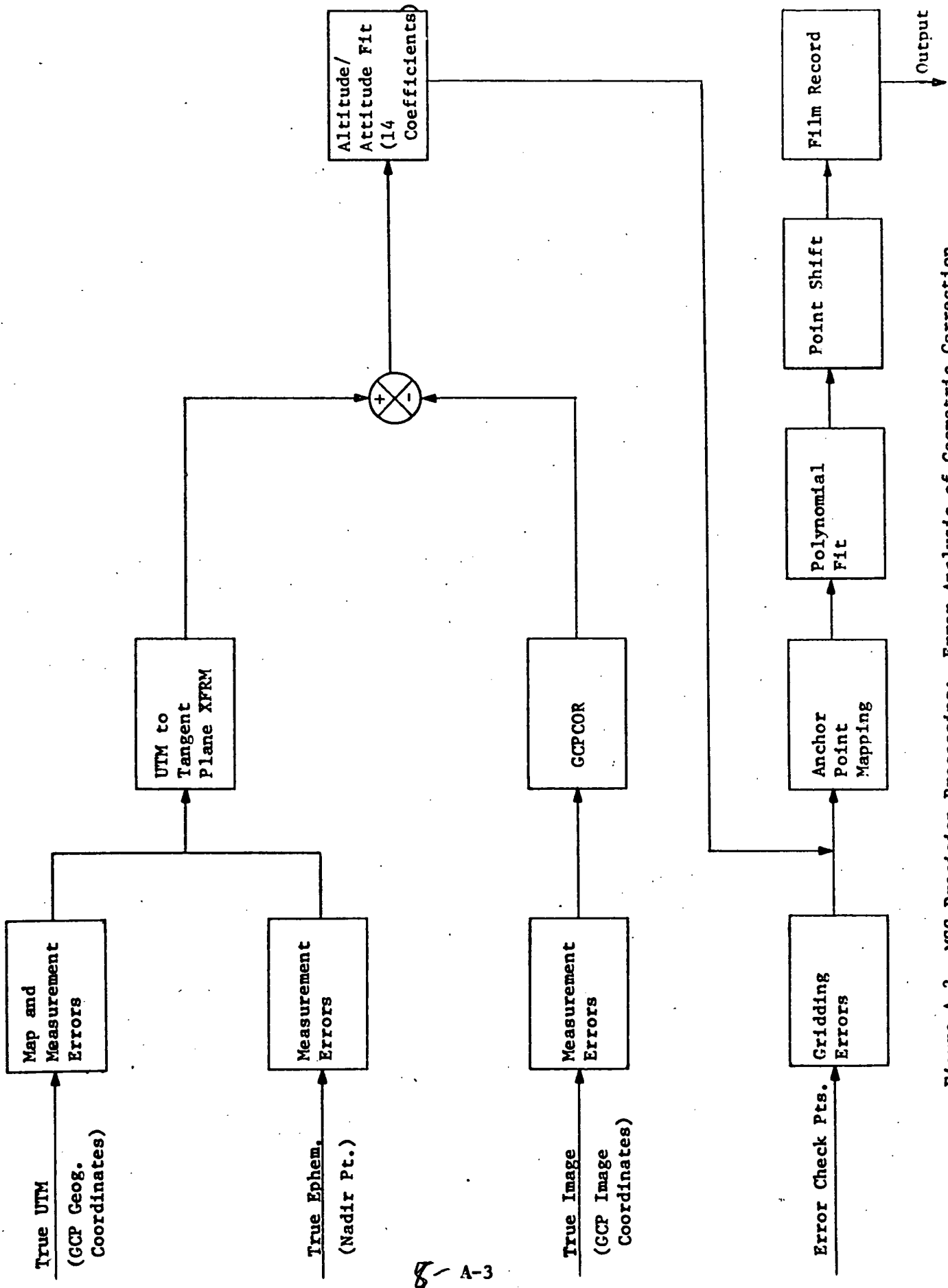


Figure A-1. MSS Precision Processing: Geometric Correction



8-A-3

Figure A-2. MSS Precision Processing: Error Analysis of Geometric Correction

Also in Figure A-2, a set of uniformly distributed error check points is indicated as input to the anchor point mapping subroutine. The output-to-input mapping of each of these points is subject to grid computation errors, anchor point mapping errors, error due to the fitting of a bivariate quintic polynomial to the anchor point mapping function, error due to the point shift algorithm, and film recording error.

The error check points are shown in Figure A-3 and summarized in Table A-1. The rectangular grid containing these check points includes 90% of the area of the output image. In Section 5 two sets of diagrams of one-standard-deviation error ellipses centered at the check points are shown. One set of relative error ellipses includes the effect of the bias error introduced by computing positions relative to the format center; the other set of absolute error ellipses does not include this bias. Composite error ellipses of both types are shown with and without the effect of film recording errors.

## 2. Input Errors

As defined in the introduction, input errors are constants or distributions which are based on information external to the MSS precision processing system. These errors are used as input data for the computation of propagated errors discussed in Section 4 and are therefore included in the composite results reported in Section 5. The input errors enter the MSS precision process where shown in Figures A-1 and A-2.

The assumed input error values are summarized in Table A-2 and discussed in the following paragraphs. The results of Section 5 can be modified to reflect different input error assumptions by re-running the programs with inputs different from those of Table A-2.

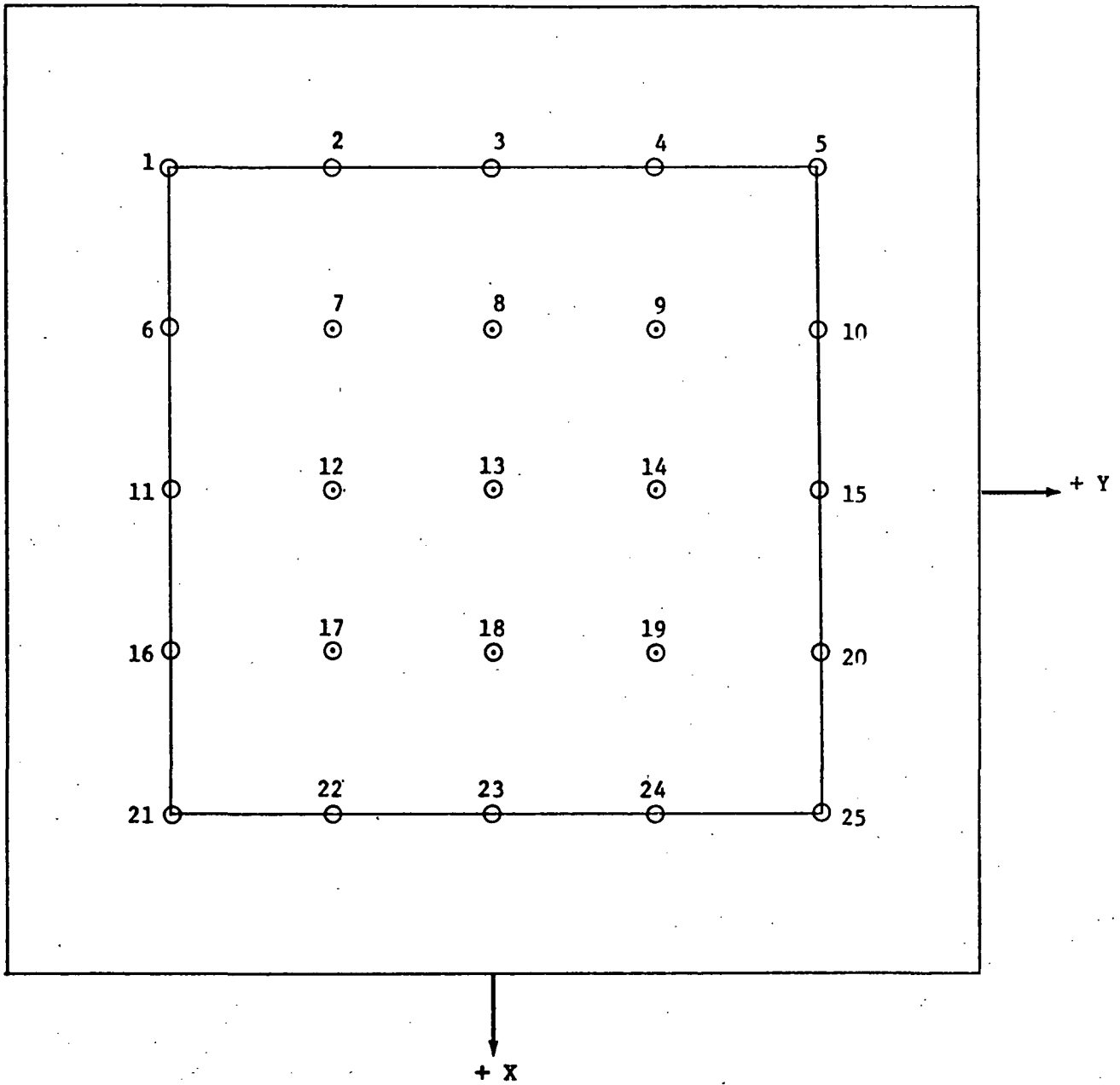


Figure A-3. MSS Error Check Points

Table A-1. MSS Error Check Points

Pt. No.	X	Y
1	-1730	-1730
2	-1730	- 865
3	-1730	0
4	-1730	865
5	-1730	1730
6	- 865	-1730
7	- 865	- 865
8	- 865	0
9	- 865	865
10	- 865	1730
11	0	-1730
12	0	- 865
13	0	0
14	0	865
15	0	1730
16	865	-1730
17	865	- 865
18	865	0
19	865	865
20	865	1730
21	1730	-1730
22	1730	- 865
23	1730	0
24	1730	865
25	1730	1730

(Coordinates are in  
output pixels.)

Table A-2. Input Errors

ERROR SOURCE	ERROR VALUE (1 Standard Deviation)
UTM Map	7.39 m.
UTM Measurement	5.00 m.
Ephemeris ]	[ Composite error: 8.92 m.
Measurement ]	
	Along-track 100.00 m.
	Cross-track 30.00 m.
Image Measurement	0.5 input pixels
S/C Velocity Measurement	zero
Mirror Velocity Correction	0.7 input pixels
Polynomial Fit	0.01 output pixels
Grid Point Computation	0.06 output pixels
Point Shift Algorithm	0.29 output pixels
Film ]	0.391 output pixels
Recording ]	
	Circumferential
	Axial 0.858 output pixels

UTM Map Error. National Map Accuracy Standards<sup>3</sup> specify that 90% of map points must be located with a tolerance of 1/50 inch for scales of 1:20,000 and smaller. The scale of the maps used to locate ground control points (GCP's) is 1:24,000, so that 1/50 inch corresponds to a 1.65-sigma ("sigma" = "standard deviation") error of 40 feet or 12.19 m. Therefore the 1-sigma error is 7.39 m.

UTM Measurement Error. The scale precision used in measuring GCP map locations was 10 m. It was assumed that the 1-sigma error was 5m.

Composite GCP Geographic Location Error. The UTM map and measurement errors were assumed to be independent, and the composite 1-sigma error was calculated to be 8.92 m, which is the RSS (root sum of squares) function of 7.39 m and 5 m.

Ephemeris Measurement Errors. 1-sigma errors in nadir point location<sup>4</sup> are the following: along-track (latitudinal), 100 m; cross-track (longitudinal), 30 m.

Image Measurement Error. The 1-sigma error in input image location of GCP's is estimated to be 0.5 pixel. This estimate is based on experience in interpretation of computer shade prints.

Spacecraft Velocity Measurement Error. The 1-sigma error in spacecraft velocity measurement<sup>4</sup> is 3 mm/sec, relative to nominal velocity of 7.39 km/sec. This error is considered to be effectively zero.

Mirror Velocity Correction Error. Data contained in Reference 5 was used to compute an estimate of 1.09 input pixels for the standard deviation of the errors in the ERTS NDPF mirror velocity profile. An independent IBM profile was developed, which corrects images with a mapping error less than that of the ERTS NDPF model. The estimated standard deviation of the IBM profile is 0.7 input pixels.

Polynomial Fit Error. Based on empirical observation of the differences between the Anchor Point Mapping subroutine (APM) and the polynomial approximation of the APM, the 1-sigma error in the latter was estimated to be 0.01 output pixels. The corresponding variance of 0.0001 output pixels has negligible effect on the propagated error.

Grid Point Computation Error. The interpolation grid points are computed so that the magnitude of the interpolation error in either x or y will be less than 0.1 pixel<sup>1</sup>. The error is assumed to be uniformly distributed as indicated by the symbol U[-0.1, 0.1]. The variance of a uniform distribution U[a, b] is given by the formula

$$\sigma^2\{U[a, b]\} = \frac{(b-a)^2}{12} \quad (2.1)$$

Therefore  $\sigma^2\{U[-0.1, 0.1]\} = 0.00333$  and the standard deviation is  $\sigma\{U[-0.1, 0.1]\} = 0.05774$  output pixels.

Point shift Algorithm Error. The "nearest neighbor" replacement procedure of this algorithm induces a maximum error of 0.5 pixels in the magnitude of either x or y. This error is assumed to be U[-0.5, 0.5]. By application of (2.1),  $\sigma^2\{U[-0.5, 0.5]\} = 0.08333$  and the standard deviation is  $\sigma\{U[-0.5, 0.5]\} = 0.28868$  output pixels.

Film Recording Error. An error study was made of the IBM Scanner/Plotter, and the results of this study were obtained<sup>6</sup> in the form of tables of circumferential and axial errors as functions of linear distances measured on the drum. These measurements were converted from mils to output pixels and the standard deviations shown in Table A-2 were computed. One component of the circumferential error was due to circumferential film stretching which occurs in mounting film on the drum. Since this error source was eliminated by a hardware modification, the data was modified so that the standard deviation of the circumferential error does not reflect the film-stretch error source.

### 3. Internal Errors

As defined in the introduction, internal errors result from mathematical approximations, so that a process having accurate input may produce erroneous output.

The following potential sources of internal errors are shown in Figure A-1.

- o Transformation from UTM to latitude/longitude coordinates
- o Transformation from latitude/longitude to tangent plane coordinates
- o Scan skew correction
- o Pitch, yaw, and spacecraft velocity corrections
- o Earth rotation correction
- o Earth curvature correction
- o Differential scaling correction
- o Attitude/altitude fit
- o Roll computation
- o Format Center computation
- o Transformation from image to UTM coordinates.

Each of these error sources is either negligible or does not involve any error approximation, with the exception of the attitude/altitude fit computation. The internal errors are discussed in the following paragraphs.

Transformation from UTM to Latitude/Longitude Coordinates. The program which accomplishes this transformation was obtained from the United States Geological Service (USGS). The mathematical error in this program is effectively zero<sup>7</sup> and IBM tests obtain essentially exact agreement with an independently calculated set of tables<sup>8</sup>.

#### Transformation from Latitude/Longitude to Tangent Plane Coordinates.

This transformation (see Reference 1, page 17) may be written in the form

$$(XT, YT, ZT)' = RMV \quad (3.1)$$

where the prime symbol signifies transposition, M and V are a matrix and vector function, respectively, of latitude, longitude, and azimuth angles. R represents the geocentric distance to a point of interest (e.g., a GCP) and is calculated by the following formula:

$$R^2 = h^2 + 2h \sqrt{A^2 \cos^2 \lambda + B^2 \sin^2 \lambda} + \frac{A^4 \cos^2 \lambda + B^4 \sin^2 \lambda}{A^2 \cos^2 \lambda + B^2 \sin^2 \lambda} \quad (3.2)$$

In the equation stated in Reference 1, the elevation h was assumed to be zero for all points. However, since this assumption would introduce a significant error for an image with a large range of elevation values, the more general function (3.2) was programmed. Examination of (3.2) shows that  $h + B \leq R \leq h + A$  as  $\lambda$  ranges from  $0^\circ$  to  $90^\circ$ . Since GCP's are located on maps with a 10-meter contour interval, it follows that the maximum error in R due to a measurement error h is 5 m. From the preceding inequality, and the fact deduced from (3.1) that R is a scale factor for tangent plane coordinates, it follows that the maximum tangent plane error in either XT or YT ranges from  $1824(\Delta h)/A$  to  $1824(\Delta h)/B$ , where  $\Delta h = 5$  m;  $A = 6,378,165$  m;  $B = 6,356,783$  m;  $1824 =$  maximum output-pixel coordinate for any image point. The maximum tangent plane error in either XT or YT is therefore 0.0014 output pixels, which is negligible. This is the only source of internal error in the transformation.

Scan Skew Correction. The only source of internal error which is reflected in this computation is the spacecraft velocity error, which was reported in Section 2 to be negligible. Since no approximation is used, this process contributes no significant internal error.

Pitch, Yaw, and Spacecraft Velocity Correction. Spacecraft velocity correction does not require mathematical approximation; therefore there is no internal error. Pitch and yaw corrections are applied both in the GCPCOR and Anchor Point Mapping Subroutines of Figure A-1, and are discussed subsequently under the heading "Attitude/Altitude Fit".

Earth Rotation Correction. No mathematical approximation is used in this computation. However, the formula for computing  $v_g$  (subsattellite point velocity in the orbital plane) is the following:

$$v_s = \frac{v^3}{\mu} R_E \left(1 + \frac{\Delta v}{v}\right) \quad (3.3)$$

where  $R_E$  is the geocentric distance to the subsatellite point,  $\mu = 398604 \text{ km}^3/\text{sec}^2$  is the gravitational parameter of earth,  $v = 7.39 \text{ km/sec}$  is the nominal inertial velocity of the spacecraft<sup>9</sup>, and  $\Delta v/v = 0.01$  is the normalized delta velocity ratio, specified on the Bulk Image Annotation Tape (BIAT), over the 27.6-second interval centered around the format center time.  $v$  in this ratio is nominal spacecraft ground track velocity, the product  $v^3 R_E/\mu$  in (3.3) is equal to the nominal subsatellite point velocity and the factor  $1 + (\Delta v/v)$  compensates for the variation from the nominal velocity  $v$ . The only sources of error, other than computational ones, are  $v$  and  $\Delta v/v$  in (3.3). The maximum orbital decay allowed before orbit adjustment, as measured by the decrease in length of the semimajor orbital axis, has been 150 meters<sup>10</sup>, which corresponds to an increase in the value of  $v$  of about 0.00008 km/sec, a negligible amount. The error in  $\Delta v/v$  is about 1%<sup>11</sup>, which implies an error in computing  $v_s$  of about 0.0001 km/sec, since  $\Delta v/v = 0.01$ . Therefore the error in computing the earth rotation correction is negligible.

Earth Curvature Correction. The polynomial formula which includes the MSS earth curvature correction is stated in Reference 1, page 28. The portion of this polynomial which corrects the image Y-coordinate for earth curvature is  $KY^3 + K^2Y^5$ , where  $K = -1/2R_E H$ , and where  $H$  is the nominal spacecraft altitude and  $R_E$  is the radius of the reference ellipsoid. The total image displacement  $\Delta Y$  due to earth curvature can be geometrically shown to be<sup>12</sup>

$$\Delta Y = -DY/R \quad (3.4)$$

where  $R = x^2 + y^2$  is the distance from the format center of the output image to an arbitrary point and

$$D = \frac{R(R_E - \sqrt{R_E^2 - R^2})}{H + R_E - \sqrt{R_E^2 - R^2}} \quad (3.5)$$

is the amount by which an output image point must be moved when mapped into the input image. If (3.5) is binomially expanded as a quotient of two series in powers of  $R/R_E$ , and powers of  $R/R_E$  greater than or equal to 4 are dropped, (3.5) is approximated as

$$D = -KR^3(1 + KR^2) \quad (3.6)$$

where  $K$  has been previously defined. Substituting (3.6) into (3.4), there results the polynomial function

$$\Delta Y = KYX^2 + KY^3 + K^2YX^4 + 2KY^3X^2 + K^2Y^5 \quad (3.7)$$

which is the RBV displacement in  $Y$ . To obtain the MSS displacement previously stated, set  $X = 0$ . The calculation of  $\Delta Y$  is exact, except for the approximation of  $D$ . The values of  $D$  given by (3.5) and (3.6) have been compared for an image with 4125 lines and 4600 pixels per line; the exact and approximate values of  $D$  differ by 0.0004 pixels. Therefore the error in the earth curvature correction is negligible.

Differential Scaling Correction. The process of changing scale (independently for  $x$  and  $y$  coordinates) from input-pixel to output-pixel dimensions is arithmetic, and there is no source of internal error.

Attitude-Altitude Fit. As previously reported<sup>1</sup>, the distortion in a positive MSS image caused by sensor altitude and attitude errors (where  $X = 0$  for each line) can be approximated by the functions

$$\Delta_A X = -H\theta + Y\psi$$

$$\Delta_A Y = (H^2 + Y^2)\phi/H \quad (3.8)$$

where  $\theta$  = pitch,  $\psi$  = yaw, and  $\phi$  = roll. The same displacement can be computed exactly by the following formulas, which are geometrically derived.

$$\begin{aligned} \Delta_E X &= \Delta_\theta X + \Delta_\psi X \\ \Delta_E Y &= \Delta_\phi Y + \Delta_\theta Y + \Delta_\psi Y \end{aligned} \quad (3.9)$$

where the right hand terms are computed as follows:

$$\begin{aligned} \Delta_{\phi} X &= 0 \\ \Delta_{\phi} Y &= \frac{(H^2 + Y^2) \sin \phi}{H \cos \phi - Y \sin \phi} \\ \Delta_{\theta} X &= -H \tan \theta \quad (3.10) \\ \Delta_{\theta} Y &= \frac{1 - \cos \theta}{\cos \theta} Y \\ \Delta_{\psi} X &= (\sin \psi) Y \\ \Delta_{\psi} Y &= (\cos \psi - 1) Y \end{aligned}$$

Approximate errors in the computation of  $\Delta X$  and  $\Delta Y$  are given by

$$\begin{aligned} \delta X &= \Delta_E X - \Delta_A X \\ \delta Y &= \Delta_E Y - \Delta_A Y \end{aligned} \quad (3.11)$$

Preliminary evaluation of (3.11) for a set of eight points uniformly distributed on a circle concentric with an MSS image and containing 68% of the image area showed a maximum radial displacement  $\sqrt{(\delta X)^2 + (\delta Y)^2}$  of 0.13 pixels. This computation assumed the maximum values of  $0.7^\circ$  for pitch and roll,  $1^\circ$  for yaw, and 492.35 n.m. = 17,961.6 pixels for altitude. The 0.13-pixel error was considered significant and was included in the MSS error analysis in the following way. Within the above bounds for  $\phi$ ,  $\theta$ , and  $\psi$ , and for  $\Delta H = \pm 492$  pixels (a liberal estimate corresponding to about 13 n.m.), a hundred vectors ( $\phi$ ,  $\theta$ ,  $\psi$ ,  $H$ ) were randomly selected. For each vector, the errors (3.11) were calculated, together with the variances of the  $\{\delta X\}$  and  $\{\delta Y\}$  distributions. The corresponding covariance matrix for the error check points of Figure A-3 was formulated and introduced into the propagated error computation (see Section 4) at the point of Figure A-2 following the Attitude-Altitude Fit computation.

Roll Computation. This process requires only a numerical evaluation of a fourth-order polynomial whose argument is time and whose coefficients were calculated in the Attitude-Altitude Fit subroutine. There is no internal error source.

Format Center Computation. The only computations involved are the transformations from the UTM coordinates to latitude/longitude and from latitude/longitude to the tangent plane. There is no approximation or other source of internal error in these subroutines, as was explained previously in this section.

#### 4. Propagated Errors

Propagated errors were previously defined as those transmitted (in general nonlinearly) by a process, so that output errors must be calculated from input errors. The following procedure is used to carry out these calculations.

For each transformation subprocess shown in Figure A-2 a sensitivity matrix  $M$  is calculated as follows. Let  $\delta\vec{a}$  and  $\delta\vec{b}$  be the respective error vectors of the variable input and output vectors,  $\vec{a}$  and  $\vec{b}$ , for a given subprocess. Then the matrix  $M$  is defined by the equation

$$\delta\vec{b} = M\delta\vec{a} \quad (4.1)$$

where if  $M = (m_{ij})$ , the matrix element  $m_{ij}$  signifies the partial derivative of  $b_i$  with respect to  $a_j$ . In general,  $m_{ij}$  is a function of the state vector, whose elements may be such parameters as ground control point measurements, image location of point, nominal altitude, and nominal attitude. Now let  $a_j$  vary to  $a_j + \Delta a_j$ , where  $\vec{a} = (a_1, a_2, \dots)$  is nominal, and compute  $\Delta b_i$  ( $i = 1, 2, \dots$ ). Then

$$m_{ij} = \Delta b_i / \Delta a_j \quad (4.2)$$

If  $C_a$  and  $C_b$  are the variance/covariance matrices of  $\delta\vec{a}$  and  $\delta\vec{b}$ , respectively, and  $E$  means "expected value of", then  $C_a = E[(\delta\vec{a})(\delta\vec{a})^T]$  and  $C_b = E[(\delta\vec{b})(\delta\vec{b})^T]$  by definition, and  $C_b$  can be expressed in terms of  $C_a$  by the following argument:

$$C_b = E[(\delta\vec{b})(\delta\vec{b})^T] \quad (4.3)$$

Substituting from (4.1) into (4.3), we have

$$\begin{aligned}
 C_b &= E[(M\delta\vec{a})(M\delta\vec{a})^T] \\
 &= E[(M(\delta\vec{a})(\delta\vec{a})^T M^T)] \\
 &= ME[(\delta\vec{a})(\delta\vec{a})^T]M^T \\
 &= MC_a M^T
 \end{aligned}
 \tag{4.4}$$

The numerical approximation (4.2) was used to calculate M for each transformation process of Figure A-2 except for the attitude/altitude fit. In this case, the sensitivity matrix was mathematically formulated in a least-squares sense for an arbitrary set of GCP's, in Reference 1, page 27.

An output matrix  $C_b$  is calculated for each process of Figure A-2. Before being used in the next process,  $C_b$  may be combined with variance values assigned to or calculated for any new parameters which appear in the following process. Since, beginning with the introduction of error check points in Figure A-2,  $C_b$  consists of the respective variances  $(\sigma_x)^2$  and  $(\sigma_y)^2$  of the displacements  $\Delta x$  and  $\Delta y$  at each of the 25 points of Figure A-3, an error ellipse with semi-axes  $\sigma_x$  and  $\sigma_y$  can be plotted at each such point after each process.

The absolute errors, as described in Section 1, were computed at two points in the process of Figure A-2. First, they were calculated with the point-shift error included, but without film recording errors. Second, they were calculated for the total MSS process, including film recording errors. In both cases,  $\sigma_x$  and  $\sigma_y$  were computed at each of the 25 error check points of Figure A-3.

After the absolute errors were calculated, errors relative to the format center (see Section 1) were calculated at each error check point in the following manner. A new relative-error sensitivity matrix for anchor point mapping was calculated by subtracting the two row-vectors corresponding respectively to the x- and the y-coordinates of the format center from the

two sets of row-vectors respectively containing values of partial derivatives relative to x and y. The new sensitivity matrix contains zero values in the format center rows and the values in the other rows are relative to zero.

The variance/covariance matrix due to point-shift error relative to the format center was calculated as follows, where a subscript zero corresponds to the format center, a prime symbol identifies absolute values, and unprimed symbols identify relative values. It is assumed that  $(\delta_{x0})^2 = 0$  and it is known that

$$(\delta_x)^2 = \text{var}(x' - x'_0) = (\sigma'_x)^2 + (\sigma_{x0})^2 - 2 \text{cov}(x'_0 x'_1)$$

The independence of the variables implies that  $\text{cov}(x'_0 x'_1) = 0$ , and it is assumed that  $(\sigma'_x)^2 = (\sigma'_{x0})^2 = (\sigma_x)^2$ . Therefore  $(\sigma_x)^2 = 2(\sigma'_x)^2$  for all rows not corresponding to the format center. A similar argument shows that  $(\sigma_y)^2 = 2(\sigma'_y)^2$ . Therefore, the new variance/covariance matrix is obtained by setting the format center rows to zero and doubling all other elements in the absolute-valued matrix.

Film errors are assumed to be random over an image, and are always measured relative to a given point on the film. Thus film recording errors in the absolute sense are the same as those in the relative sense.

## 5. Results

Figures A-4 through A-7 show absolute and relative error ellipses at each of the 25 error check points of Figure A-3, both including and excluding film recording errors. The corresponding data is contained in Tables A-3 through A-6, respectively. Table A-7 summarizes overall RMS and maximum errors for both error classes, absolute and relative.

In each table, the RSS (root sum of squares) is computed at each point by the formula

$$\text{RSS} = \sqrt{(\sigma_x)^2 + (\sigma_y)^2}$$

The RMS (root mean square) in Table A-7 is calculated by the formula

$$\text{RMS} = \sqrt{\sum (\text{RSS})^2 / N}$$

where N = 25 for absolute errors and N = 24 for relative errors, since in the latter case the format center is excluded.

TABLE A-3. Absolute Errors Including Point Shift and Excluding Film Recording

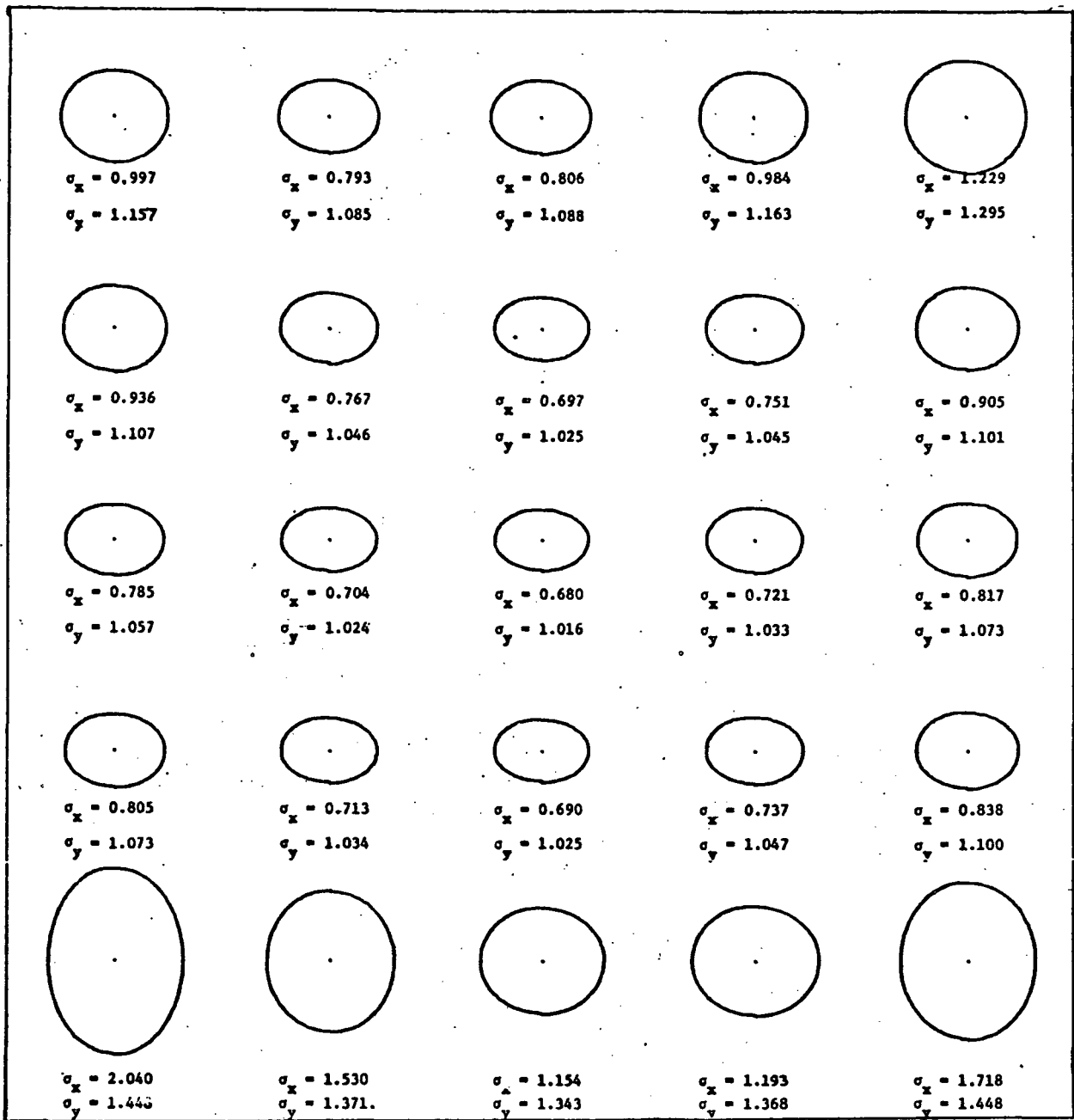
Point No.		1	2	3	4	5
$\sigma_x$	pixels	0.997	0.793	0.806	0.984	1.229
	meters	50.6	40.3	40.9	50.0	62.4
$\sigma_y$	pixels	1.157	1.085	1.088	1.163	1.295
	meters	58.8	55.1	55.3	59.1	65.8
RSS	pixels	1.528	1.343	1.354	1.524	1.785
	meters	77.6	68.2	68.8	77.4	90.7

Point No.		6	7	8	9	10
$\sigma_x$	pixels	0.936	0.767	0.697	0.751	0.905
	meters	47.5	39.0	35.4	38.2	46.0
$\sigma_y$	pixels	1.107	1.046	1.025	1.045	1.101
	meters	56.2	53.1	52.1	53.1	55.9
RSS	pixels	1.450	1.297	1.240	1.287	1.425
	meters	73.6	65.9	63.0	65.4	72.4

Point No.		11	12	13	14	15
$\sigma_x$	pixels	0.785	0.704	0.680	0.721	0.817
	meters	39.9	35.8	34.5	36.6	41.5
$\sigma_y$	pixels	1.057	1.024	1.016	1.033	1.073
	meters	53.7	52.0	51.6	52.5	54.5
RSS	pixels	1.317	1.243	1.223	1.259	1.348
	meters	66.9	63.1	62.1	64.0	68.5

Point No.		16	17	18	19	20
$\sigma_x$	pixels	0.805	0.713	0.690	0.737	0.838
	meters	40.9	36.2	35.0	37.4	42.6
$\sigma_y$	pixels	1.073	1.034	1.025	1.047	1.100
	meters	54.5	52.5	52.1	53.2	55.9
RSS	pixels	1.341	1.256	1.235	1.280	1.383
	meters	68.1	63.8	62.7	65.0	70.3

Point No.		21	22	23	24	25
$\sigma_x$	pixels	2.040	1.530	1.154	1.193	1.718
	meters	103.6	77.7	58.6	60.6	87.3
$\sigma_y$	pixels	1.448	1.371	1.343	1.368	1.448
	meters	73.6	69.6	68.2	69.5	73.6
RSS	pixels	2.501	2.055	1.771	1.815	2.247
	meters	127.1	104.4	90.0	92.2	114.2



(Unit is the Pixel.)

Figure A-4. Absolute Errors Including Point Shift and Excluding Film Recording

TABLE A-4. Absolute Errors Including Film Recording

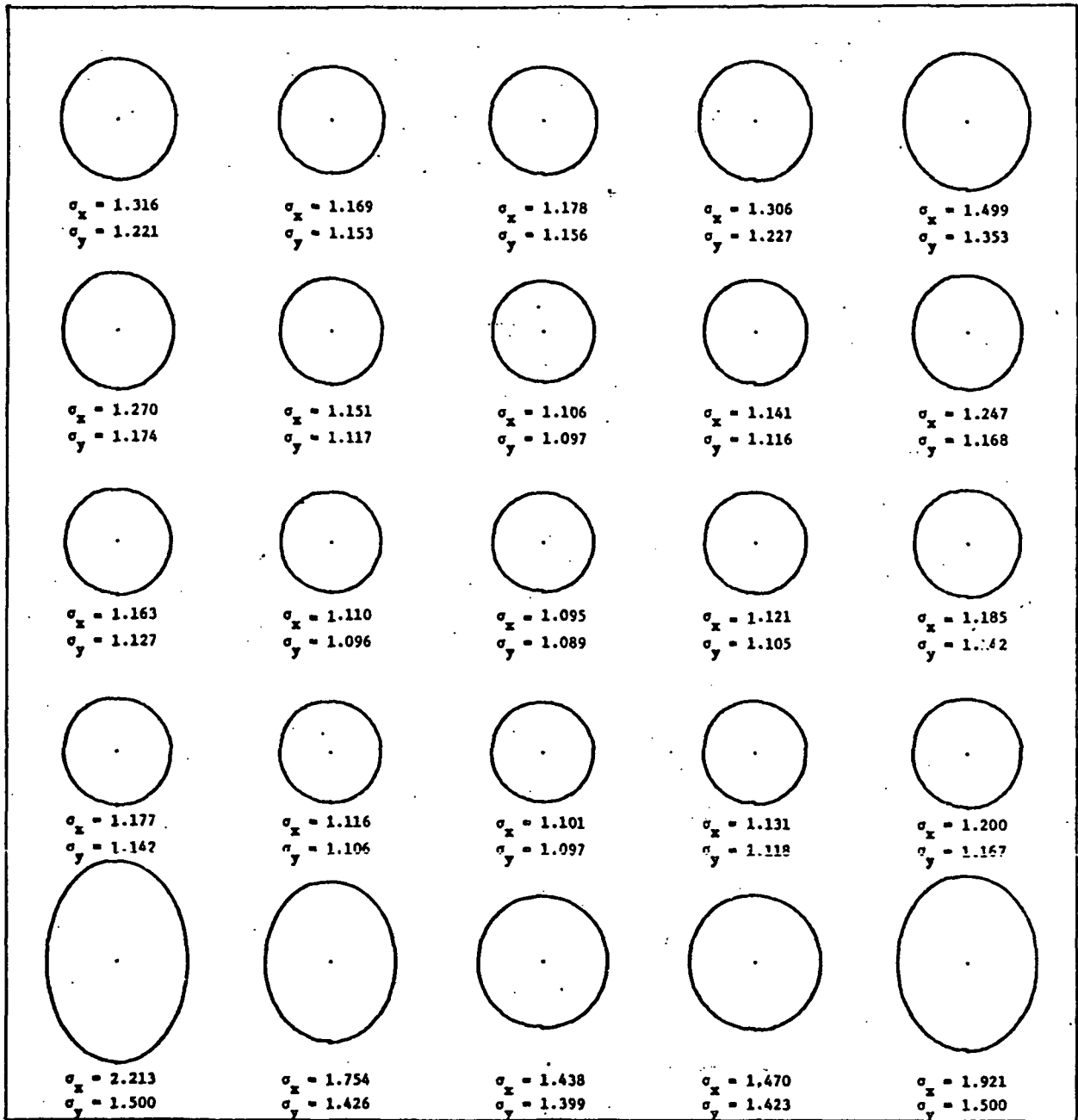
Point No.		1	2	3	4	5
$\sigma_x$	pixels	1.316	1.169	1.178	1.306	1.499
	meters	66.9	59.4	59.8	66.3	76.1
$\sigma_y$	pixels	1.221	1.153	1.156	1.227	1.353
	meters	62.0	58.6	58.7	62.3	68.7
RSS	pixels	1.795	1.642	1.650	1.792	2.019
	meters	91.2	83.4	83.8	91.0	102.6

Point No.		6	7	8	9	10
$\sigma_x$	pixels	1.270	1.151	1.106	1.141	1.247
	meters	64.5	58.5	56.2	58.0	63.3
$\sigma_y$	pixels	1.174	1.117	1.097	1.116	1.168
	meters	59.6	56.7	55.7	56.7	59.3
RSS	pixels	1.730	1.604	1.558	1.596	1.709
	meters	87.9	81.5	79.1	81.1	86.8

Point No.		11	12	13	14	15
$\sigma_x$	pixels	1.163	1.110	1.095	1.121	1.185
	meters	59.1	56.3	55.6	56.9	60.2
$\sigma_y$	pixels	1.127	1.096	1.089	1.105	1.142
	meters	57.3	55.7	55.3	56.1	58.0
RSS	pixels	1.620	1.560	1.544	1.574	1.646
	meters	82.3	79.3	78.4	78.0	83.6

Point No.		16	17	18	19	20
$\sigma_x$	pixels	1.177	1.116	1.101	1.131	1.200
	meters	59.8	56.7	55.9	57.5	60.96
$\sigma_y$	pixels	1.142	1.106	1.097	1.118	1.167
	meters	58.0	56.2	55.7	56.8	59.3
RSS	pixels	1.640	1.571	1.555	1.590	1.674
	meters	83.3	79.8	79.0	80.8	85.0

Point No.		21	22	23	24	25
$\sigma_x$	pixels	2.213	1.754	1.438	1.470	1.921
	meters	112.4	89.1	73.0	74.7	97.6
$\sigma_y$	pixels	1.500	1.426	1.399	1.423	1.500
	meters	76.2	72.4	71.1	72.2	76.2
RSS	pixels	2.674	2.261	2.006	2.046	2.437
	meters	135.8	114.8	101.9	103.9	123.8



(Unit is the Pixel.)

Figure A-5. Absolute Errors Including Film Recording

TABLE A-5. Relative Errors Including Point Shift and Excluding Film Recording

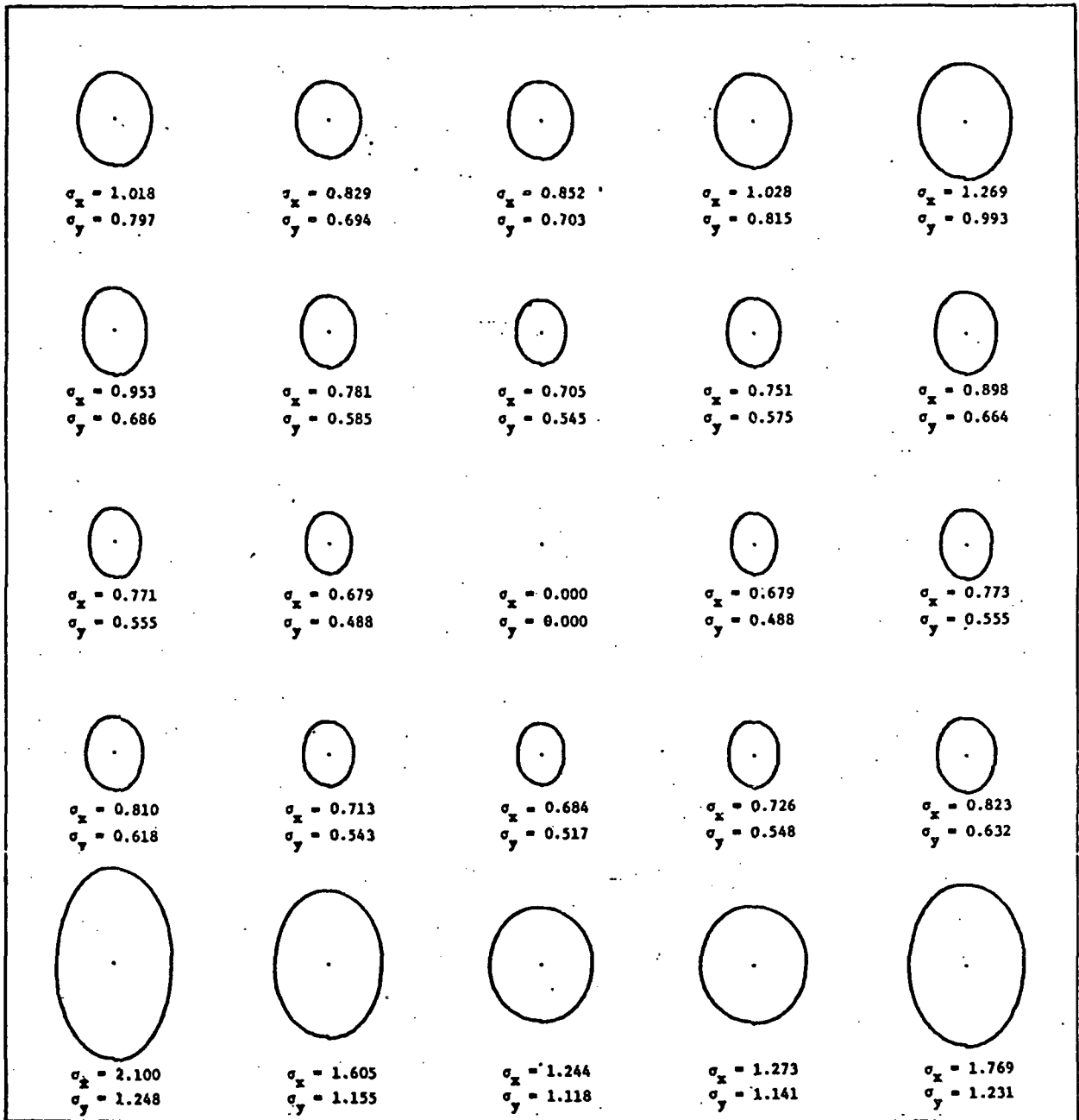
Point No.		1	2	3	4	5
$\sigma_x$	pixels	1.018	0.829	0.852	1.028	1.269
	meters	51.7	42.1	43.3	52.2	64.5
$\sigma_y$	pixels	0.797	0.694	0.703	0.815	0.993
	meters	40.5	35.3	35.7	41.4	50.4
RSS	pixels	1.293	1.081	1.105	1.312	1.611
	meters	65.7	54.9	56.1	66.7	81.9

Point No.		6	7	8	9	10
$\sigma_x$	pixels	0.953	0.781	0.705	0.751	0.898
	meters	48.4	39.7	35.8	38.2	45.6
$\sigma_y$	pixels	0.686	0.585	0.545	0.575	0.664
	meters	34.8	20.4	27.7	29.2	33.7
RSS	pixels	1.174	0.976	0.891	0.945	1.117
	meters	59.6	49.6	45.2	48.0	56.7

Point No.		11	12	13	14	15
$\sigma_x$	pixels	0.771	0.679	0.000	0.679	0.773
	meters	39.2	34.5	0.0	34.5	39.3
$\sigma_y$	pixels	0.555	0.488	0.000	0.488	0.555
	meters	28.2	24.8	0.0	24.8	28.2
RSS	pixels	0.950	0.836	0.000	0.836	0.951
	meters	48.3	42.5	0.0	42.5	48.3

Point No.		16	17	18	19	20
$\sigma_x$	pixels	0.810	0.713	0.684	0.726	0.823
	meters	41.1	36.2	34.7	36.9	41.8
$\sigma_y$	pixels	0.618	0.543	0.517	0.548	0.632
	meters	31.4	27.6	26.3	27.4	32.1
RSS	pixels	1.018	0.896	0.857	0.910	1.038
	meters	51.7	45.5	43.5	46.2	52.7

Point No.		21	22	23	24	25
$\sigma_x$	pixels	2.100	1.605	1.244	1.273	1.769
	meters	106.7	81.5	63.2	64.7	89.9
$\sigma_y$	pixels	1.248	1.155	1.118	1.141	1.231
	meters	63.4	58.7	56.8	58.0	62.5
RSS	pixels	2.443	1.977	1.673	1.710	2.156
	meters	124.1	100.4	85.0	86.9	109.5



(Unit is the Pixel.)

Figure A-6. Relative Errors Including Point Shift and Excluding Film Recording

TABLE A-6. Relative Errors Including Film Recording

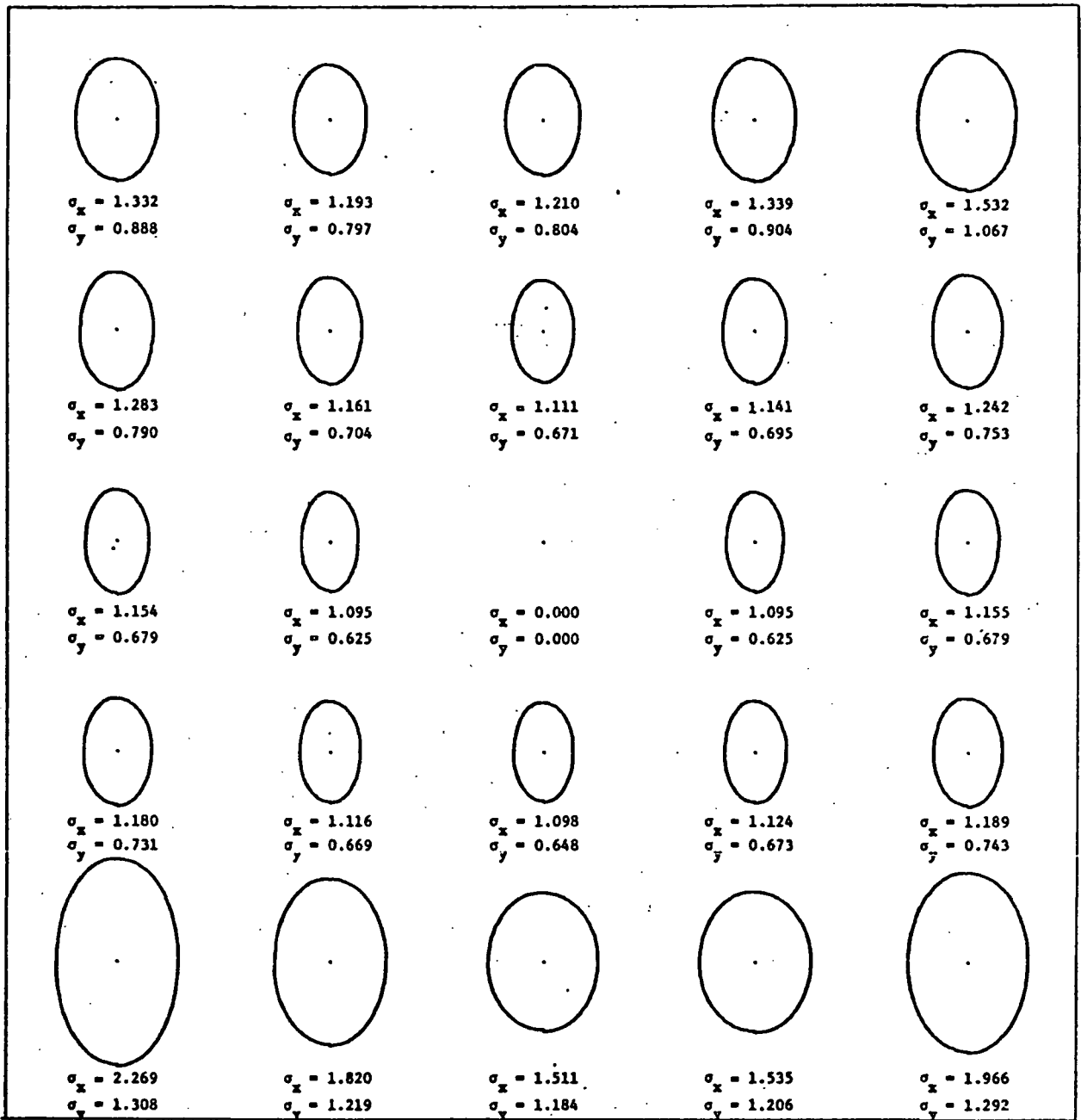
Point No.		1	2	3	4	5
$\sigma_x$	pixels	1.332	1.193	1.210	1.339	1.532
	meters	67.7	60.6	61.4	68.0	77.8
$\sigma_y$	pixels	0.888	0.797	0.804	0.904	1.067
	meters	45.1	40.5	40.9	45.9	54.2
RSS	pixels	1.600	1.435	1.453	1.616	1.867
	meters	81.3	72.9	73.8	82.1	94.9

Point No.		6	7	8	9	10
$\sigma_x$	pixels	1.283	1.161	1.111	1.141	1.242
	meters	65.2	59.0	56.4	57.9	63.1
$\sigma_y$	pixels	0.790	0.704	0.671	0.695	0.753
	meters	40.1	35.7	34.1	35.3	38.3
RSS	pixels	1.506	1.357	1.298	1.336	1.453
	meters	76.5	68.9	65.9	67.9	73.8

Point No.		11	12	13	14	15
$\sigma_x$	pixels	1.154	1.095	0.000	1.095	1.155
	meters	58.6	55.6	0.0	55.6	58.7
$\sigma_y$	pixels	0.679	0.625	0.000	0.625	0.679
	meters	34.5	31.8	0.0	31.8	34.5
RSS	pixels	1.339	1.261	0.000	1.261	1.340
	meters	68.0	64.0	0.0	64.0	68.1

Point No.		16	17	18	19	20
$\sigma_x$	pixels	1.180	1.116	1.098	1.124	1.189
	meters	60.0	56.7	55.8	57.1	60.4
$\sigma_y$	pixels	0.731	0.669	0.648	0.673	0.743
	meters	37.2	34.0	32.9	34.2	37.8
RSS	pixels	1.389	1.301	1.275	1.310	1.402
	meters	70.5	66.1	64.8	66.6	71.2

Point No.		21	22	23	24	25
$\sigma_x$	pixels	2.269	1.820	1.511	1.535	1.966
	meters	115.2	92.5	76.8	78.0	99.9
$\sigma_y$	pixels	1.308	1.219	1.184	1.206	1.292
	meters	66.4	61.9	60.2	61.3	65.6
RSS	pixels	2.619	2.191	1.920	1.953	2.353
	meters	133.0	111.3	97.5	99.2	119.5



(Unit is the Pixel.)

Figure A-7. Relative Errors Including Film Recording

TABLE A-7. Summary of MSS Error Analysis Results

Error Class	Relative Error (Meters)		Absolute Error (Meters)	
	RMS	MAX	RMS	MAX
Including Point Shift and Excluding Film Recording	66.9	124.1	78.1	127.1
Including Film Recording	82.2	133.0	91.6	135.8

6. References

1. Bernstein, R., "All-Digital Precision Processing of ERTS Images", IBM Interim Report for Period March-July 1972, prepared for Goddard Space Flight Center, July 1972.
2. Bernstein, R., "All-Digital Precision Processing of ERTS Images", IBM Interim Report for period August 1972 - June 1973, prepared for Goddard Space Flight Center, July 1973.
3. "National Topographic Map Accuracy Standards", Manual of Photogrammetry, Third Edition, American Society of Photogrammetry, Falls Church, Virginia, 1966, p. 1182.
4. Telephone conversation with Fred Kallmeyer (Goddard Space Flight Center), July 31, 1973.
5. Letter from S. Portner to W. Derouchie. Subject: "Determination of MSS Mirror Velocity Correction Profile", February 27, 1973.
6. Telephone conversation with Thomas Gagnon (IBM, Kingston, N. Y.), August 28, 1973.
7. Telephone conversation with John Rowland (USGS), July 26, 1973.
8. Universal Transverse Mercator Grid Tables for Latitudes 0°-80°, Department of the Army Technical Manual TM 5-241-11, December 1959.
9. Letter from Paul Heffner to Ted Connell. Subject: "User Request for MSS Data", January 24, 1973.
10. Telephone conversation with Lee Smith (Goddard Space Flight Center), August 8, 1973.
11. Telephone conversation with Gerald Grebowsky, (Goddard Space Flight Center), August 9, 1973.
12. Ferneyhough, D.G., Jr., "Geometric Correction of ERTS RBV Images by Automatic Digital Techniques", M.S. Thesis, George Washington University, June 9, 1971.

## APPENDIX B

### RBV PRECISION PROCESSING ERROR ANALYSIS

The effects of error sources of three types are considered in this analysis: input errors, internal errors, and propagated errors. Input errors are constants or distributions which are either assumed or based on information external to the RBV precision processing system. Internal errors result from approximation in mathematical models, so that a process having accurate input produces erroneous output. Propagated errors are transmitted (in general nonlinearly) by a process, so that erroneous input must be compared with erroneous output. The results reported in Section 5 include effects of significant errors in the three categories.

Most of the input and internal error data, as well as the procedure for calculating propagated errors, is the same for the RBV and MSS processes. The later was documented in Appendix A; other references are listed in Section 6 of Appendix A. Where RBV precision processing or error analysis differs from the corresponding MSS process or analysis, the differences are documented in the following sections. Otherwise, Appendix A is quoted.

#### 1. Analysis Plan

Figure B-1 shows the geometric corrections and transformations of the RBV precision process, and the input errors for the process. Details of the process were reported in References 1 and 2.

Figure B-2 shows the grouping of consecutive corrections and/or transformations for purposes of the error analysis. What is sought for each "box" in Figure B-2 is the sensitivity matrix which related the  $\Delta x$ ,  $\Delta y$  errors in the Ground Control Points (GCPs) on the image to the  $\Delta x$ ,  $\Delta y$  errors in the same points after the set of corrections indicated in the figure have been made. The elements of the sensitivity matrix are partial



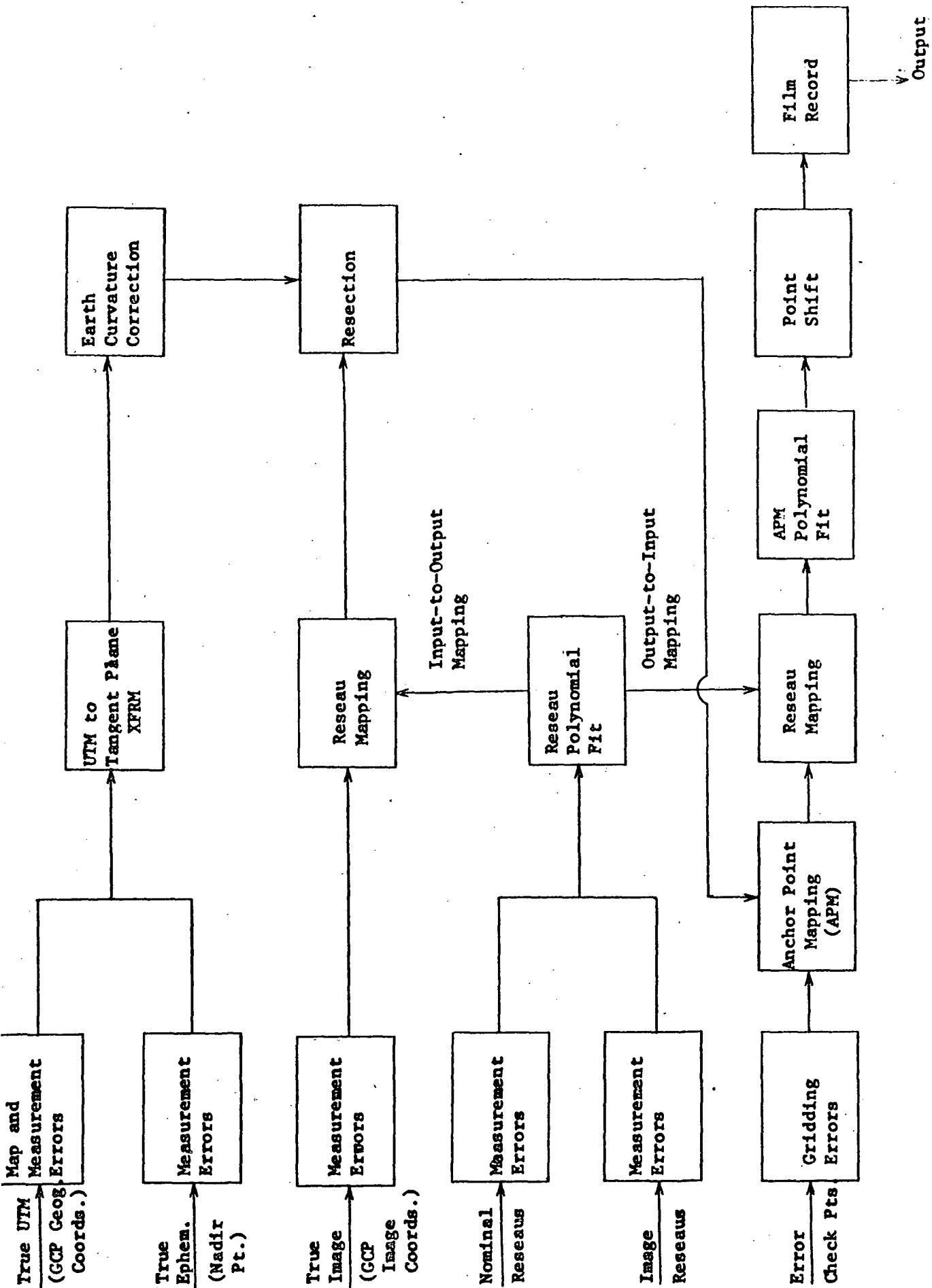


Figure B-2. RBV Precision Processing: Error Analysis of Geometric Correction

derivatives of the values of output variables of a process with respect to the input variables. Therefore, the sensitivity matrix is a function of the operating state vector at a given point in Figure B-2.

Since the coordinates of the anchor points are calculated exactly, the anchor points are not shown as an error source in Figure B-2.

Also in Figure B-2, a set of uniformly distributed error check points is indicated as input to the anchor point mapping subroutine. The output-to-input mapping of each of these points is subject to grid computation errors, anchor point mapping errors, error due to the fitting of a bivariate quintic polynomial to the anchor point mapping function, error due to the point shift algorithm, and film recording error.

The error check points are shown in Figure B-3 and summarized in Table B-1. The rectangular grid containing these check points includes 90% of the area of the output image. In Section 5 two sets of diagrams of one-standard-deviation error ellipses centered at the check points are shown. One set of relative error ellipses includes the effect of the bias error introduced by computing positions relative to the format center; the other set of absolute error ellipses does not include this bias. Composite error ellipses of both types are shown with and without the effect of film recording errors.

## 2. Input Errors

As defined in the introduction, input errors are constants or distributions which are based on information external to the RBV precision processing system. These errors are used as input data for the computation

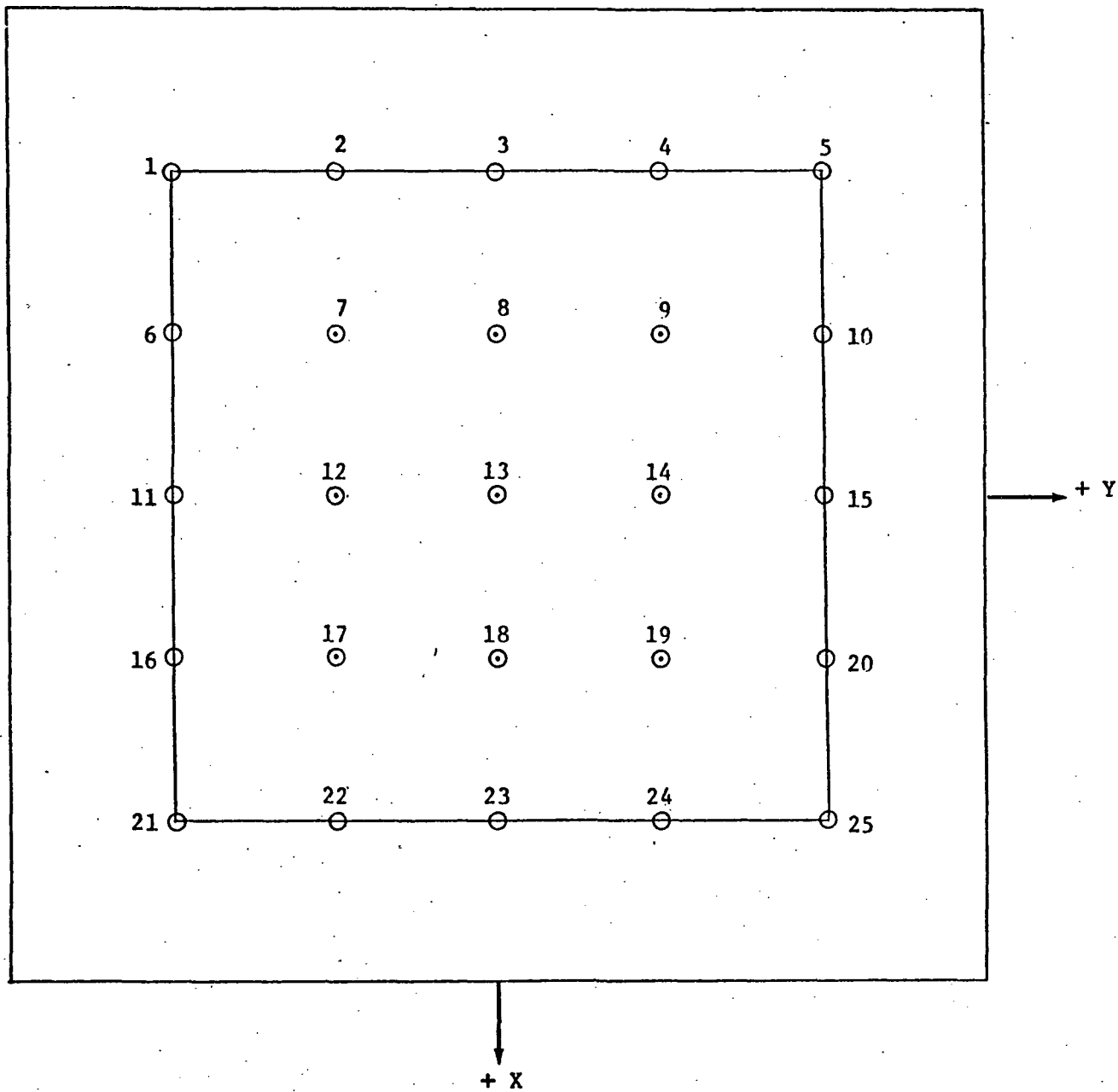


Figure B-3. RBV Error Check Points

TABLE B-1. RBV Error Check Points

Pt. No.	X	Y
1	-1730	-1730
2	-1730	- 865
3	-1730	0
4	-1730	865
5	-1730	1730
6	- 865	-1730
7	- 865	- 865
8	- 865	0
9	- 865	865
10	- 865	1730
11	0	-1730
12	0	- 865
13	0	0
14	0	865
15	0	1730
16	865	-1730
17	865	- 865
18	865	0
19	865	865
20	865	1730
21	1730	-1730
22	1730	- 865
23	1730	0
24	1730	865
25	1730	1730

(Coordinates are  
in output pixels)

of propagated errors discussed in Section 4 and are therefore included in the composite results reported in Section 5. The input errors enter the RBV precision process where shown in Figures B-1 and B-2.

The assumed input error values are summarized in Table B-2 and discussed in the following paragraphs. The results of Section 5 can be modified to reflect different input error assumptions by re-running the programs with inputs different from those of Table B-2.

The error sources and their values shown in Table B-2 are the same as those for the MSS, except that spacecraft velocity measurement and the mirror velocity correction have been deleted, since they are not applicable to the RBV process. Measurement and location errors in reseau points, which are not applicable to the MSS process, have been included in Table B-2.

TABLE B-2. RBV Input Errors

ERROR SOURCE	ERROR VALUE (1 Standard Deviation)
UTM Map	7.39 m.
UTM Measurement	5.00 m.
Ephemeris ] Along-track	100.00 m.
Measurement ] Cross-track	30.00 m.
Image Measurement	0.5 input pixels
Reseaus [ Input Image Location	0.289 input pixels
Reseaus [ Nominal Location Measurement	0.066 input pixels
Polynomial Fit	0.01 output pixels
Grid Point Computation	0.06 output pixels
Point Shift Algorithm	0.29 output pixels
Film ] Circumferential	0.391 output pixels
Recording ] Axial	0.858 output pixels

[ Composite error:  
8.92 m.

**"Page missing from available version"**

The discussion in Appendix A of the first two items and the last two items in the above list applies without change to the RBV process. The MSS internal error sources requiring scan skew, earth rotation, and roll computation corrections are not applicable to the RBV process. The RBV differential scaling correction is included in the reseau mapping sub-routines of Figure B-1, and since no mathematical approximation is involved, this correction is not listed as an RBV internal error source. The three RBV internal error sources which require correction procedures substantially different from those of the MSS process are discussed below.

Earth Curvature Correction. The total image displacements  $\Delta X$  and  $\Delta Y$  due to earth curvature can be geometrically shown to be<sup>12</sup>

$$\begin{aligned}\Delta X &= -DX/R \\ \Delta Y &= -DY/R\end{aligned}\quad (3.1)$$

where D is the function (3.5) of Appendix A. The D approximate (3.6) of Appendix A will not be used in the RBV process. Since the equations (3.1) do not involve approximations, there is no associated internal error source.

Resection. The attitude (pitch, roll and yaw angles) and altitude of the camera at the moment of exposure are calculated by the photogrammetric technique of resectioning. The geometric principle involved (Reference 3, p. 50) is that each image-lens-GCP set of three points is collinear and that any residual discrepancy is attributable to accidental error of image measurement. The resection equations have the form

$$\bar{x} = kM(\bar{X} - \bar{X}_c) \quad (3.2)$$

where  $\bar{x}$  is the vector of image Cartesian coordinates of a set of GCPs,  $\bar{X}$  is the vector of Cartesian geographic coordinates of the same GCPs,  $\bar{X}_c$  is the vector of Cartesian geographic coordinates of the camera, k is a scaling factor, and M is the composite attitude matrix which rotationally relates the ground and camera coordinate systems. When more than

three GCPs are available, a least-squares iterative algorithm is used to solve the error equations. There are three sources of possible error in these calculations: the set of threshold values used to terminate the iterative loop, the noncommutativity of the factors of the M matrix, and the approximation of the M matrix for small values of the attitude angles.

The four attitude values are initialized, and the error equations derived from (3.2) are iteratively solved. Values of the four parameters R, P, Y, and H (roll, pitch, yaw and altitude) are compared with the corresponding values at the end of the previous pass and the calculation is stopped when each difference is less than the appropriate threshold value of 1 microradian (less than 1 m. on the ground) for R, P, Y and 0.1 pixel for H. These errors in the attitude/altitude corrections are negligible.

The matrix M in (3.2) is obtained as the product of three elementary rotation matrices,  $M_P$ ,  $M_R$ , and  $M_Y$ , each of which is a function of one attitude parameter. Since these matrix factors do not commute, the values of the six possible ordered products formed from them were calculated, using the maximum values of  $0.7^\circ$  for pitch and roll and  $1.0^\circ$  for yaw, and all possible sign combinations. The maximum variation in the value of an element of M caused by such permutation of its factors is approximately 0.0003, which corresponds to a displacement of a corner point of an RBV image of about  $8 \times 10^{-8}$  output pixel, which is negligible.

The error equations for the resection calculated are formulated in terms of an approximation  $\bar{M}$  of the matrix M, which is obtained by letting each of the P, R, Y angles approach zero, since their maximum values do not exceed  $1^\circ$ . The maximum displacement of an image point (at a corner) due to this approximation was calculated to be 0.04 output pixels, which is negligible.

In summary, the composite internal error associated with the resection process is negligible.

Roll, Pitch, Yaw, and Altitude Corrections. These corrections are implemented in the RBV process by using exact equations derived from the resection equations. Therefore there are no internal errors associated with these corrections.

#### 4 Propagated Errors

See Appendix A.

#### 5 Results

The discussion in Sections 4 and 5 of Appendix A applies without change to the RBV process.

TABLE B-3. Absolute RBV Errors Including Point Shift and Excluding Film Recording

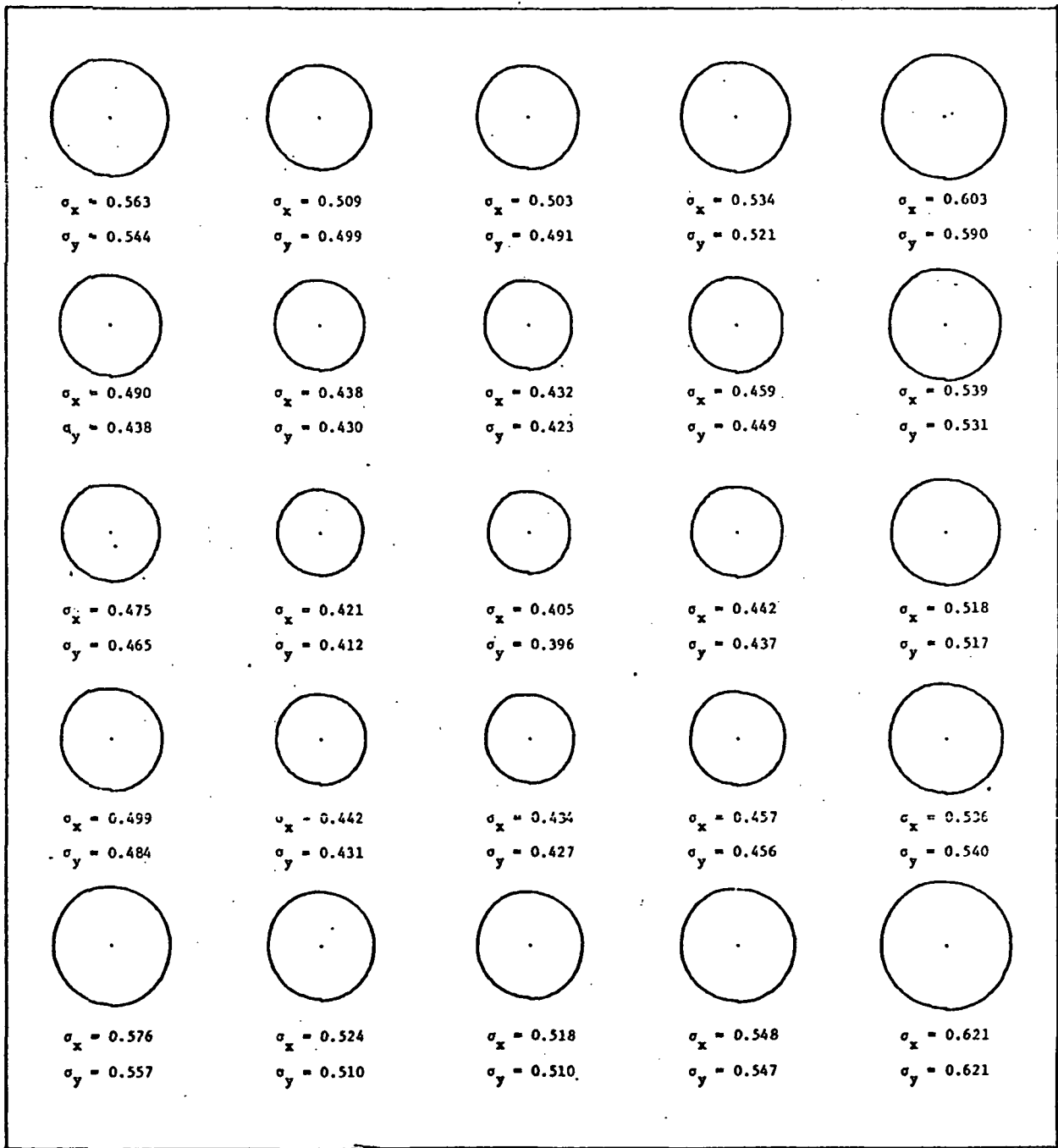
Point No.		1	2	3	4	5
$\sigma_x$	pixels	0.563	0.509	0.503	0.534	0.603
	meters	28.6	25.8	25.5	27.1	30.6
$\sigma_y$	pixels	0.554	0.499	0.491	0.521	0.590
	meters	28.2	25.4	24.9	26.5	30.0
RSS	pixels	0.790	0.713	0.703	0.746	0.844
	meters	40.1	36.2	35.7	37.9	42.9

Point No.		6	7	8	9	10
$\sigma_x$	pixels	0.490	0.438	0.432	0.459	0.539
	meters	24.9	22.2	22.0	23.3	27.4
$\sigma_y$	pixels	0.483	0.430	0.432	0.449	0.531
	meters	24.6	21.8	21.5	22.8	27.0
RSS	pixels	0.688	0.613	0.605	0.642	0.756
	meters	35.0	31.2	30.7	32.6	38.4

Point No.		11	12	13	14	15
$\sigma_x$	pixels	0.475	0.421	0.405	0.442	0.518
	meters	24.1	21.4	20.6	22.5	26.3
$\sigma_y$	pixels	0.465	0.412	0.396	0.437	0.517
	meters	23.6	20.9	20.1	22.2	26.2
RSS	pixels	0.664	0.589	0.566	0.622	0.731
	meters	33.7	29.9	28.8	31.6	37.2

Point No.		16	17	18	19	20
$\sigma_x$	pixels	0.499	0.442	0.434	0.457	0.536
	meters	25.4	22.4	22.0	23.2	27.2
$\sigma_y$	pixels	0.484	0.431	0.427	0.456	0.540
	meters	24.6	21.9	21.7	23.2	27.4
RSS	pixels	0.695	0.617	0.609	0.646	0.761
	meters	35.3	31.4	30.9	32.8	38.7

Point No.		21	22	23	24	25
$\sigma_x$	pixels	0.576	0.524	0.518	0.548	0.621
	meters	29.3	26.6	26.3	27.8	31.5
$\sigma_y$	pixels	0.557	0.510	0.510	0.547	0.621
	meters	28.3	25.9	25.9	27.8	31.5
RSS	pixels	0.802	0.731	0.727	0.774	0.878
	meters	40.7	37.2	36.9	39.3	44.6



(Unit is the pixel.)

**Figure B-4. Absolute RBV Errors Including Point Shift  
and Excluding Film Recording**

TABLE B-4. Absolute RBV Errors Including Film Recording

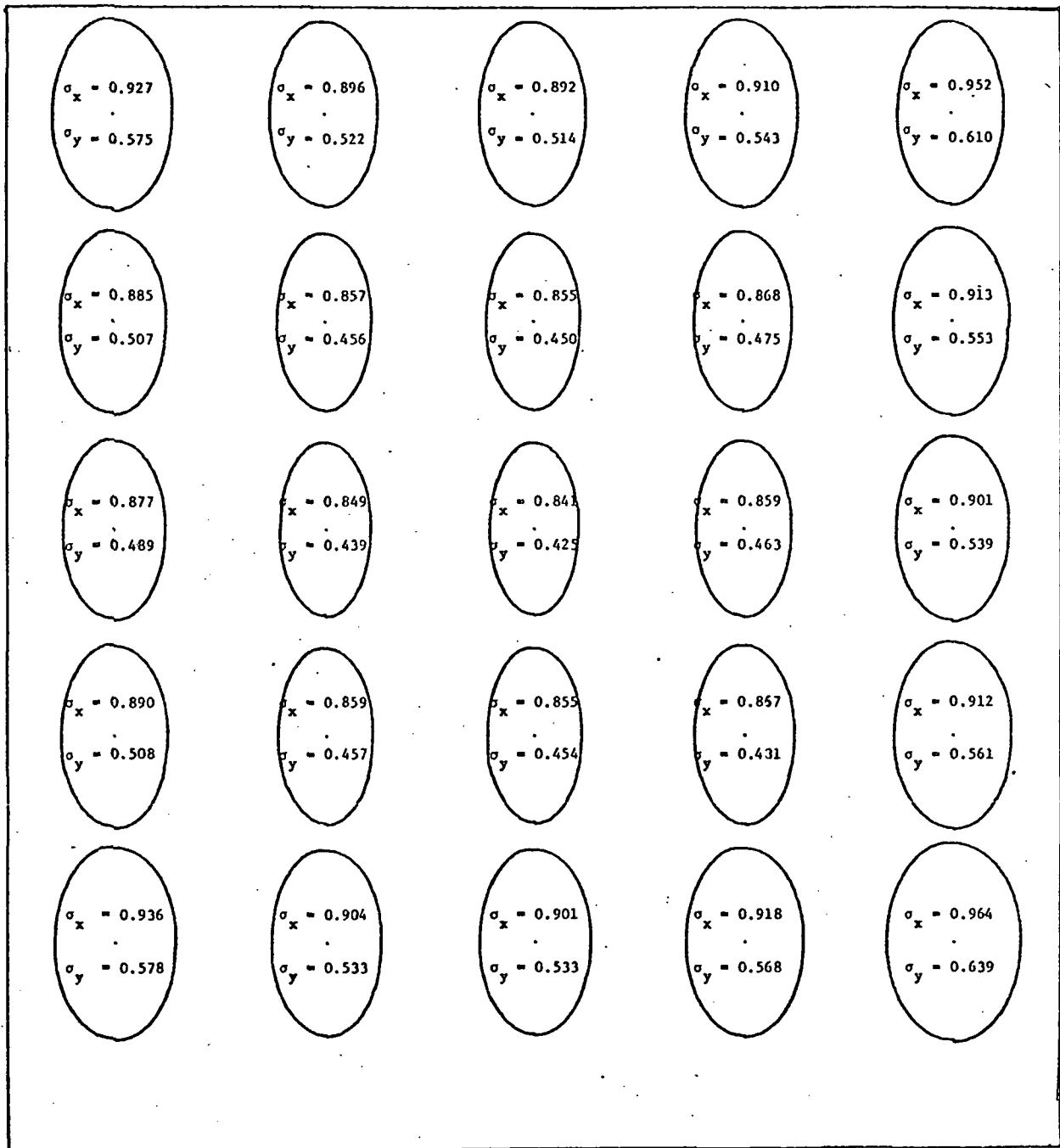
Point No.		1	2	3	4	5
$\sigma_x$	pixels	0.927	0.896	0.892	0.910	0.952
	meters	47.1	45.5	45.3	46.2	48.4
$\sigma_y$	pixels	0.575	0.522	0.514	0.543	0.610
	meters	29.2	26.5	26.1	27.6	31.0
RSS	pixels	1.091	1.037	1.030	1.060	1.131
	meters	55.4	52.7	52.3	53.8	57.4

Point No.		6	7	8	9	10
$\sigma_x$	pixels	0.885	0.857	0.855	0.868	0.913
	meters	44.9	43.5	43.4	44.1	46.4
$\sigma_y$	pixels	0.507	0.456	0.450	0.475	0.553
	meters	25.8	23.2	22.8	24.1	28.1
RSS	pixels	1.020	0.971	0.966	0.989	1.067
	meters	51.8	49.3	49.1	50.3	54.2

Point No.		11	12	13	14	15
$\sigma_x$	pixels	0.877	0.849	0.841	0.859	0.901
	meters	44.5	43.1	42.7	43.7	45.8
$\sigma_y$	pixels	0.489	0.439	0.425	0.463	0.539
	meters	24.8	22.3	21.6	23.5	27.4
RSS	pixels	1.004	0.956	0.942	0.976	1.049
	meters	51.0	48.6	47.9	49.6	53.3

Point No.		16	17	18	19	20
$\sigma_x$	pixels	0.890	0.859	0.855	0.867	0.912
	meters	45.2	43.7	43.4	44.1	46.3
$\sigma_y$	pixels	0.508	0.457	0.454	0.481	0.561
	meters	25.8	23.2	23.0	24.5	28.5
RSS	pixels	1.025	0.973	0.968	0.992	1.070
	meters	52.1	49.4	49.2	50.4	54.4

Point No.		21	22	23	24	25
$\sigma_x$	pixels	0.936	0.904	0.901	0.918	0.964
	meters	47.5	45.9	45.7	46.7	49.0
$\sigma_y$	pixels	0.578	0.533	0.533	0.568	0.639
	meters	29.4	27.1	27.1	28.9	32.5
RSS	pixels	1.100	1.050	1.046	1.080	1.157
	meters	55.9	53.3	53.2	54.9	58.8



(Unit is the pixel.)

Figure B-5. Absolute RBV Errors Including Film Recording

TABLE B-5. Relative RBV errors Including Point Shift and Excluding Film Recording

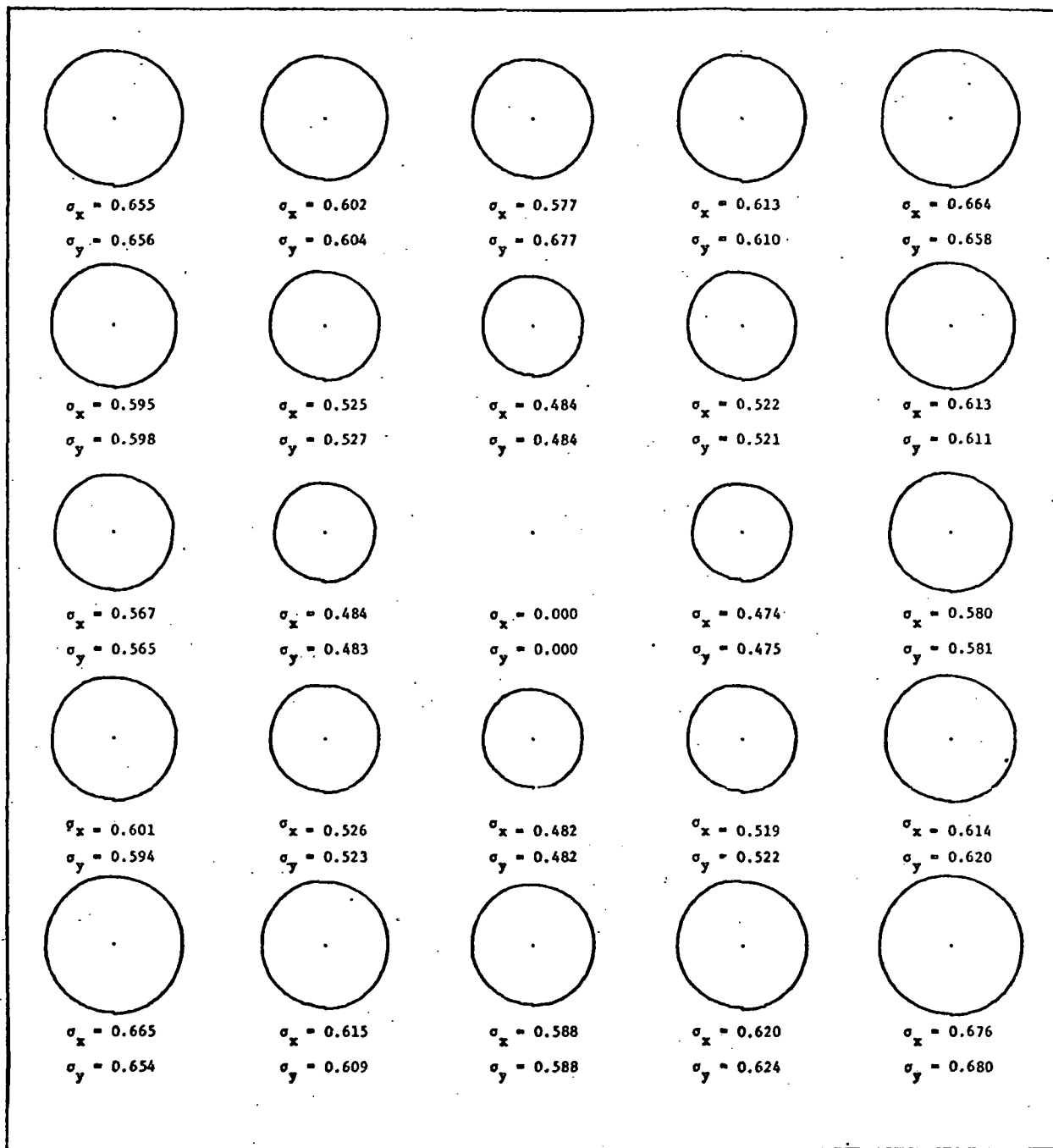
Point No.		1	2	3	4	5
$\sigma_x$	pixels	0.655	0.602	0.577	0.613	0.664
	meters	33.3	30.6	29.3	31.1	33.7
$\sigma_y$	pixels	0.656	0.604	0.577	0.610	0.658
	meters	33.3	30.7	29.3	31.0	33.5
RSS	pixels	0.927	0.853	0.816	0.864	0.935
	meters	47.1	43.3	41.5	43.9	47.5

Point No.		6	7	8	9	10
$\sigma_x$	pixels	0.595	0.525	0.484	0.522	0.613
	meters	30.3	26.7	24.6	26.5	31.2
$\sigma_y$	pixels	0.598	0.527	0.484	0.521	0.611
	meters	30.4	26.8	24.6	26.4	31.0
RSS	pixels	0.844	0.744	0.684	0.737	0.866
	meters	42.9	37.8	34.8	37.5	44.0

Point No.		11	12	13	14	15
$\sigma_x$	pixels	0.567	0.484	0.000	0.474	0.580
	meters	28.8	24.6	0.0	24.1	29.5
$\sigma_y$	pixels	0.656	0.483	0.000	0.475	0.581
	meters	28.7	24.6	0.0	24.1	29.5
RSS	pixels	0.800	0.684	0.000	0.671	0.821
	meters	40.1	34.7	0.0	34.1	41.7

Point No.		16	17	18	19	20
$\sigma_x$	pixels	0.601	0.526	0.482	0.519	0.614
	meters	30.5	26.7	24.5	26.4	31.2
$\sigma_y$	pixels	0.594	0.523	0.482	0.522	0.620
	meters	30.2	26.6	24.5	26.5	31.5
RSS	pixels	0.845	0.742	0.682	0.736	0.872
	meters	42.9	37.7	34.6	37.4	44.3

Point No.		21	22	23	24	25
$\sigma_x$	pixels	0.665	0.615	0.588	0.620	0.676
	meters	33.8	31.2	29.9	31.5	34.3
$\sigma_y$	pixels	0.654	0.609	0.588	0.642	0.680
	meters	33.2	31.0	29.9	31.7	34.6
RSS	pixels	0.933	0.866	0.832	0.880	0.959
	meters	47.4	44.0	42.3	44.7	48.7



(Unit is the pixel.)

Figure B-6. Relative RBV Errors Including Point Shift  
and Excluding Film Recording

TABLE B-6. Relative RBV Errors Including Film Recording

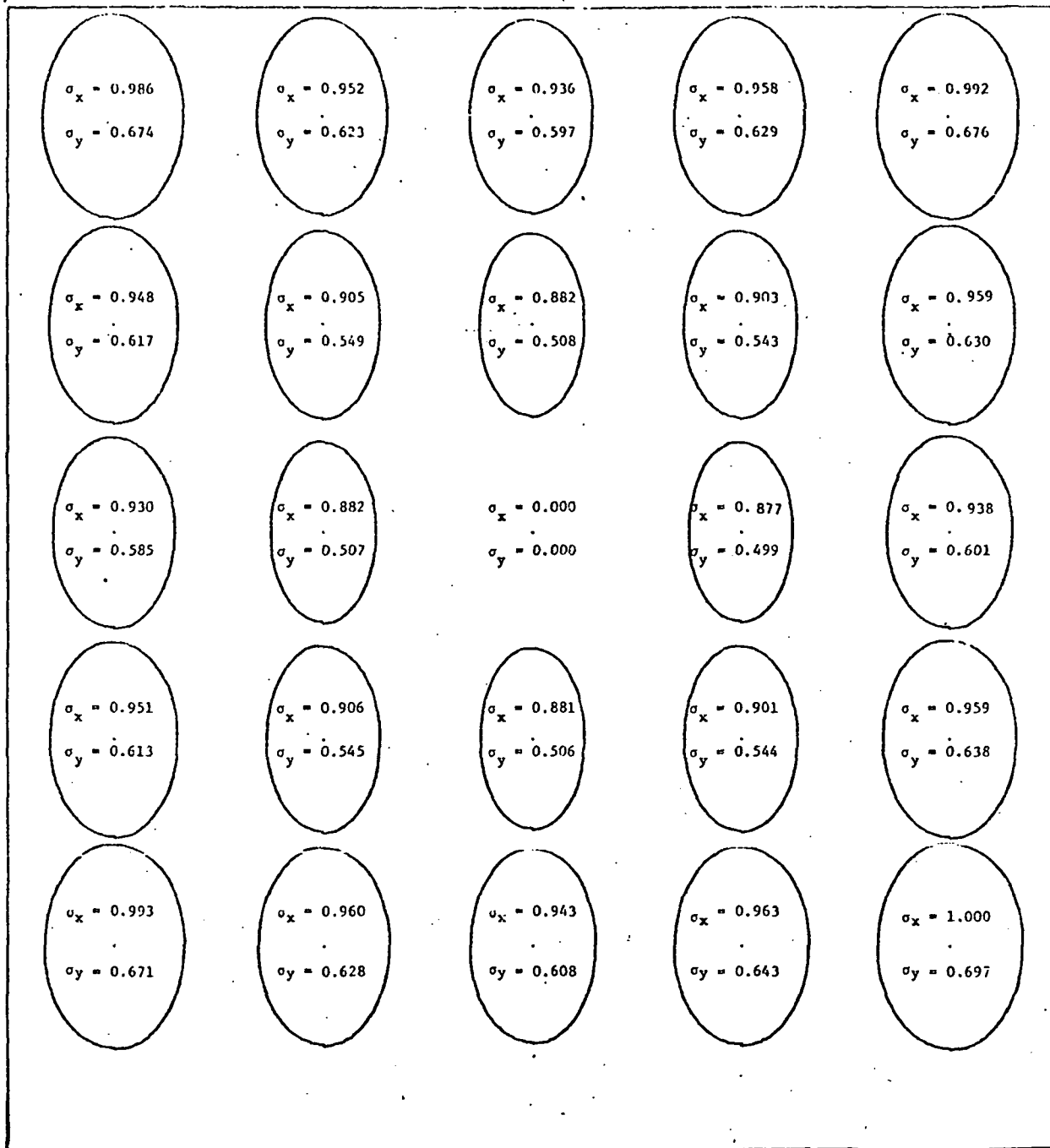
Point No.		1	2	3	4	5
$\sigma_x$	pixels	0.986	0.952	0.936	0.958	0.992
	meters	50.1	48.4	47.6	48.7	50.4
$\sigma_y$	pixels	0.674	0.623	0.597	0.629	0.676
	meters	34.2	31.7	30.4	31.9	34.3
RSS	pixels	1.194	1.138	1.110	1.146	1.200
	meters	60.7	57.8	56.4	58.2	61.0

Point No.		6	7	8	9	10
$\sigma_x$	pixels	0.948	0.905	0.882	0.903	0.959
	meters	48.1	46.1	44.8	45.9	48.7
$\sigma_y$	pixels	0.617	0.549	0.508	0.543	0.630
	meters	31.3	27.9	25.8	27.6	32.0
RSS	pixels	1.131	1.059	1.017	1.054	1.147
	meters	57.4	53.8	51.7	53.5	58.3

Point No.		11	12	13	14	15
$\sigma_x$	pixels	0.930	0.882	0.000	0.877	0.938
	meters	47.2	44.8	0.0	44.5	47.6
$\sigma_y$	pixels	0.585	0.507	0.000	0.499	0.601
	meters	29.7	25.8	0.0	25.3	30.5
RSS	pixels	1.099	1.017	0.000	1.009	1.114
	meters	55.8	51.7	0.0	51.2	56.6

Point No.		16	17	18	19	20
$\sigma_x$	pixels	0.951	0.906	0.881	0.901	0.959
	meters	48.3	46.0	44.7	45.8	48.7
$\sigma_y$	pixels	0.613	0.545	0.506	0.544	0.638
	meters	31.2	27.7	25.7	27.6	32.4
RSS	pixels	1.131	1.057	1.016	1.053	1.152
	meters	57.5	53.7	51.6	53.5	58.5

Point No.		21	22	23	24	25
$\sigma_x$	pixels	0.993	0.960	0.943	0.963	1.000
	meters	50.4	48.8	47.9	48.9	50.8
$\sigma_y$	pixels	0.671	0.682	0.608	0.643	0.697
	meters	34.1	31.9	30.9	32.6	35.4
RSS	pixels	1.199	1.147	1.122	1.158	1.219
	meters	60.9	58.3	57.0	58.8	61.9



(Unit is the pixel.)

Figure B-7. Relative RBV Errors Including Film Recording

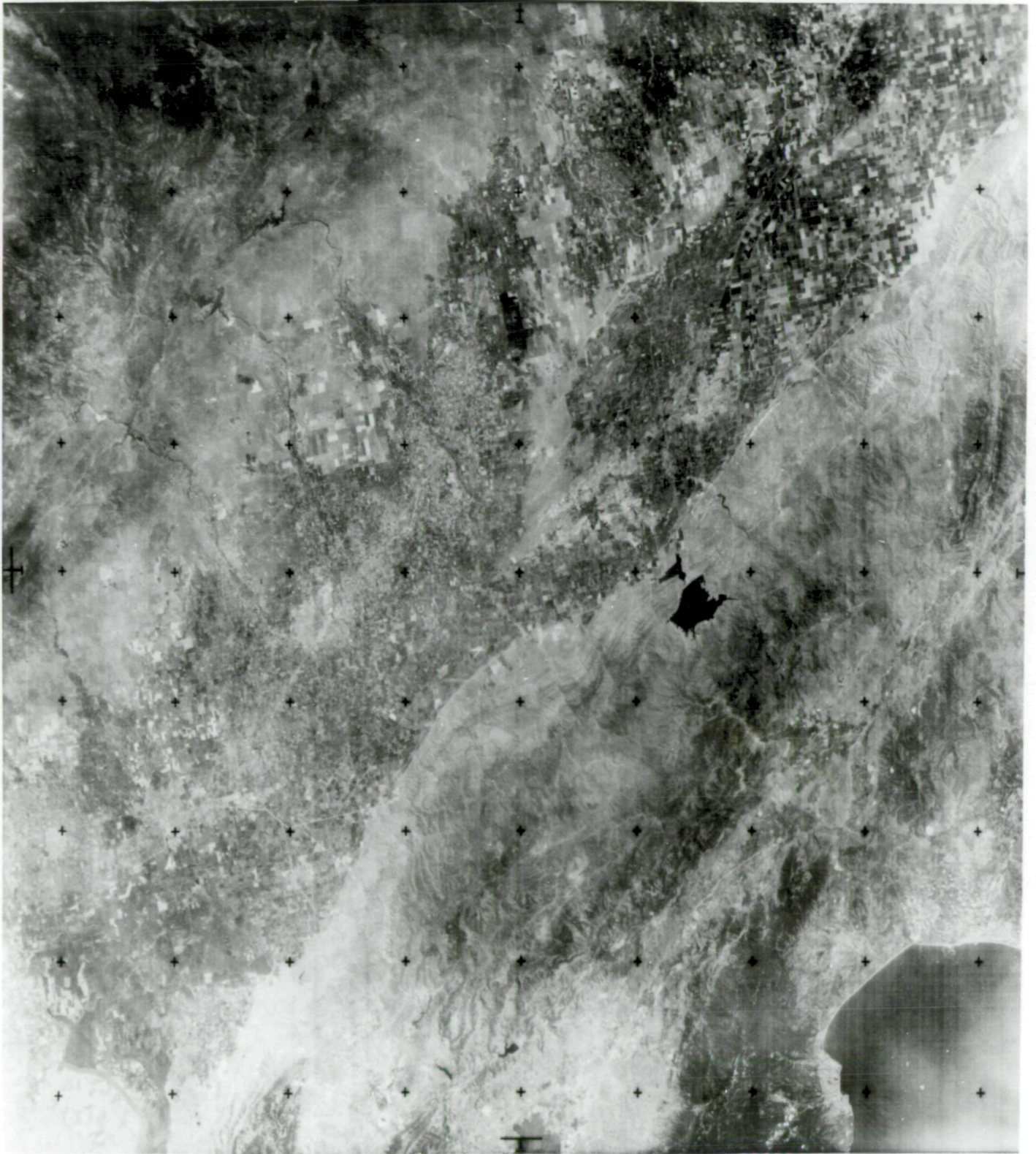
TABLE B-7. Summary of RBV Error Analysis Results

ERROR CLASS	Relative Error (Meters)		Absolute Error (Meters)	
	RMS	MAX	RMS	MAX
Including Point Shift and Excluding Film Recording	41.8	48.7	35.8	44.6
Including Film Recording	56.6	61.9	52.4	58.8

6. References

1. Bernstein, R., "All-Digital Precision Processing of ERTS Images", IBM Interim Report for Period March-July 1972, prepared for Goddard Space Flight Center, July 1972.
2. Bernstein, R., "All-Digital Precision Processing of ERTS Images", IBM Interim Report for period August 1972 - June 1973, prepared for Goddard Space Flight Center, July 1973.
3. "National Topographic Map Accuracy Standards", Manual of Photogrammetry, Third Edition, American Society of Photogrammetry, Falls Church, Virginia, 1966, p. 1182.
4. Telephone conversation with Fred Kallmeyer (Goddard Space Flight Center), July 31, 1973.
5. Letter from S. Portner to W. Derouchie. Subject: "Determination of MSS Mirror Velocity Correction Profile", February 27, 1973.
6. Telephone conversation with Thomas Gagnon (IBM, Kingston, N. Y.), August 28, 1973.
7. Telephone conversation with John Rowland (USGS), July 26, 1973.
8. Universal Transverse Mercator Grid Tables for Latitudes 0°-80°, Department of the Army Technical Manual TM 5-241-11, December 1959.
9. Letter from Paul Heffner to Ted Connell. Subject: "User Request for MSS Data", January 24, 1973.
10. Telephone conversation with Lee Smith (Goddard Space Flight Center), August 8, 1973.
11. Telephone conversation with Gerald Grebowsky, (Goddard Space Flight Center), August 9, 1973.
12. Ferneyhough, D.G., Jr., "Geometric Correction of ERTS RBV Images by Automatic Digital Techniques", M.S. Thesis, George Washington University, June 9, 1971

Figure 2-2  
Monterey - Band 1  
After Radiometric Correction



B

USH NRSR EPTS 1  
06 OCT 73 C N38-53/W076-55 N N38-52/W076-48

SUN EL40 AZ147 190-6134 -1- 0-

SLAVE PROCESSED BY IBM  
NRSR EPTS E-1440-15175- 6

W077°30

W077°00

W076°30

W076°00

139°30

139°00

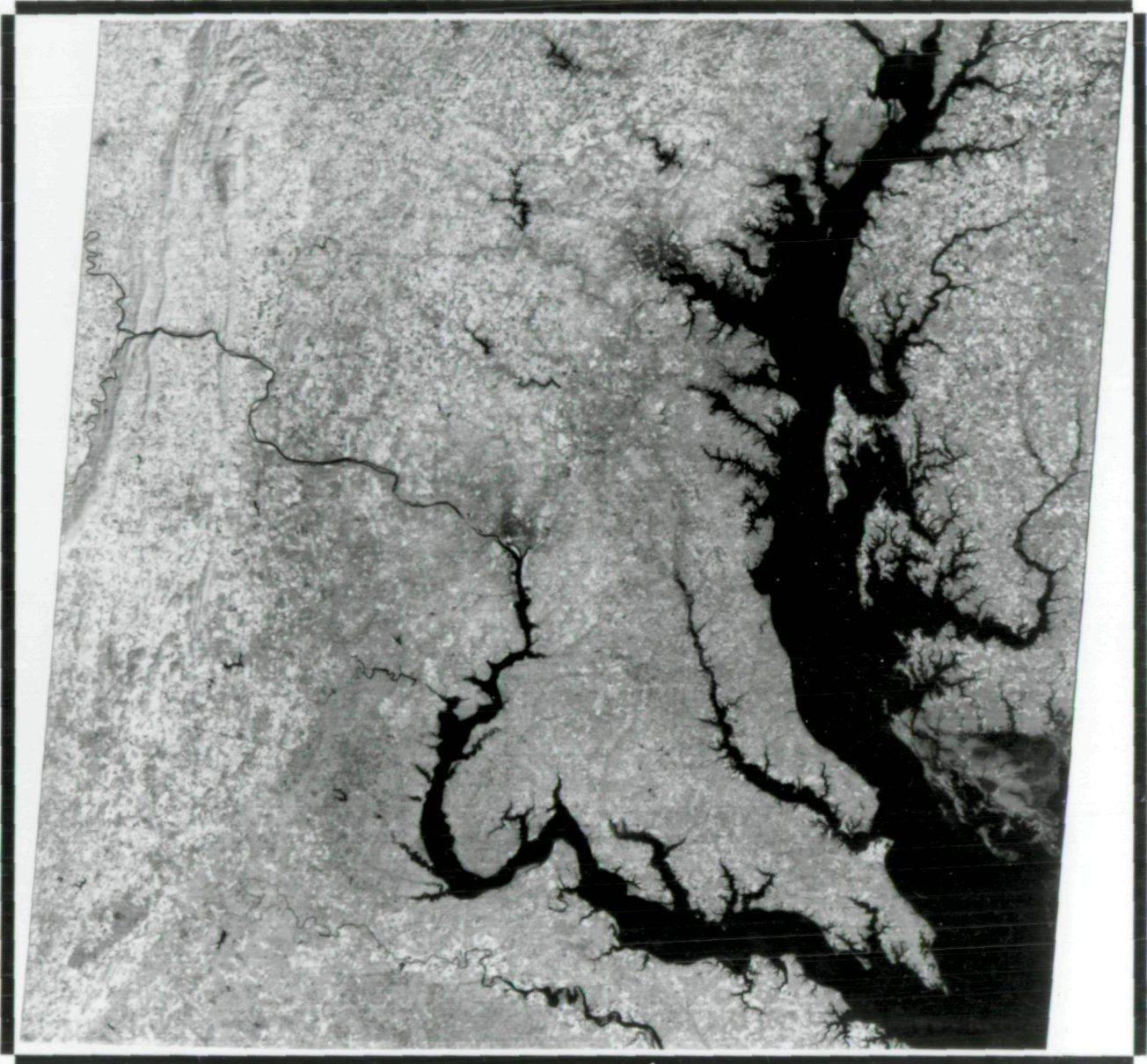
N  
138°30

35

30

25

4  
200  
000



250000 UTM

30

35

40

FORMAT CENTER:  
UTM N4305127, E335009, Z18  
GEODETTIC N38.8814°/W076.9020°

KILOM  
ST MI

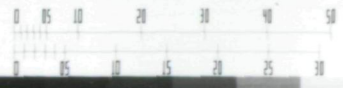


IMAGE IDENTIFICATION:  
IMAGED AT 1517 GMT ON 06 OCT 73  
DIGITALLY PROCESSED ON 18 NOV 74

Figure 3-24  
Chesapeake Bay - Band 6  
Linear Counts/Density Relationship

C

USA NASA ERTS 1  
06OCT73 C N38-53/W076-55 N N38-52/W076-48

SUN EL40 AZ147 190-6134 -1- 0-

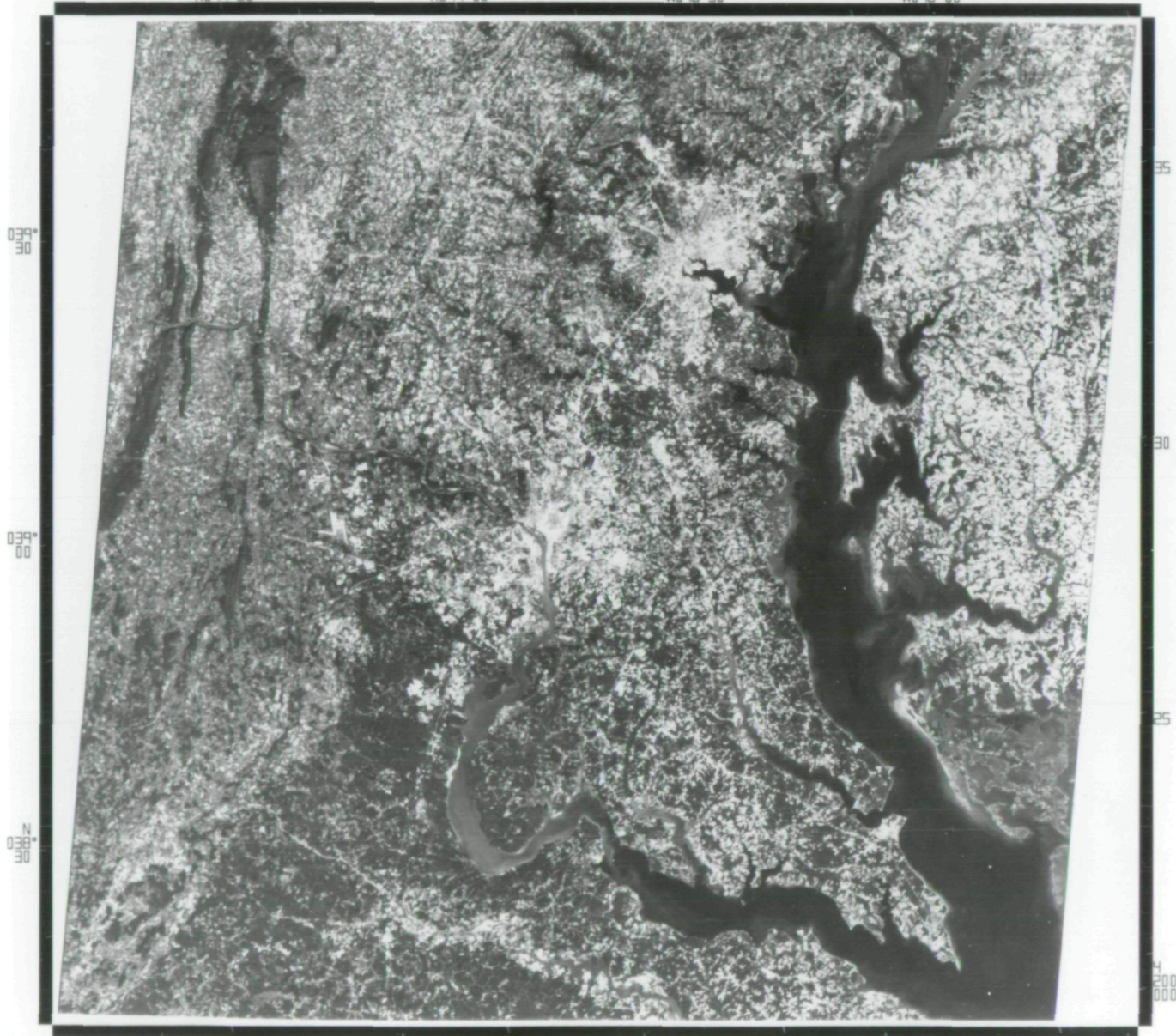
SCENE PROCESSED BY 18M  
NASA ERTS E-1440-15175- 5

W077°30

W077°00

W076°30

W076°00



FORMAT CENTER:  
UTM N4305127, E335009, 718  
GEOIDETIC N38.8814°/W076.9020°

KILOM  
ST MI



IMAGE IDENTIFICATION:  
IMAGED AT 1517 GMT ON 06 OCT 73  
DIGITALLY PROCESSED ON 14 OCT 74

Figure 3-18  
Chesapeake Bay - Band 5

D

USA NASA ERTS 1  
06 OCT 73 C N38-53/4076-55 N N38-52/4076-48

SUN EL40 AZ147 190-6134 -1- 0- NASA SCENE PROCESSED BY 18M  
NASC EPTS E-1140-15175-

4077\*30

4077\*00

4076\*30

4076\*00

139° 30'

139° 00'

N 138° 30'

35

30

25

20



250000 UTM

30

35

40

FORMAT CENTER:  
UTM N4305127, E335009, Z18  
GEODETTIC N38.8814°/4076.9020°

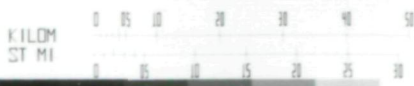


IMAGE IDENTIFICATION:  
IMAGED AT 1517 GMT ON 06 OCT 73  
DIGITALLY PROCESSED ON 14 OCT 74

Figure 3-21  
Chesapeake Bay - MSS Color Composite

E

USP NASA EPTS 1  
06OCT73 C N38-53/W076-55 N N38-52/W076-48

SUN EL40 AZ147 190-6134- -1- 0-

SCENE PROCESSED BY IBM  
NASA EPTS E-1440-15175-

W077°30

W077°00

W076°30

W076°00

39°30

39°00

N  
39°30

35

30

25

4  
200  
000



250000 UTM

30

35

40

FORMAT CENTER:  
UTM N4305127, E335009, Z18  
GEODETTIC N38.8814°/W076.9020°

KILOM  
ST MI

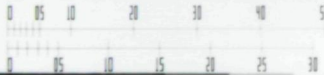


IMAGE IDENTIFICATION:  
IMAGED AT 1517 GMT ON 06 OCT 73  
DIGITALLY PROCESSED ON 14 OCT 74

Figure 3-26  
Chesapeake Bay - MSS Color Composite  
Linear Counts/Density Relationship

F

USH NGA EPTS 1  
06 OCT 73 C N38-53/W076-55 N N38-52/W076-48

SUN EL40 AZ147 190-6134- -1- 0-

SLRNF. PROCESSED BY 18M  
NAGA EPTS E-1440-15175- 5

W077°30

W077°00

W076°30

W076°00

039°30

039°00

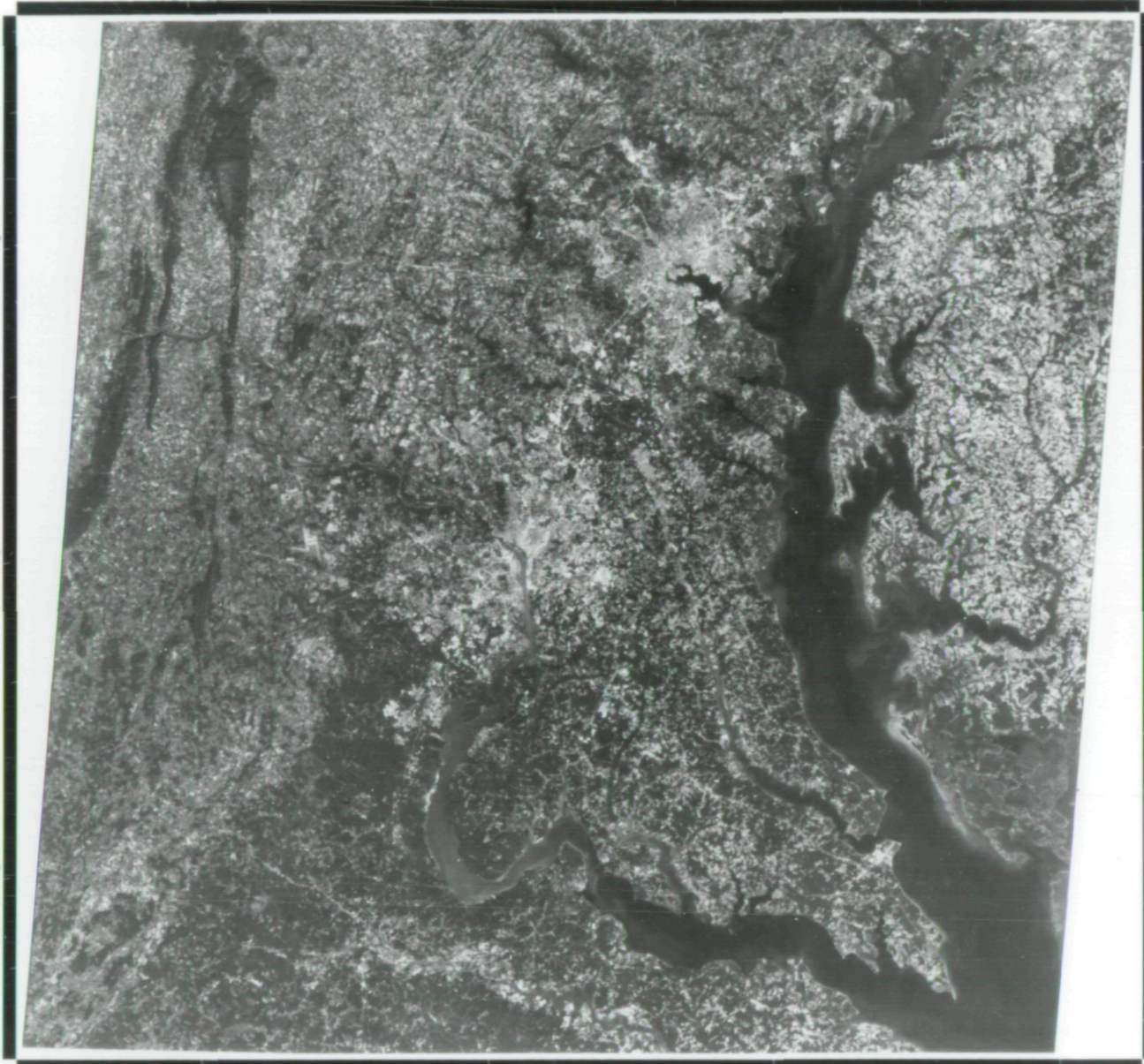
N 038°30

35

30

25

20000



250000 UTM

30

35

40

FORMAT CENTER:  
UTM N4305127. E3335000. Z18  
GEODETTIC N38.8814°/W076.9020°

KILOM  
ST MI

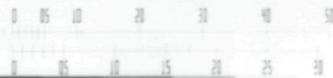


IMAGE IDENTIFICATION:  
IMAGED AT 1517 GMT ON 06 OCT 73  
DIGITALLY PROCESSED ON 14 OCT 74

Figure 3-23  
Chesapeake Bay - Band 5  
Linear Counts/Density Relationship

G

USN NASA EPTS 1  
06 OCT 73 C N38-53/4076-55 N N38-52/4076-48

SUN EL40 AZ147 190-6134- -1- 0-

SCENE PROCESSED BY 187  
NASA EPTS E-1440-15175- 6

4077°30

4077°00

4076°30

4076°00

039°30

039°00

N  
138°30

35

30

25

4  
200  
000



250000 UTM

30

35

40

FORMAT CENTER:  
UTM N4305127, E335009, Z18  
GEOIDETIC N38.8814°/4076.9020°

KILOM  
ST MI

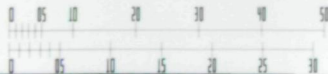


IMAGE IDENTIFICATION:  
IMAGED AT 1517 GMT ON 06 OCT 73  
DIGITALLY PROCESSED ON 18 NOV 74

Figure 3-19  
Chesapeake Bay - Band 6

H

USA NASA ERTS 1  
25 JUL 72 C N87-17/W120-56 N N87-17/W120-54

SUN EL59 AZ116 191-0028-6-1- 0-

SCENE PROCESSED BY 16M  
NASA ERTS E-1002-18134- 5

W121°30

W121°00

W120°30

W120°00

38° 00

37° 30

N 37° 00

15

10

050  
000



600000 UTM

65

70

75

FORMAT CENTER:  
UTM N4127699, E677394, Z10  
GEODEIC N37.2808°/W120.9990°

KILOM  
ST MI

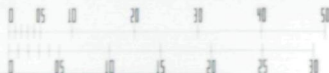


IMAGE IDENTIFICATION:  
IMAGED AT 1813 GMT ON 25 JUL 72  
DIGITALLY PROCESSED ON 04 NOV 74

Figure 3-8  
Monterey - Band 5



(a) Nearest Neighbor Assignment



(b) Bilinear Interpolation



(c) Cubic Convolution

Figure 6-12  
Composite Geometric Correction  
Enlargements of Subimage Area

USA NASA ERTS 1  
25 JUL 72 C N37-17/W120-56 N N37-17/W120-54

SUN EL59 AZ116 191-0028-6-1- 0-

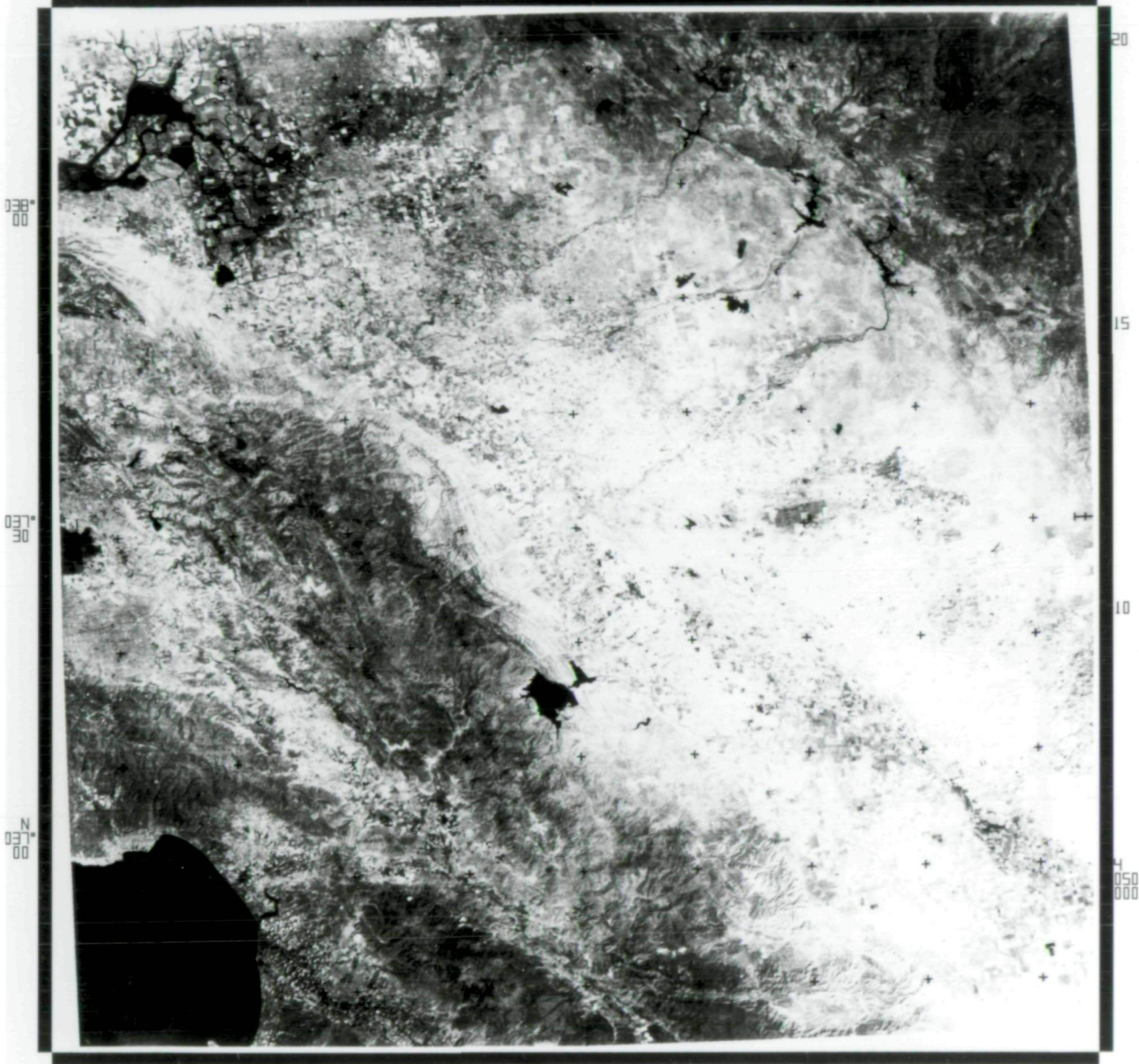
PRECISION PROCESSED BY IBM  
NASA ERTS E-1002-18134- 34

W121°30

W121°00

W120°30

W120°00



600000 UTM

65

70

FORMAT CENTER:  
UTM N4131651. E6780003. Z10  
GEODETTIC N37.3163°/W120.9912°

KILOM  
ST MI

SCALE 1:1,000,000

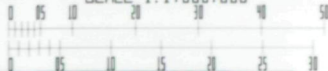


IMAGE IDENTIFICATION:  
IMAGED AT 1813 GMT ON 25 JUL 72  
DIGITALLY PROCESSED ON 04 NOV 74

Figure 3-6  
Monterey - Band 3

K

USA NASA EPTS 1  
25 JUL 72 C N37-17/W120-56 N N37-17/W120-54

SUN EL59 AZ116 191-0028-6-1- 0-

PRECISION PROCESSED BY 16M  
NASA EPTS E-1002-18134- 2 4

W121°30

W121°00

W120°30

W120°00

138° 00

137° 30

N 137° 00

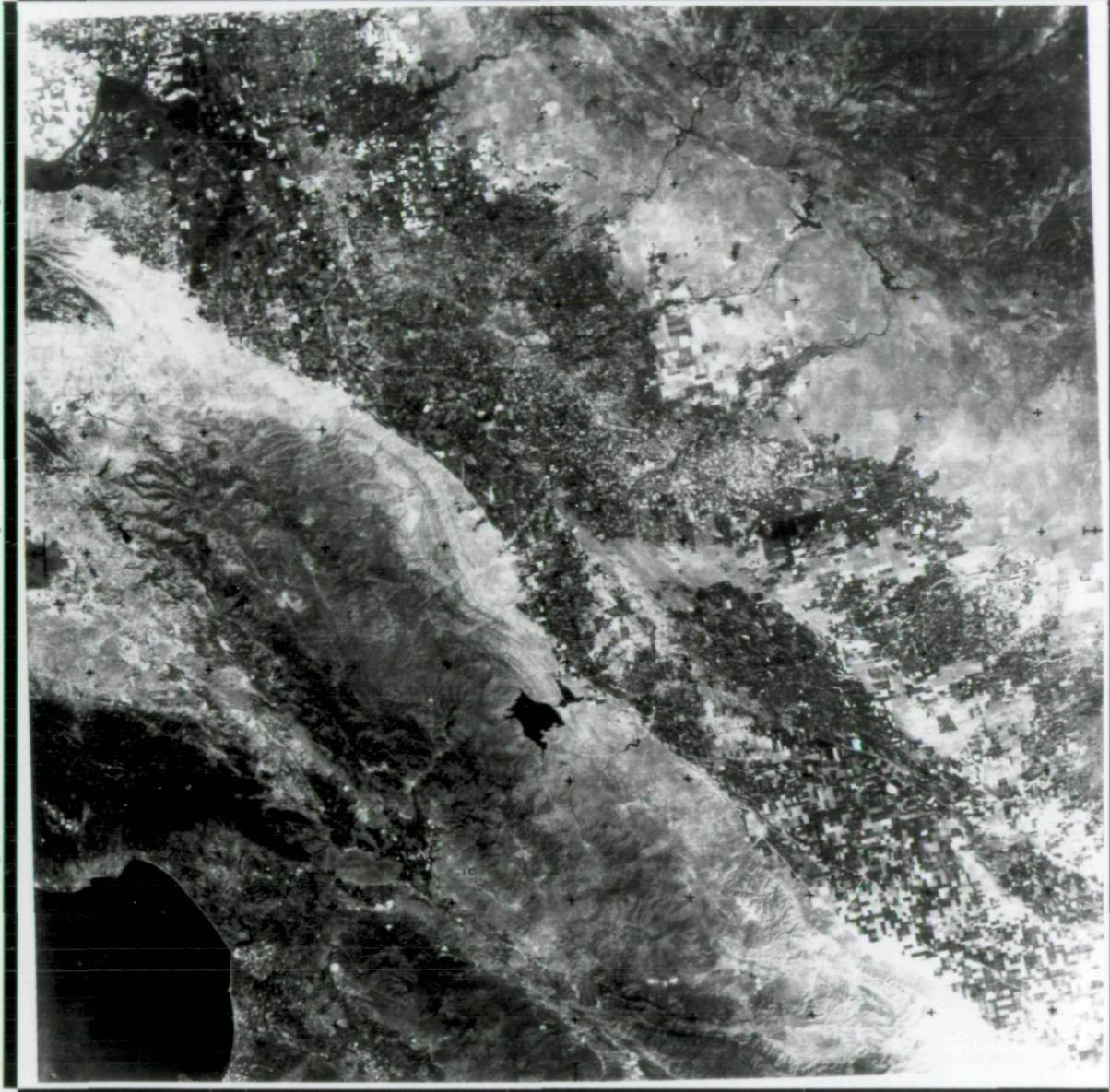
20

15

10

5

050 000



600000 UTM

65

70

FORMAT CENTER:  
UTM N4131348, E678198, Z10  
GEODETTIC N37.3135°/W120.9890°

KILOM  
ST MI

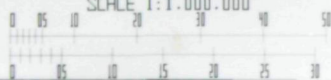


IMAGE IDENTIFICATION:  
IMAGED AT 1813 GMT ON 25 JUL 72  
DIGITALLY PROCESSED ON 04 OCT 74

Figure 3-5  
Monterey - Band 2

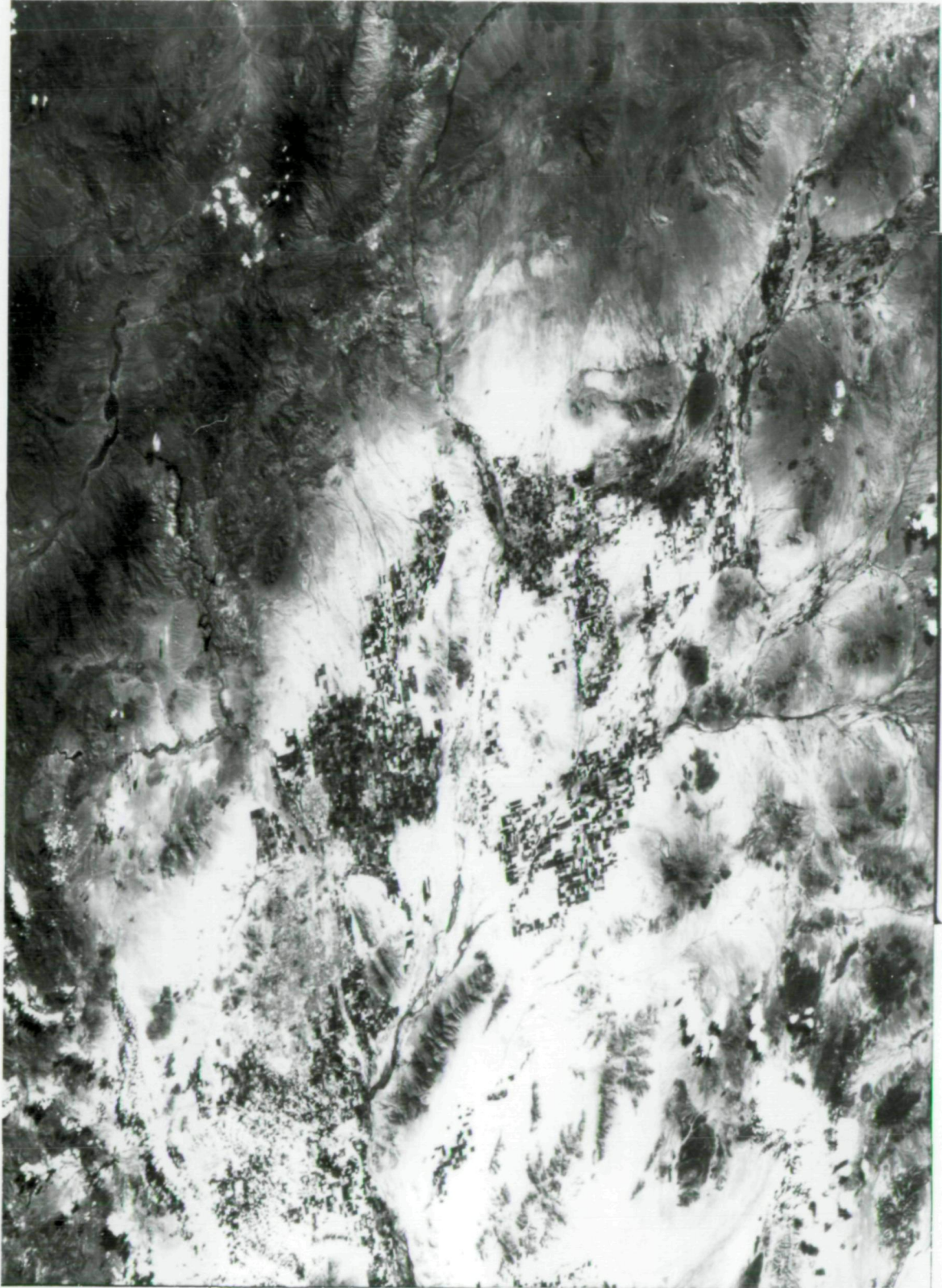


Figure 2-4  
MSS Image After  
Linear Striping Compensation

m

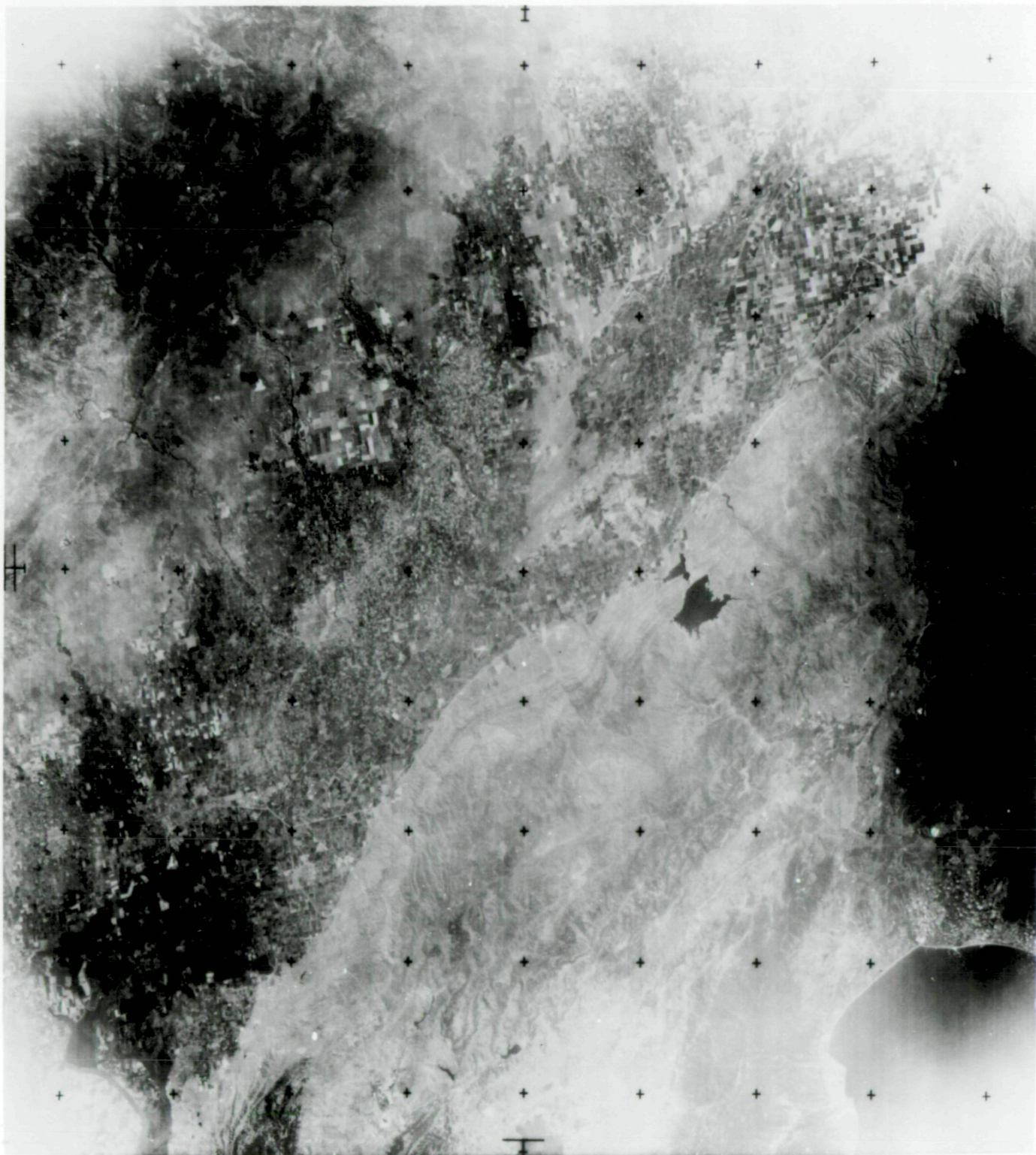
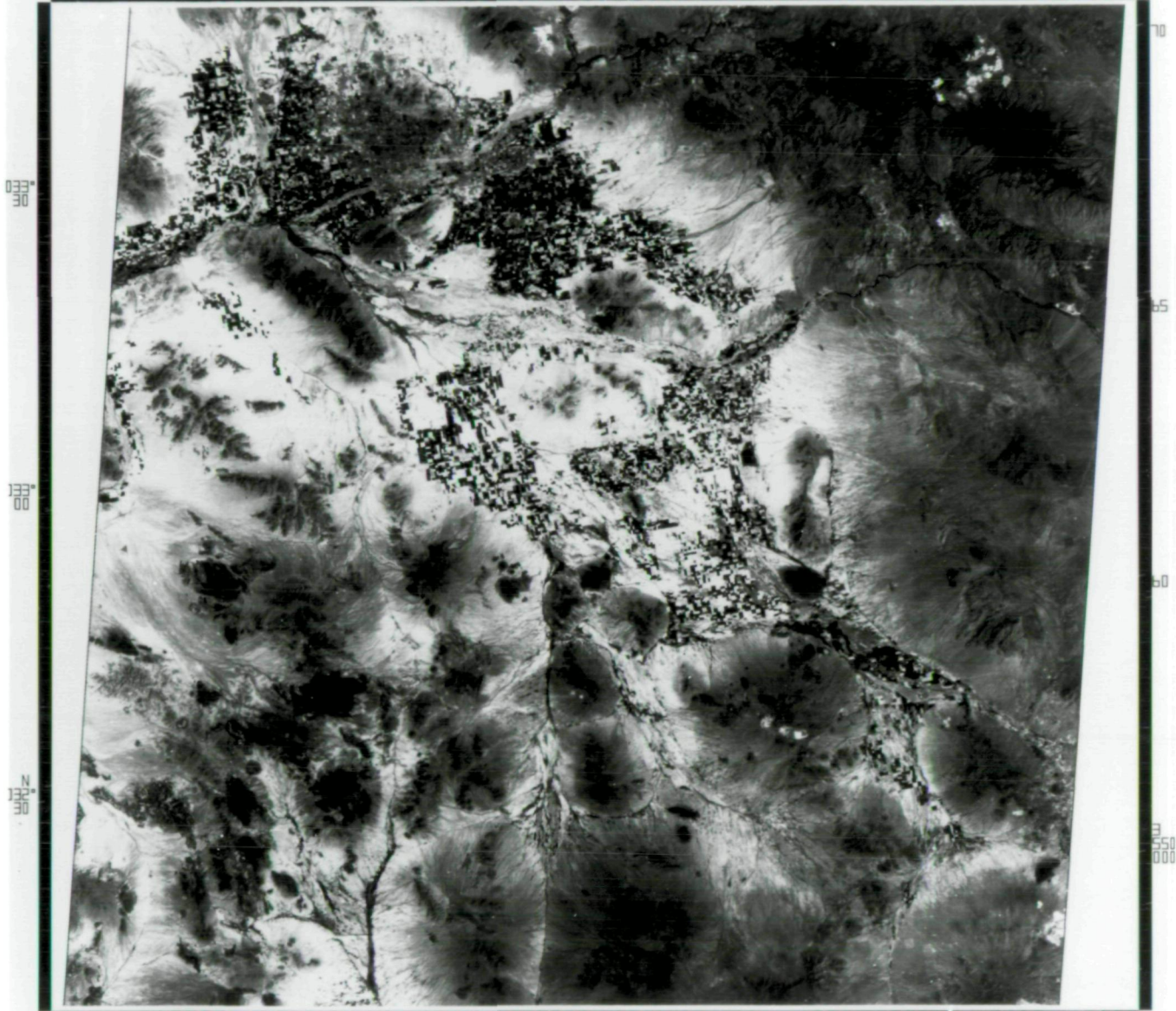


Figure 2-1  
Monterey - Band 1  
Before Radiometric Correction

N

W112°30 W112°00 W111°30 W111°00  
SUN EL55 R2122 184-0432- -1- 0- NGR EPTS E-1031-17325- 5



033° 30

033° 00

033° 30

70

65

60

550  
000

350000 UTM 40 45 50

FORMAT CENTER:  
UTM N3631900, E426017, 212  
GEODETTIC N32.8243°/W111.7903°

KILOM  
ST MI

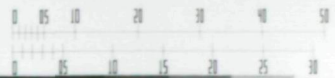


IMAGE IDENTIFICATION:  
IMAGED AT 1732 GMT ON 23 AUG 72  
DIGITALLY PROCESSED ON 04 NOV 74

Figure 3-13  
Phoenix - Band 5

USM NASA ERTS 1  
25 JUL 72 C N37-17/W120-56 N N37-17/W120-54

SUN EL59 AZ116 191-0028-6-1- 0-

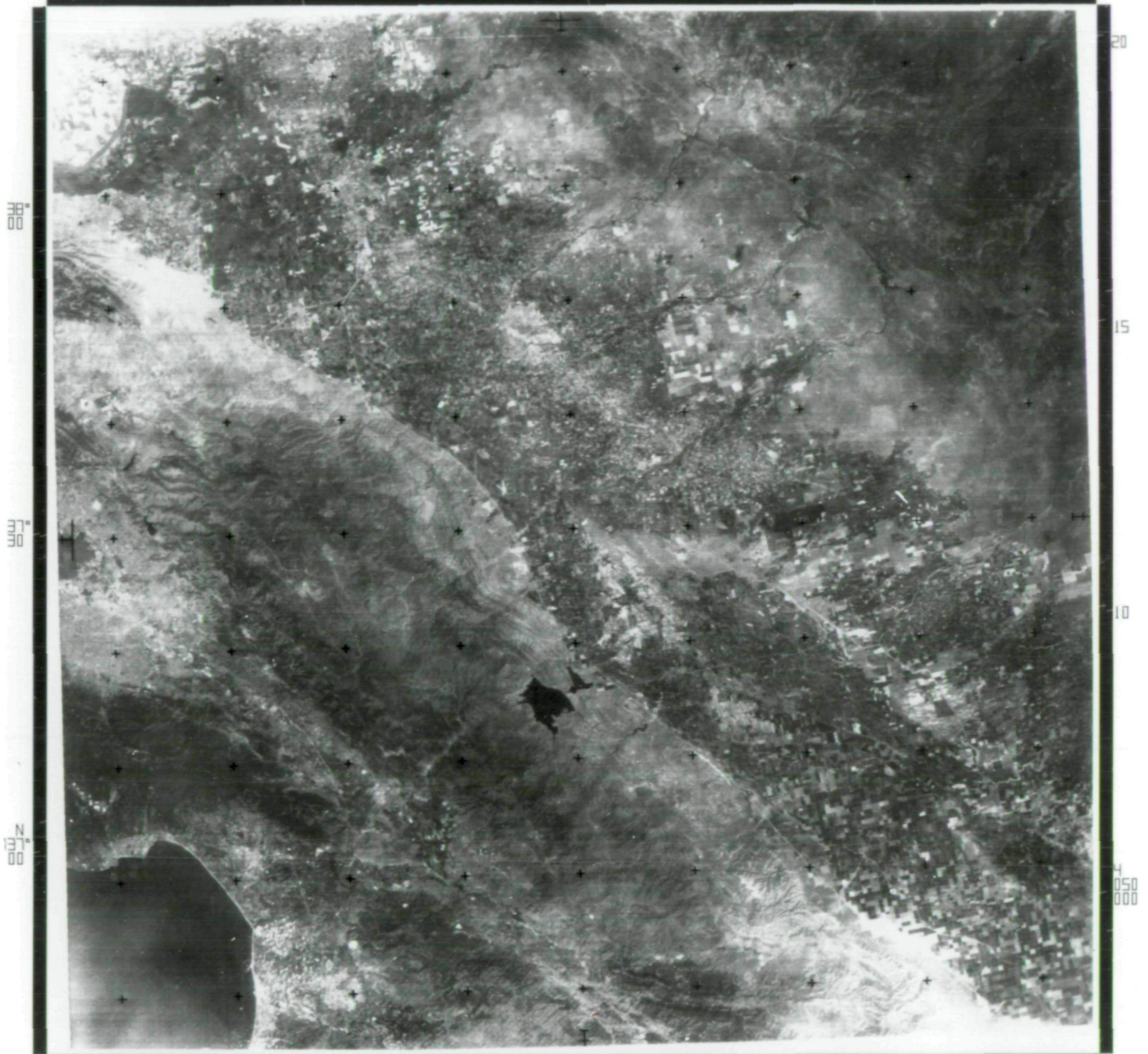
0  
PHELISSON PROCESSED BY 18M  
NASA ERTS E-1002-18134-1 4

W121°30

W121°00

W120°30

W120°00



600000 UTM

65

70

FORMAT CENTER:  
UTM N4132367, E678275, Z10  
GEODETTIC N37.3227°/W120.9879°

KILOM  
ST MI

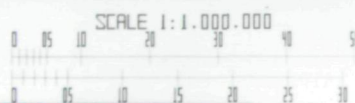


IMAGE IDENTIFICATION:  
IMAGED AT 1813 GMT ON 25 JUL 72  
DIGITALLY PROCESSED ON 04 OCT 74

Figure 3-4  
Monterey - Band 1

P

25 JUL 72 L N31-17/W120-56 N N31-17/W120-54

SUN ELSA RZ116 191-0028-6-1- 0-

NASA ERTS E-1002-18134-4

W121°30

W121°00

W120°30

W120°00

038°00

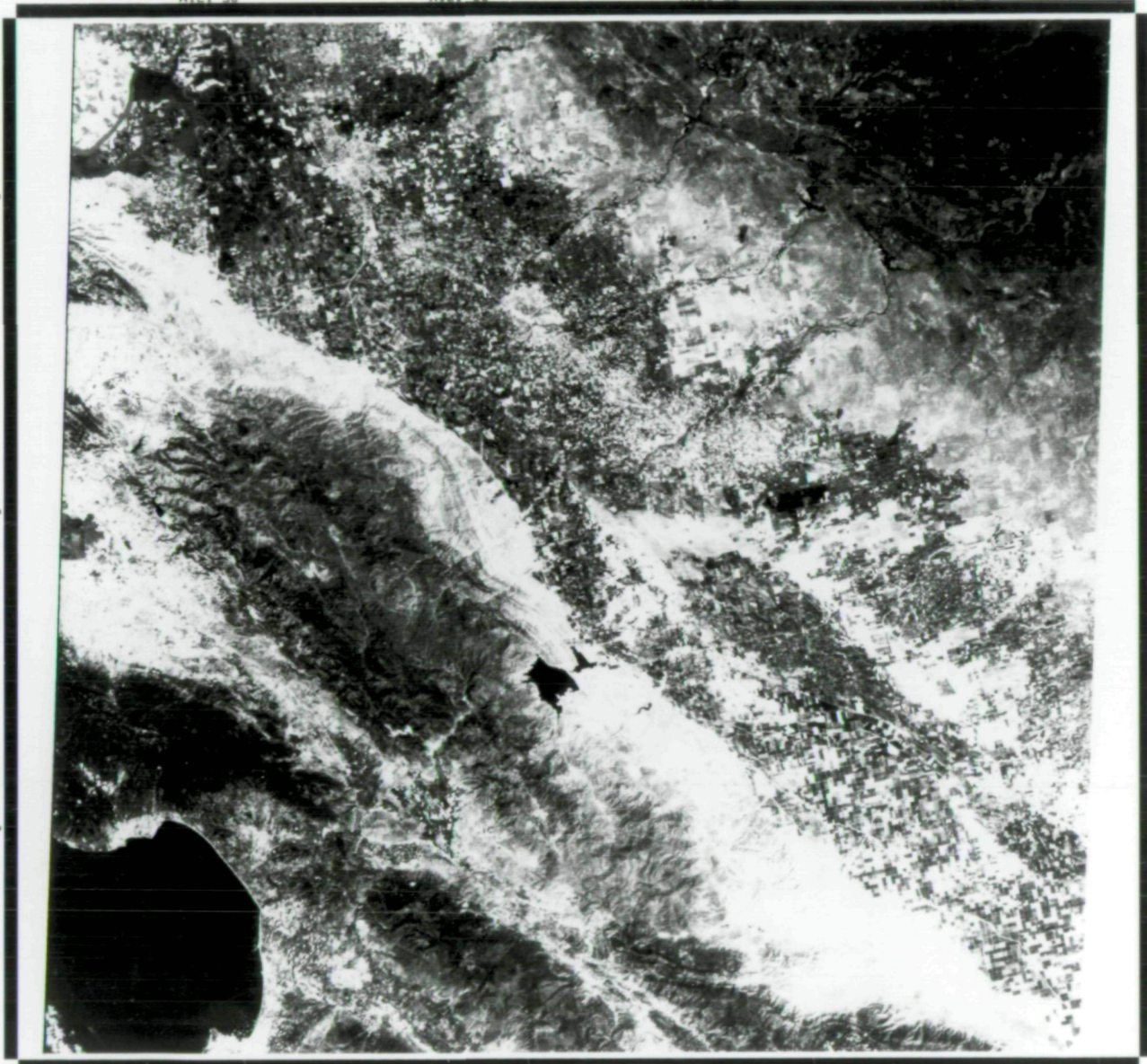
037°30

N 037°00

15

10

050 000



600000 UTM

65

70

75

FORMAT CENTER:  
 UTM N4127699, E677394, Z10  
 GEODETIC N37.2808°/W120.9990°

KILOM  
 ST MI

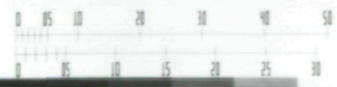


IMAGE IDENTIFICATION:  
 IMAGED AT 1813 GMT ON 25 JUL 72  
 DIGITALLY PROCESSED ON 04 NOV 74

Figure 3-7  
 Monterey - Band 4

PRECISION PROCESSED BY IBM

RESAMPLING BY CUBIC CONVOLUTION INTERPOLATION



EPTS MSS 1002-1A134 BAND 5

9

Figure 6-6  
Monterey - Band 5  
Resampled by Cubic Convolution  
No Sampling Delay Compensation

PRELIMINARY PROCESSED BY IBM

RESAMPLING BY BILINEAR INTERPOLATION WITH SAMPLE DELAY COMPENSATION



SPITS MISS 1000-10100 P0010 C

R

Figure 6-10  
Composite Geometric Correction  
Bilinear Interpolation

5

USA NASA EPTS 1  
25 JUL 72 C N37-17/W120-56 N N37-17/W120-54

SUN ELSA AZ116 191-0028-6-1- 0- NASA EPTS E-1002-18134- 109

W121°30

W121°00

W120°30

W120°00

33° 00

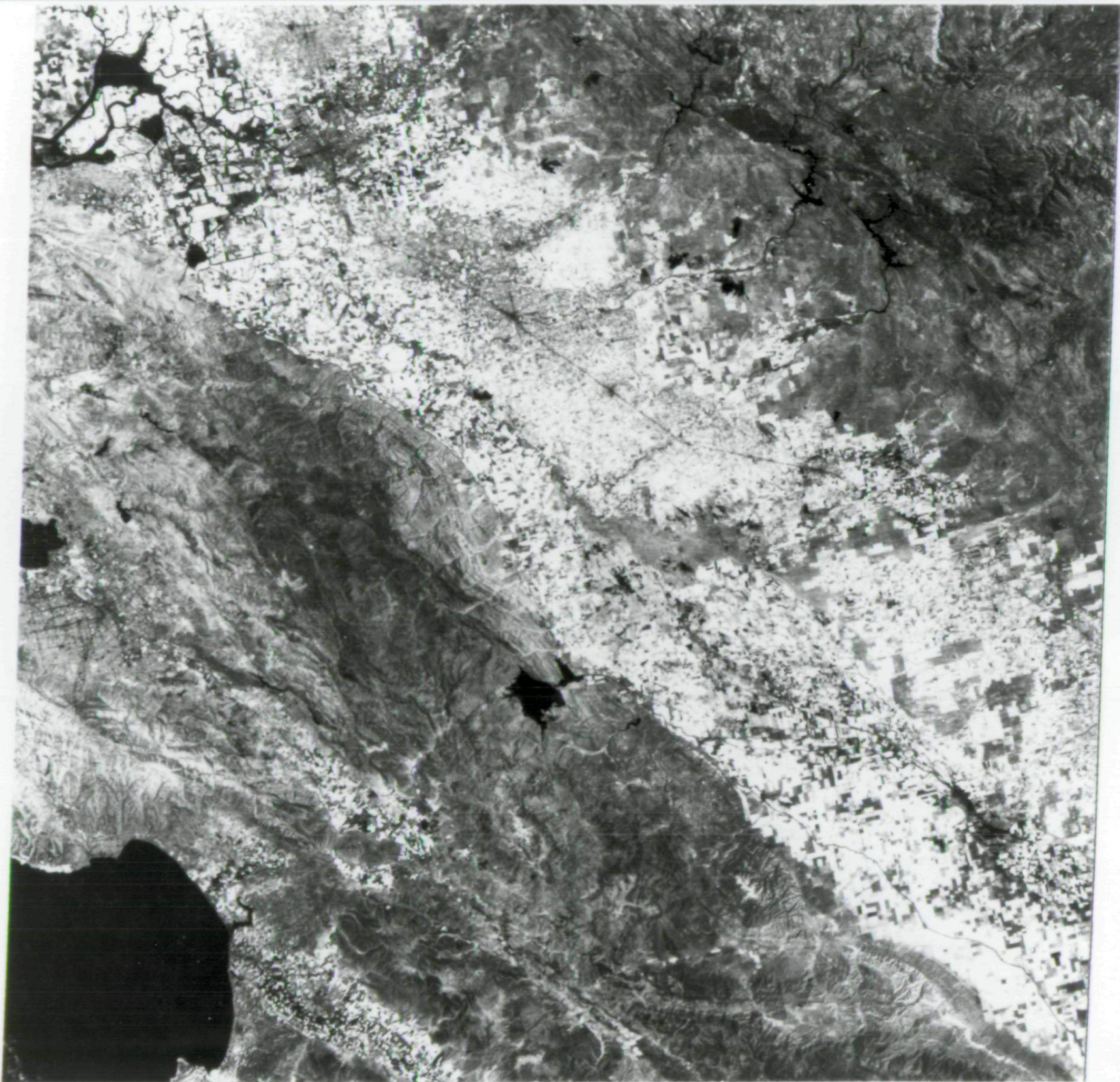
32° 30

N  
32° 00

15

10

4  
050  
000



600000 UTM

65

70

75

FORMAT CENTER:  
UTM N4127699, E677394, Z10  
GEODETTIC N37.2808°/W120.9990°

KILOM  
ST MI

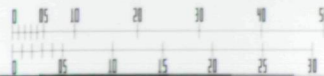


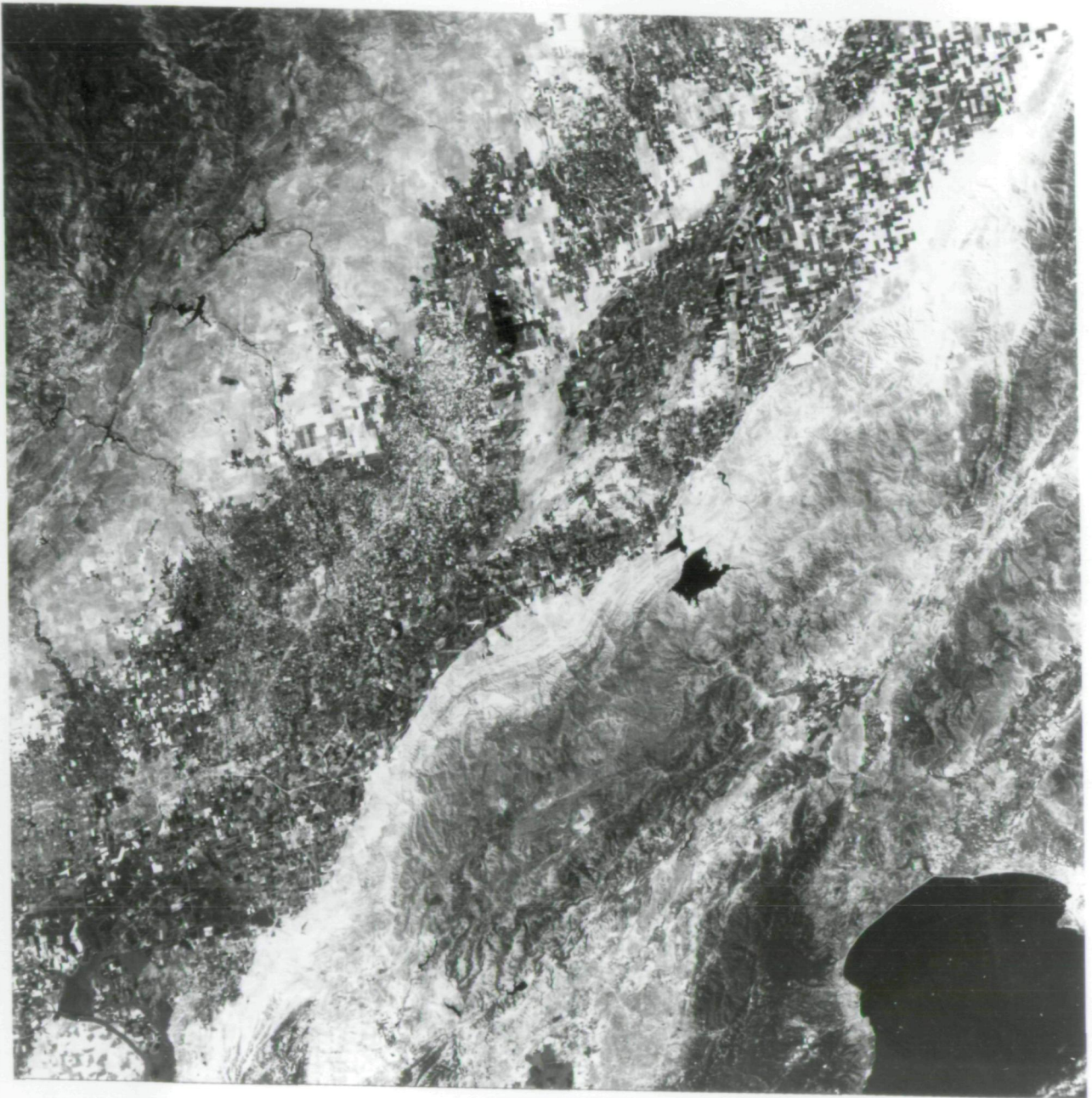
IMAGE IDENTIFICATION:  
IMAGED AT 1813 GMT ON 25 JUL 72  
DIGITALLY PROCESSED ON 04 NOV 74

Figure 3-10  
Monterey - Band 7

T

PRECISION PROCESSED BY IBM

RESAMPLING BY CUBIC CONVOLUTION INTERPOLATION WITH SAMPLE DELAY COMPENSATION



FPTS. MSS. 1002-18134 RANO 5

Figure 6-11  
Composite Geometric Correction  
Cubic Convolution

2

25 JUL 72 C N37-17/W120-56 N N37-17/W120-54

SUN ELS9 AZ116 191-0028-6-1- 0-

SCENE PROCESSED BY 16M  
NPOA EPTS E-1002-18134-

W121°30

W121°00

W120°30

W120°00

138°00

137°30

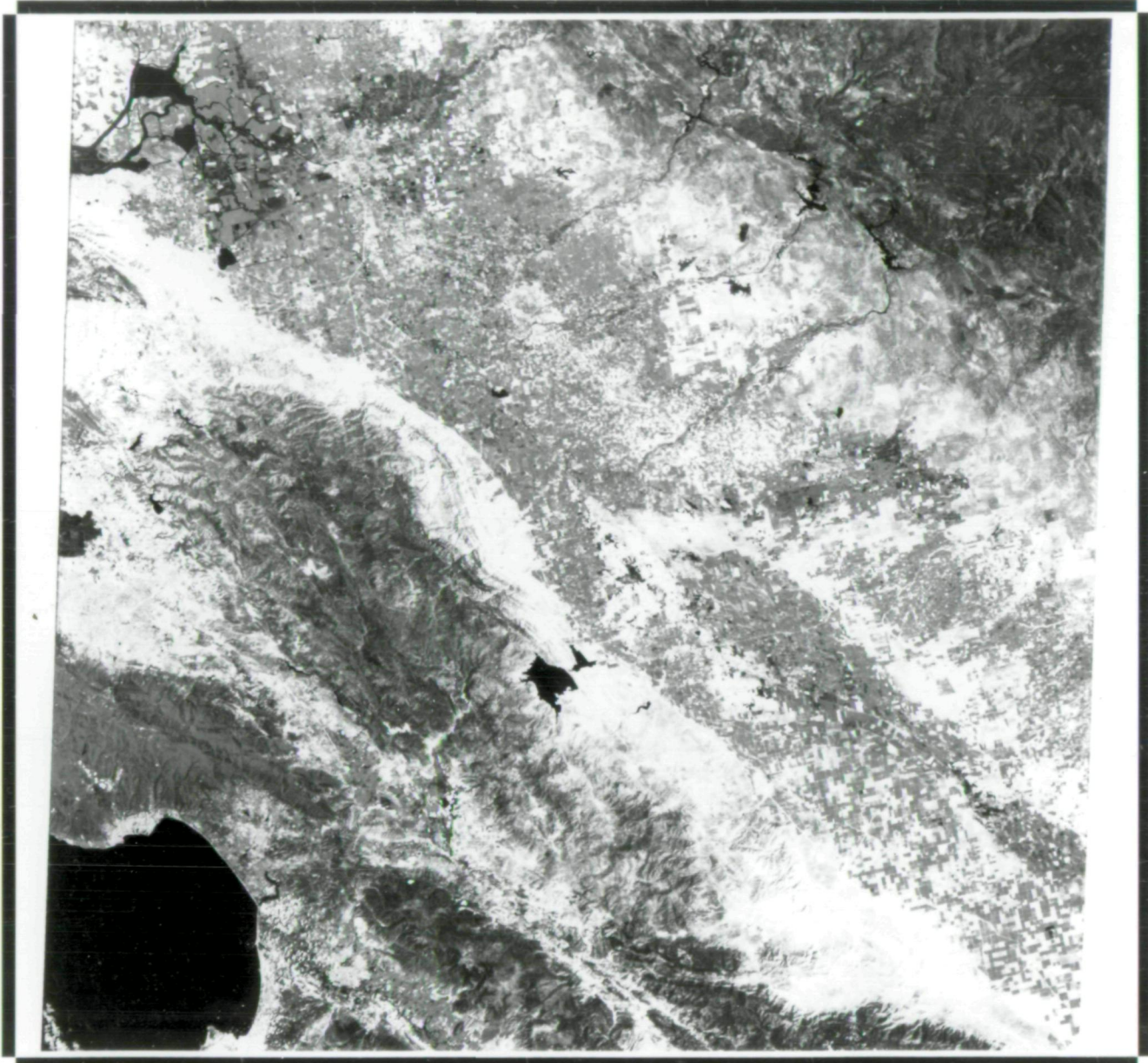
137°00

15

10

4

050  
000



600000 UTM

65

70

75

FORMAT CENTER:  
UTM N4127699, E677394, Z10  
GEODETTIC N37.2808°/W120.9990°

KILOM  
ST MI



IMAGE IDENTIFICATION:  
IMAGED AT 1813 GMT ON 25 JUL 72  
DIGITALLY PROCESSED ON 04 NOV 74

Figure 3-11

Monterey - MSS Color Composite

USA NASA EPTS 1  
25 JUL 72 C N37-17/W120-56 N N37-17/W120-54

SUN ELSA RZ116 191-0028-6-1- 0-

SCENE PROCESSED BY IBM  
NASA EPTS E-1002-18134-6

W121°30

W121°00

W120°30

W120°00

138°  
00

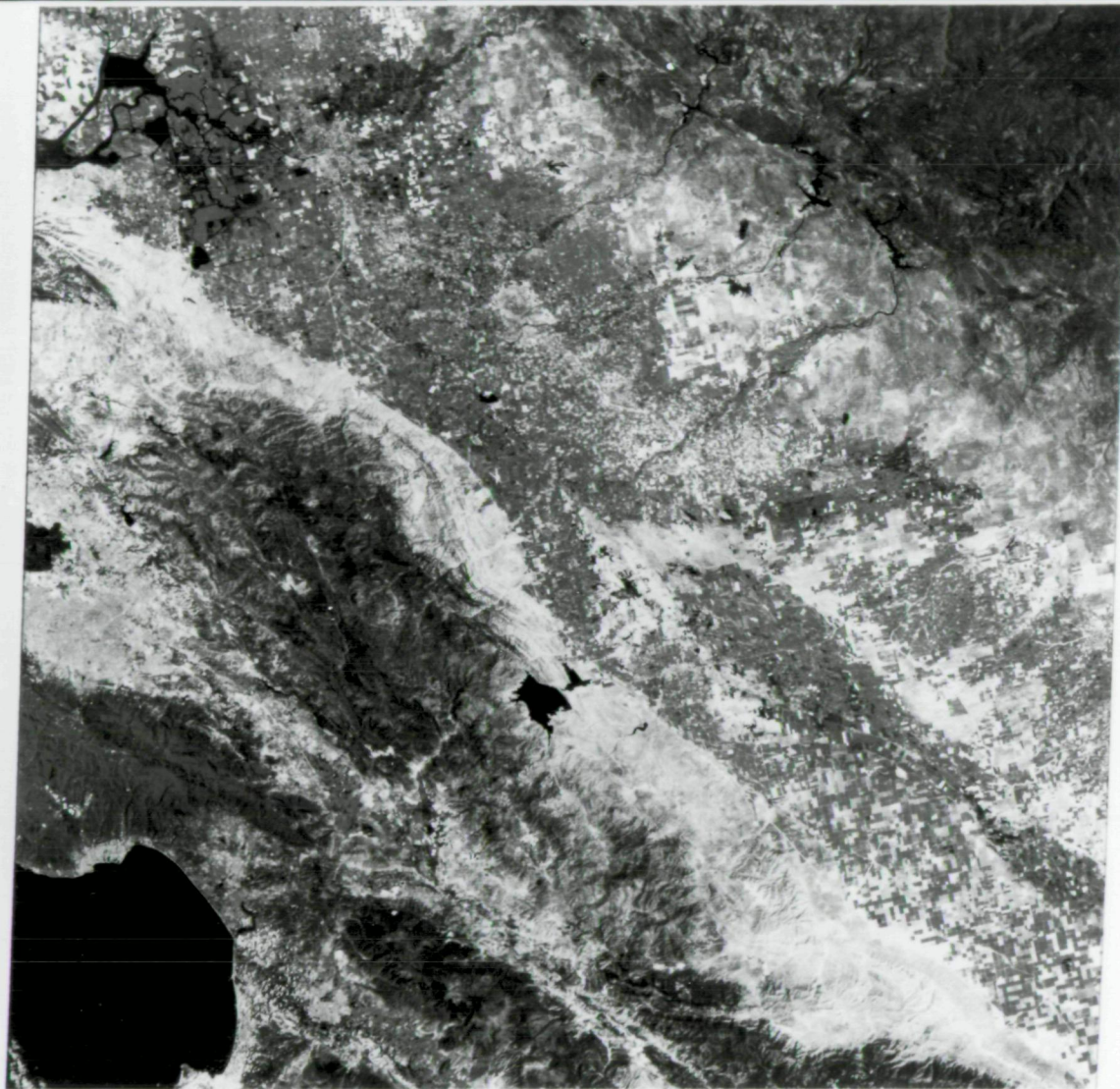
137°  
30

N  
037°  
00

15

10

050  
000



600000 UTM

65

10

15

FORMAT CENTER:  
UTM N4127699, 6677394, Z10  
GEODETTIC N37.2808°/W120.9990°

KILOM  
ST M1

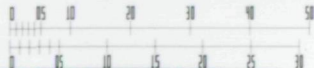


IMAGE IDENTIFICATION:  
IMAGED AT 1813 GMT ON 25 JUL 72  
DIGITALLY PROCESSED ON 04 NOV 74

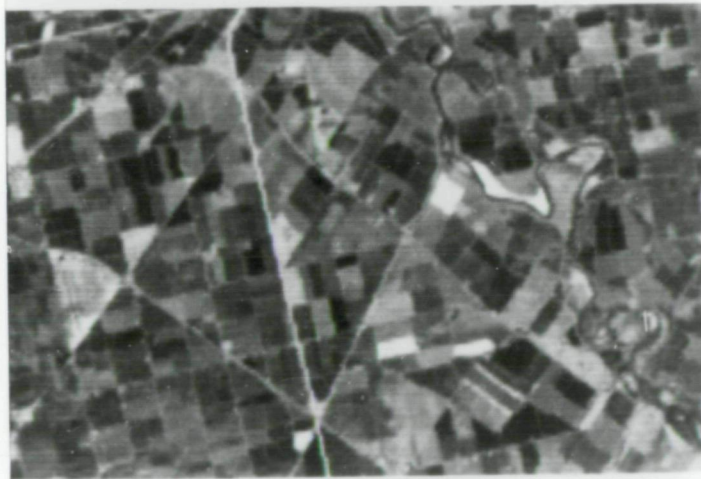
Figure 3-11  
Monterey - MSS Color Composite

W

(a) Nearest Neighbor Assignment



(b) Bilinear Interpolation



(c) Cubic Convolution



Figure 6-7

USA NASA ERTS 1  
06 OCT 73 C N38-53/W076-55 N N38-52/W076-48

SUN EL40 AZ147 190-6134 -1- 0- NASA ERTS E-1440-15175-7

SCENE PROCESSED BY IBM

W077°30

W077°00

W076°30

W076°00

039°30

039°00

N  
038°30

35

30

25

200  
000

250000 UTM

30

35

40

FORMAT CENTER:  
UTM N4305127. E335009. Z18  
GEODETTIC N38.8814/W076.9020

KILOM  
ST MI

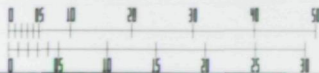


IMAGE IDENTIFICATION:  
IMAGED AT 1517 GMT ON 06 OCT 73  
DIGITALLY PROCESSED ON 14 OCT 74

Figure 3-25  
Chesapeake Bay - Band 7  
Linear Counts/Density Relationship

USC NHCS EPTS 1  
06OCT73 C N38-53/W076-55 N N38-52/W076-48

SUN EL40 AZ147 190-6134 -1- 0-

SCENE PROCESSED BY IBM  
NASC EPTS E-1440-15175- 7

W077°30

W077°00

W076°30

W076°00

039°30

039°00

N  
038°30

35

30

25

4  
200  
000



250000 UTM

30

35

40

FORMAT CENTER:  
UTM N4305127, E335009, Z18  
GEODETTIC N38.8814°/W076.9020°

KILOM  
ST MI



IMAGE IDENTIFICATION:  
IMAGED AT 1517 GMT ON 06 OCT 73  
DIGITALLY PROCESSED ON 14 OCT 74

Figure 3-20  
Chesapeake Bay - Band 7

2

WSP NASA ERTS 1  
06 OCT 73 C N38-53/W076-55 N N38-52/W076-48

SUN EL40 AZ147 190-6134- -1- 0-

SLER MAJLESSEU BT 187  
NASA ERTS E-1440-15175-4

W077°30

W077°00

W076°30

W076°00

039°30

039°00

N  
038°30

35

30

25

200  
000



250000 UTM

30

35

40

FORMAT CENTER:  
UTM N4305127, E335009, Z18  
GEODETTIC N38.8814°/W076.9020°

KILOM  
ST MI

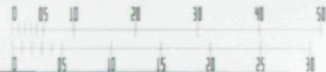


IMAGE IDENTIFICATION:  
IMAGED AT 1517 GMT ON 06 OCT 73  
DIGITALLY PROCESSED ON 14 OCT 74

Figure 3-17  
Chesapeake Bay - Band 4

Z2

US4 NASA EPTS 1  
06OCT73 C N38-53/W076-55 N N38-52/W076-48

SUN EL40 AZ147 190-6134- -1- 0- NASA EPTS E-1440-15175-4

W077°30

W077°00

W076°30

W076°00



FORMAT CENTER:  
UTM N4305127. E335009. Z18  
GEODETTIC N38.8814°/W076.9020°



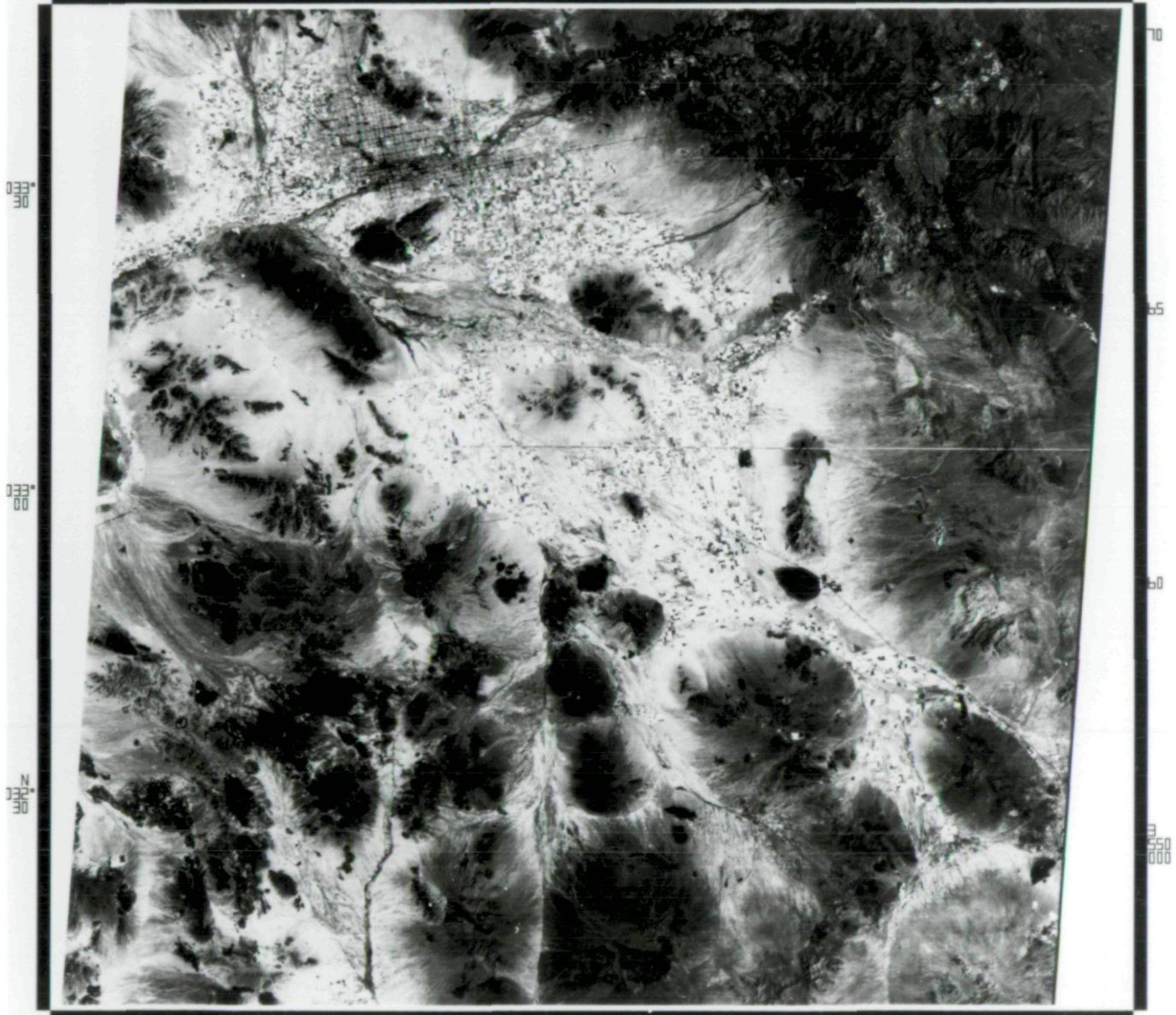
IMAGE IDENTIFICATION:  
IMAGED AT 1517 GMT ON 06 OCT 73  
DIGITALLY PROCESSED ON 14 OCT 74

Figure 3-22  
Chesapeake Bay - Band 4  
Linear Counts/Density Relationship

ZB

USA NASA EPTS 1  
23 AUG 72 C N32-53/W111-48 N N32-51/W111-39  
H112°30 W111°00

SUN EL55 AZ122 189-0432 -1- 0- NASA EPTS E-1031-17325-  
H111°30 W111°00



350000 UTM

40

45

50

FORMAT CENTER:  
UTM N3631900, E426017, Z12  
GEODETTIC N32.8243°/W111.7403°

KILOM  
ST MI

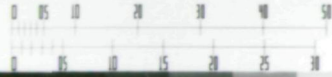


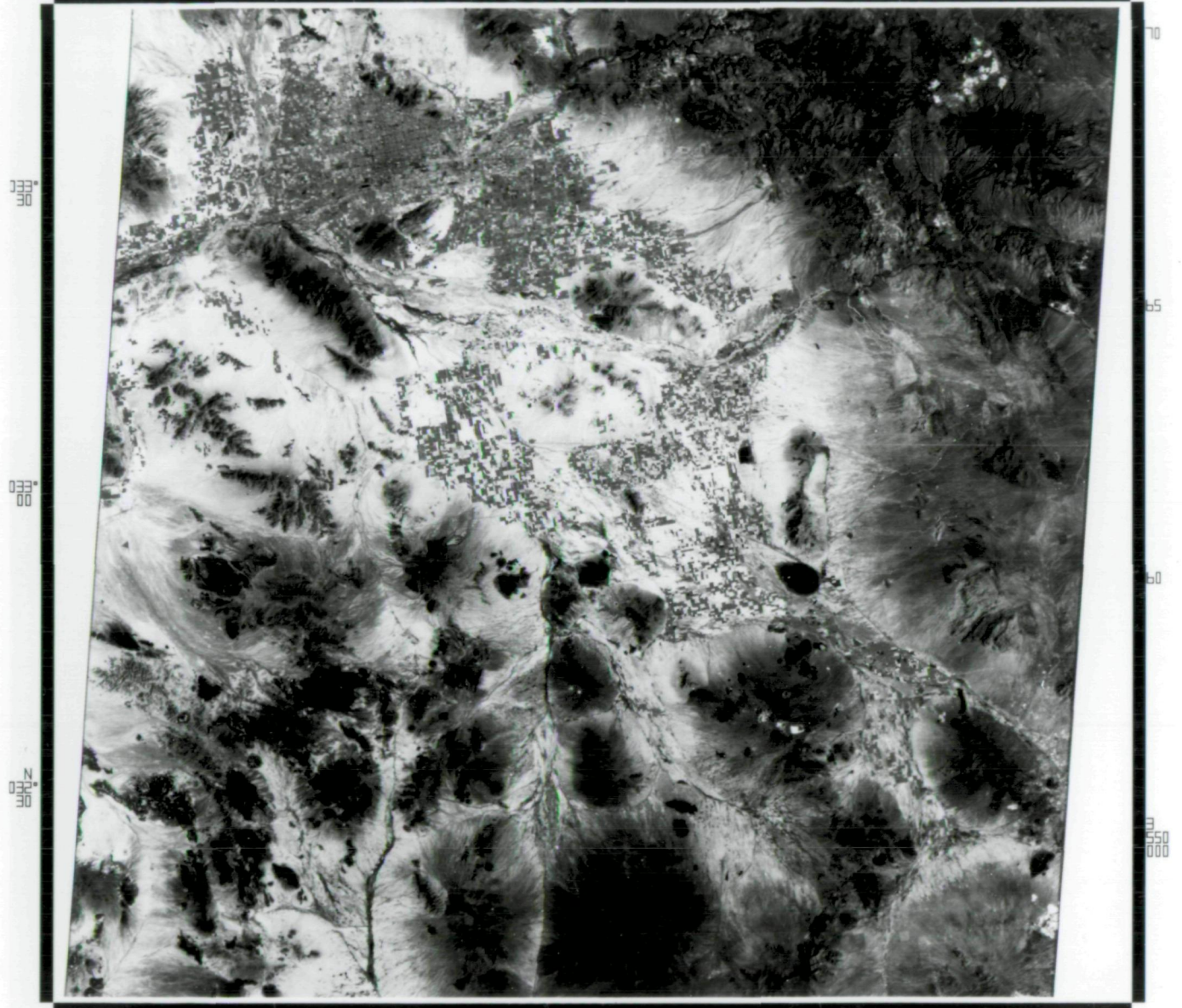
IMAGE IDENTIFICATION:  
IMAGED AT 1732 GMT ON 23 AUG 72  
DIGITALLY PROCESSED ON 06 NOV 74

Figure 3-15  
Phoenix - Band 7

ZC

USC NPOC EPTS 1  
23AUG72 C N32-53/W111-48 N N32-51/W111-39  
W112°30 W112°00 W111°30 W111°00

SUN EL55 AZ122 189-0432- -1- 0-  
SCENE PROCESSED BY 16M  
NACA EPTS E-1031-17325-5



FORMAT CENTER:  
UTM N3631900, E426017, Z12  
GEODETTIC N32.8243°/W111.7903°

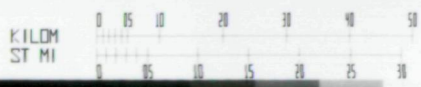


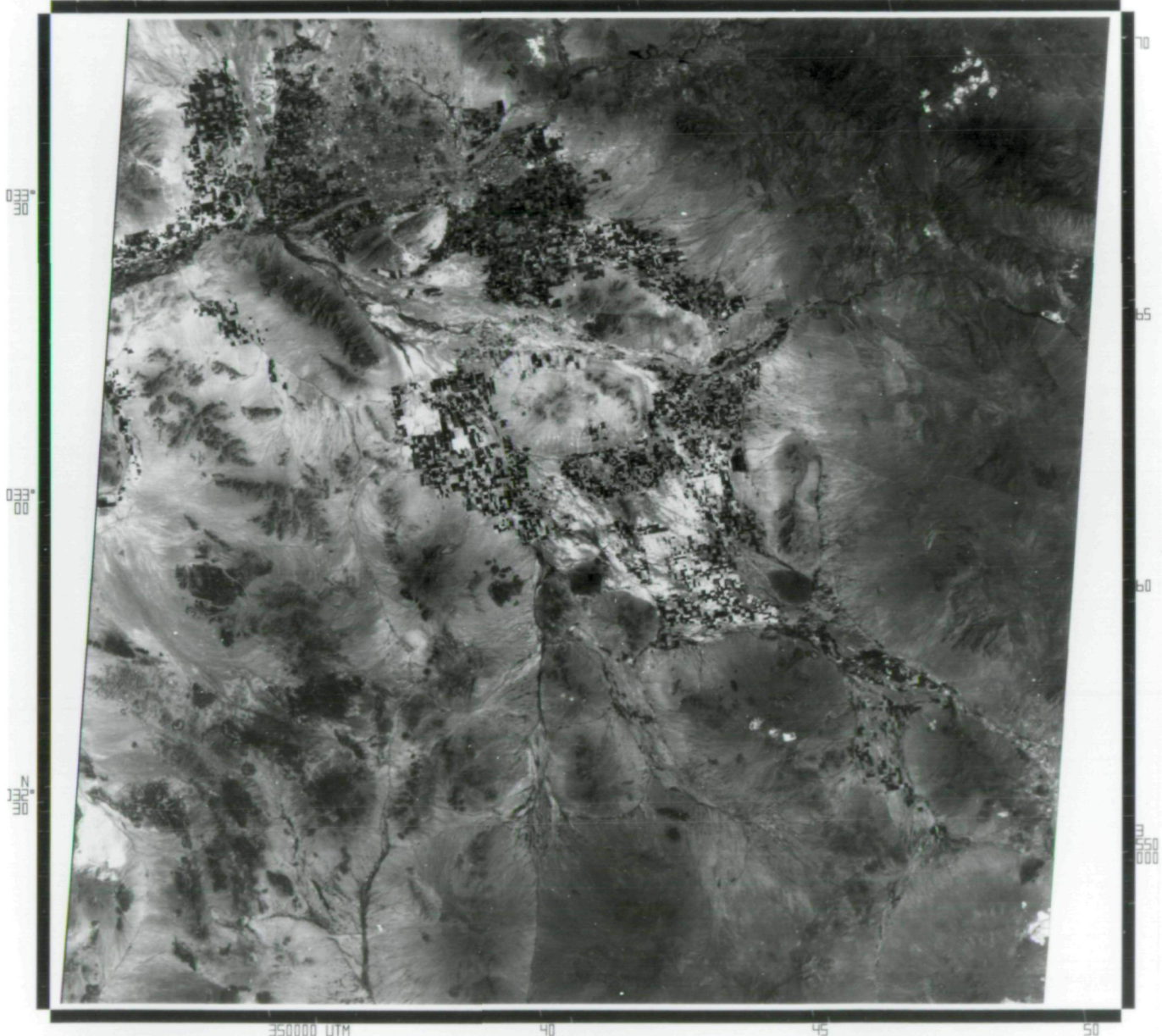
IMAGE IDENTIFICATION:  
IMAGED AT 1732 GMT ON 23 AUG 72  
DIGITALLY PROCESSED ON 04 NOV 74

Figure 3-16  
Phoenix - MSS Color Composite

3d

USC NPSA EPTS 1  
23AUG72 C N32-53/W111-48 N N32-51/W111-39  
W112°30 W112°00

SUN EL55 AZ122 189-0432- -1- 0- SCENE PROCESSED BY 18M  
NACA EPTS E-1031-17325-4 W111°30 W111°00



FORMAT CENTER:  
UTM N3631900, E426017, Z12  
GEODETTIC N32.8248°/W111.7903°

KILOM  
ST MI



IMAGE IDENTIFICATION:  
IMAGED AT 1732 GMT ON 23 AUG 72  
DIGITALLY PROCESSED ON 04 NOV 74

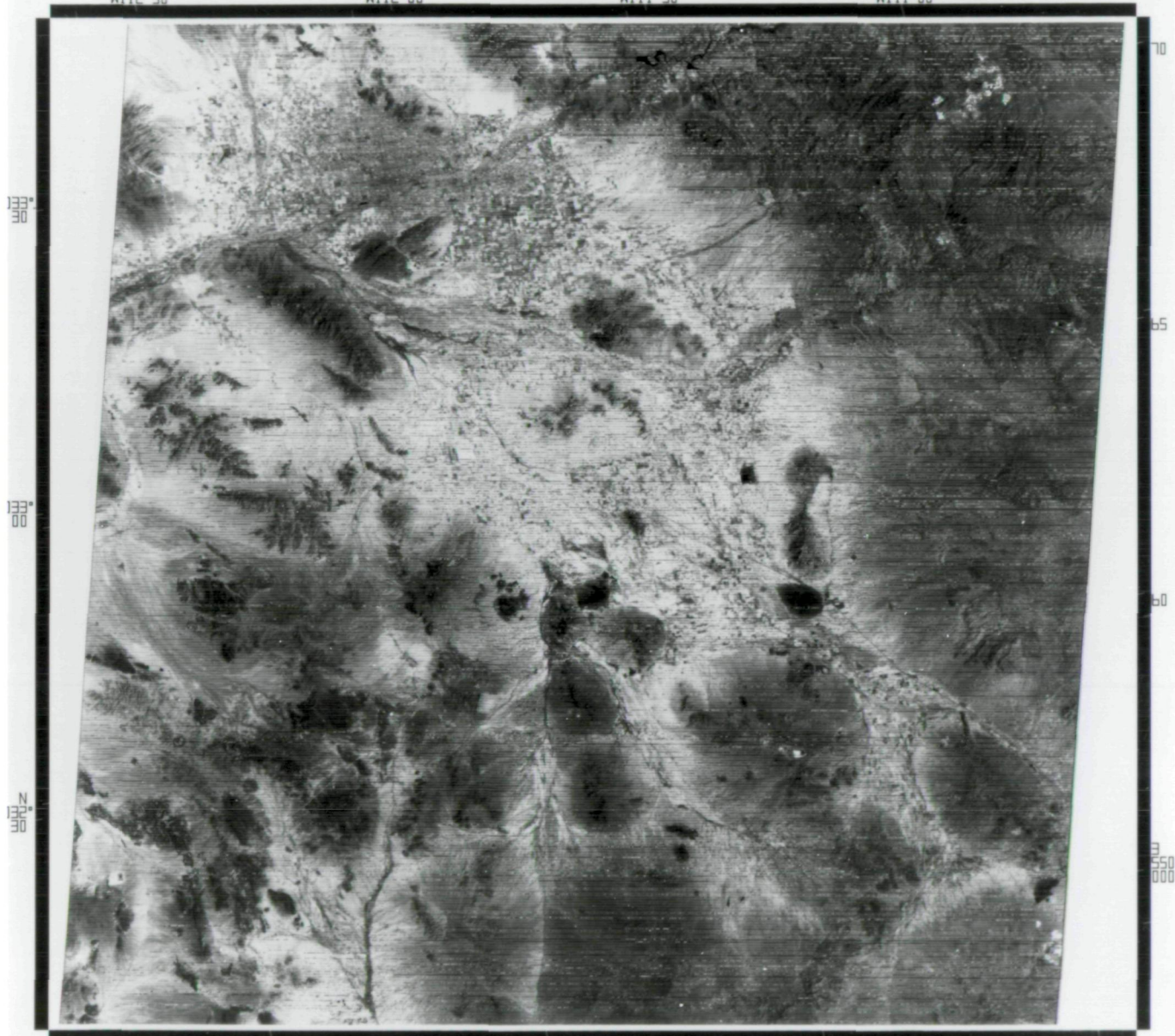
Figure 3-12  
Phoenix - Band 4

Ze

USA NASA ERTS 1  
25 AUG 72 C N32-53/W111-48 N N32-51/W111-39  
W112°30' 00" W111°30' 00"

SUN EL55 AZ122 189-0432- -1- 0-

SCENE PROCESSED BY IBM  
NASA ERTS E-1031-17325- 6  
W111°00'



350000 UTM

40

45

50

FORMAT CENTER:  
UTM N3631900, E426017, Z12  
GEODETTIC N32.8243°/W111.7903°

KILOM  
ST MI

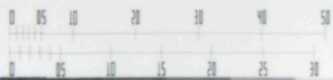


IMAGE IDENTIFICATION:  
IMAGED AT 1732 GMT ON 23 AUG 72  
DIGITALLY PROCESSED ON 19 NOV 74

Figure 3-14  
Phoenix - Band 6

ZF

U.S. NAVAL ERTS-1  
25 JUL 72 C N37-17/W120-56 N N37-17/W120-54

SUN EL59 AZ116 191-0028-6-1- 0- NAESA ERTS E-1002-18134-  
SCENE PROCESSED BY 167

W121°30

W121°00

W120°30

W120°00

38° 00

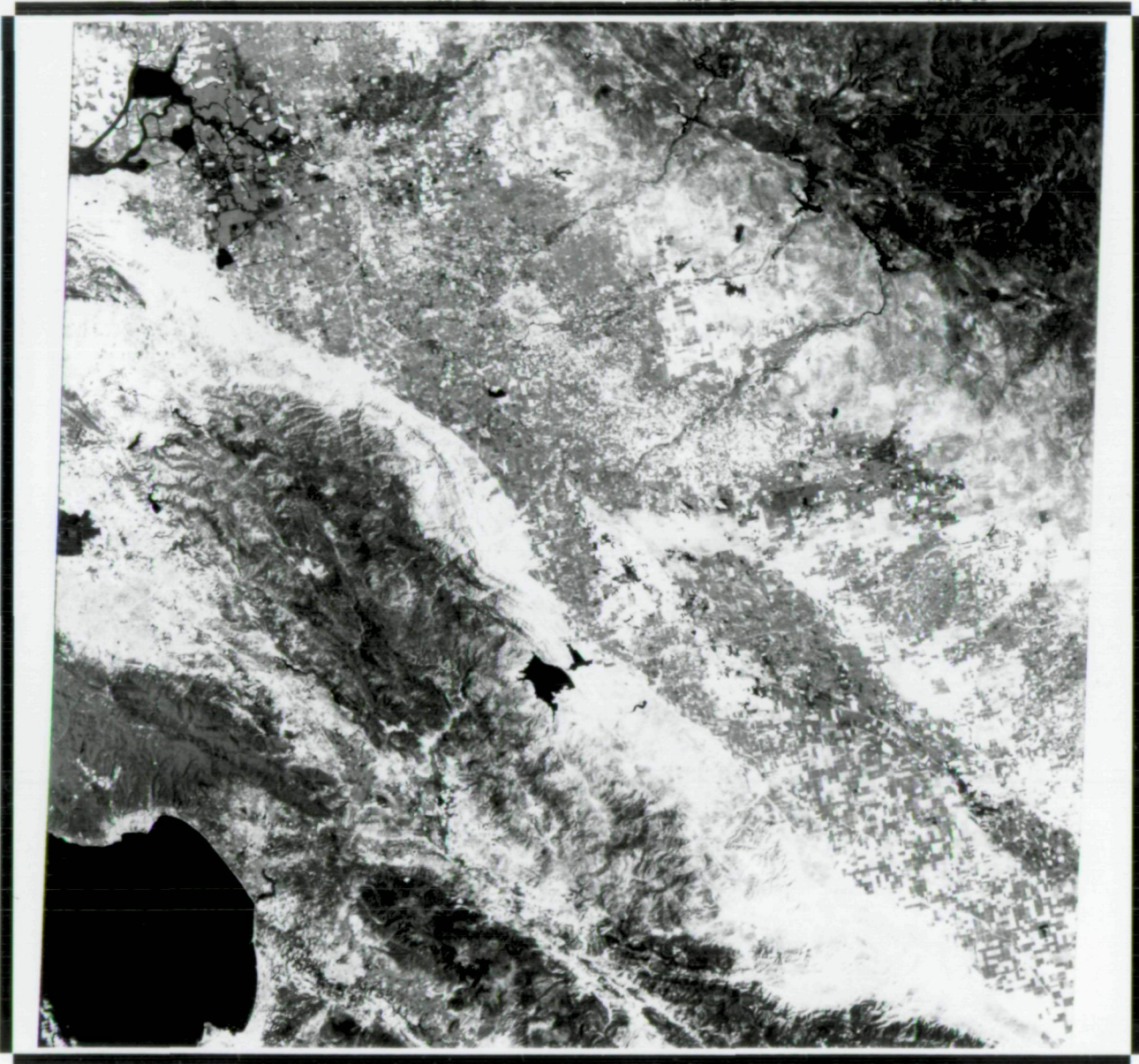
37° 30

N 37° 10

15

10

050  
000



600000 UTM

65

70

75

FORMAT CENTER:  
UTM N4127699, E677394, Z10  
GEODETTIC N37.28087/W120.9990°

KILOM  
ST MI

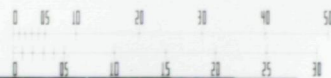


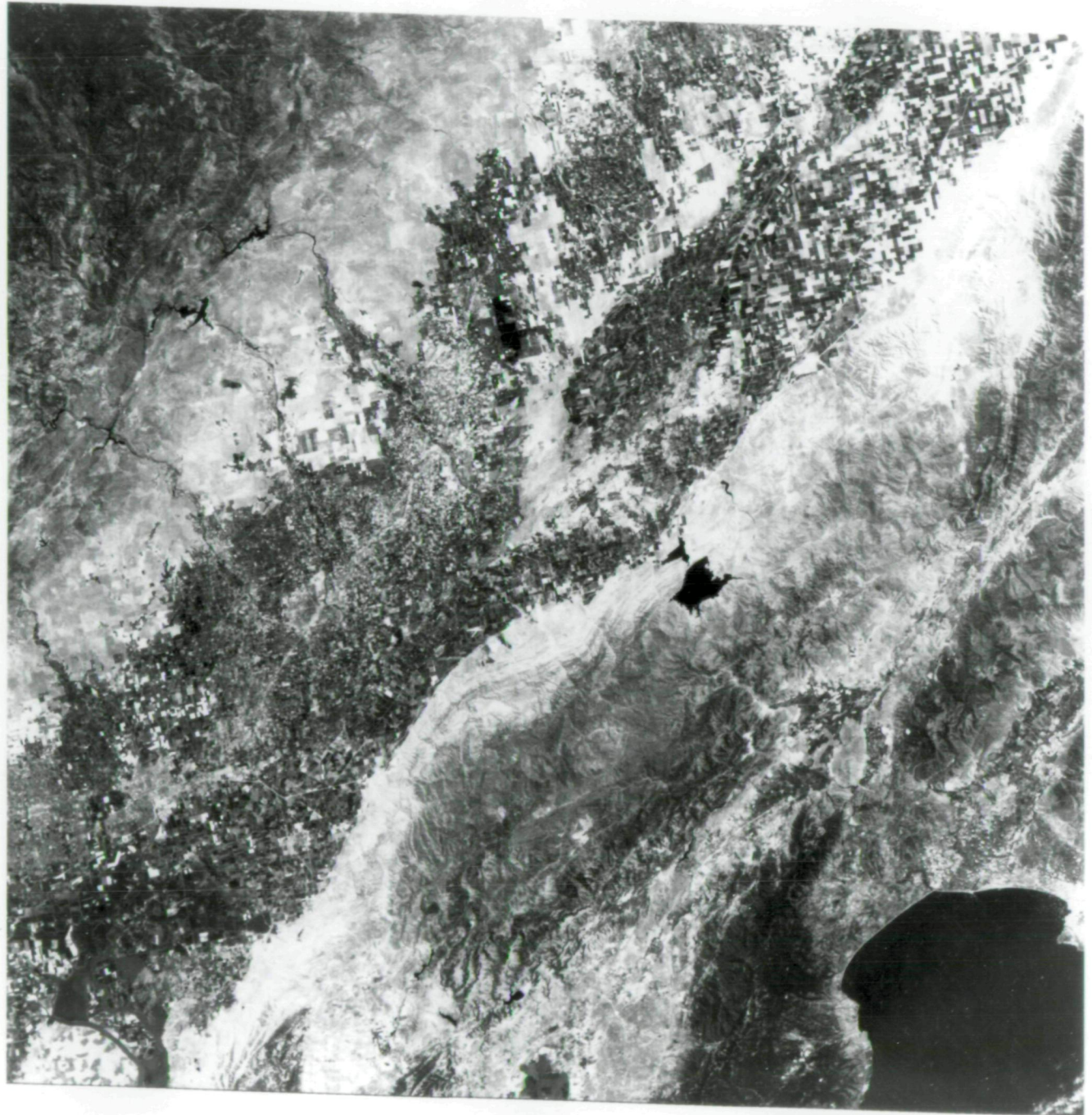
IMAGE IDENTIFICATION:  
IMAGED AT 1813 GMT ON 25 JUL 72  
DIGITALLY PROCESSED ON 04 NOV 74



Figure 3-11  
Monterey - MSS Color Composite

Zg

PRECISION PROCESSED BY IBM



EPIC MSC 1002-10134 BAND 5

RESAMPLING BY BILINEAR INTERPOLATION

Figure 6-5  
Monterey - Band 5  
Resampled by Bilinear Interpolation  
No Sampling Delay Compensation



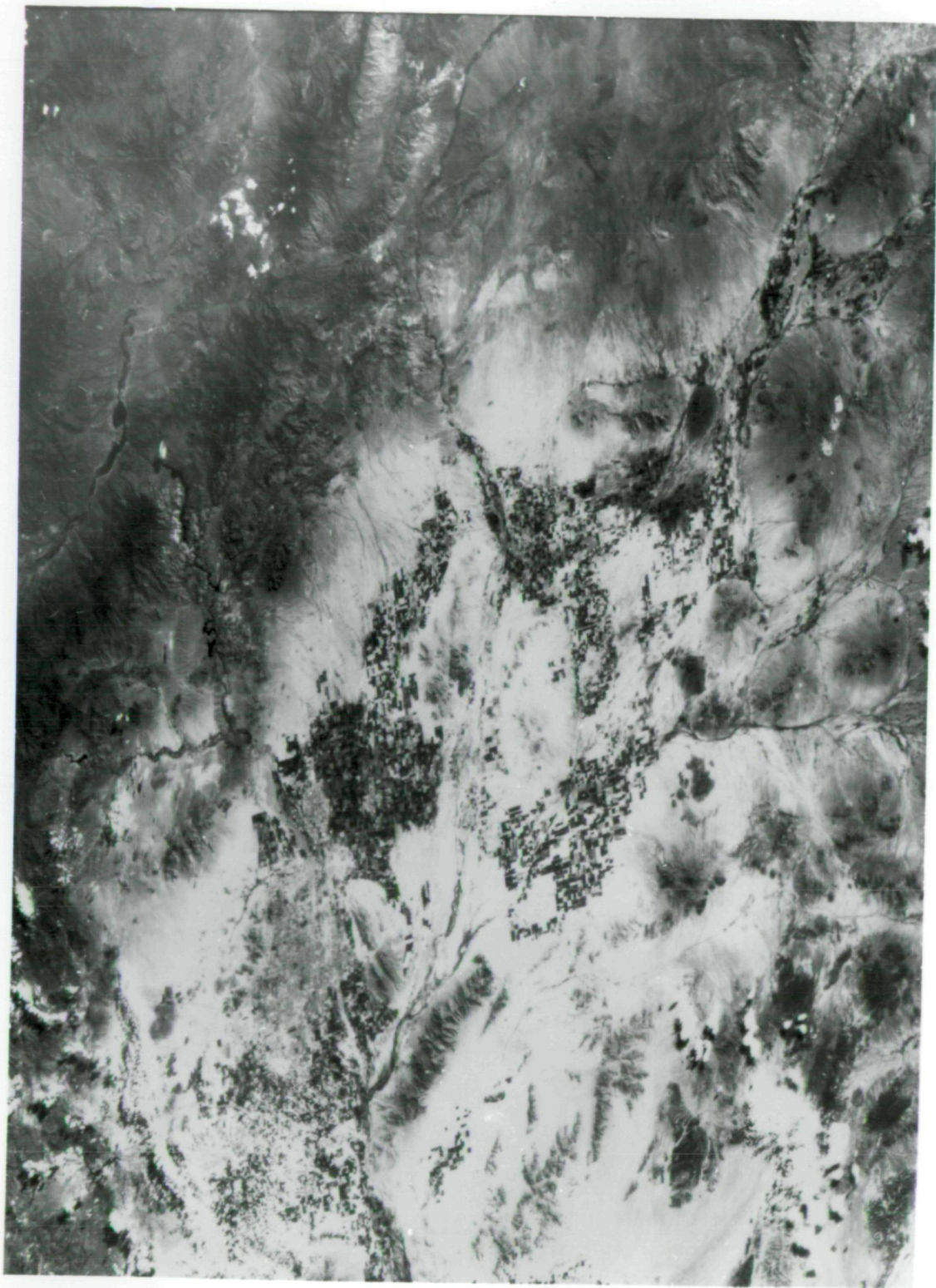


Figure 2-3  
MSS Image Showing Striping